

POLISH
ACADEMY
OF SCIENCES
INSTITUTE
OF FUNDAMENTAL
TECHNOLOGICAL
RESEARCH

ECOLE
NATIONALE
D'INGENIEURS
DE METZ (ENIM)

ENGINEERING TRANSACTIONS

ROZPRAWY INŻYNIERSKIE - TRAITE d'INGENIERIE

QUARTERLY
VOLUME 59
ISSUE 4



WARSZAWA - METZ 2011



Contents of issue 4 vol. LIX

- 251 P. CHURCH, R. PEREIRA, P. GOULD, I. LEWTAS, *Methodology for comparison of hydrocode modelling with experiment for Split Hopkinson Pressure Bar (SHPB) testing of soft materials*
- 263 CH. MARÉCHAL, F. BRESSON, G. HAUGOU, *Development of a numerical model of the 9 mm Parabellum FMJ bullet including jacket failure*
- 273 M. NOWAK, J. OSTROWSKA-MACIEJEWSKA, R.B. PEŁCHERSKI, P. SZEPTYŃSKI, *Yield criterion accounting for the third invariant of stress tensor deviator. Part I. Proposition of the yield criterion based on the concept of influence functions*
- 283 P. SZEPTYŃSKI, *Yield criterion accounting for the influence of the third invariant of stress tensor deviator. Part II: Analysis of convexity condition of the yield surface*
- 299 P. PERZYNA, *Micromechanics of localized fracture phenomena in inelastic solids generated by impact-loaded adiabatic processes*

METHODOLOGY FOR COMPARISON OF HYDROCODE MODELLING WITH EXPERIMENT FOR SPLIT HOPKINSON PRESSURE BAR (SHPB) TESTING OF SOFT MATERIALS

P. C h u r c h ¹⁾, R. P e r e i r a ¹⁾,
P. G o u l d ²⁾, I. L e w t a s ¹⁾

¹⁾ **QinetiQ, WES**

Fort Halstead

Sevenoaks, Kent TN14 7BP, United Kingdom

e-mail: pdchurch@qinetiq.com

²⁾ **QinetiQ, WES**

Bristol, United Kingdom

The objective of this work is to develop a technique for reliable comparison of simulations with SHPB data in order to validate material models for “soft” materials such as polymers. Comparison with an output stress-strain curve is not sufficient since there are many assumptions built into this analysis. Primarily these concern the notion that the specimen is in stress equilibrium and volume is conserved. The problem is that the choice of material model for the specimen in the simulation dictates how and when the specimen attains stress equilibrium. The main methodology is based on comparing the simulations with the raw strain gauge data on the input and output bars, which makes no assumptions about stress equilibrium. However, one has to account for the well documented Pochhammer-Chree oscillations and their effect on the specimen.

1. INTRODUCTION

The Split Hopkinson Pressure Bar (SHPB) has been in use for many years, mainly for metals and also more recently for much softer materials such as polymer, usually in compression. The experimental technique is well documented through papers by KOLSKY [1] and there is an excellent review paper by GRAY *et al.* [2]. The SHPB test is regarded as the key validation test for material models at high strain rate. The main reason for this is that the specimen is considered to be in uniaxial stress after attaining stress equilibrium and high strains can be achieved through purely elastic loading in the bars where there are no shock waves present. Also for metals equilibrium is seen to be obtained

after three stress wave transits in the specimen based on one-wave versus three-wave analysis and the onset of plasticity ensuring no volume change in the specimen. Thus one simply needs to monitor the stress v strain response in the specimen to compare with the experimental output. For softer non-metallic materials such as polymers the deformation mechanisms are driven by elastic behaviour and thus it is not so clear-cut when stress equilibrium is obtained – if indeed the sample is ever in equilibrium during the test. In simulations the choice of material model is the prime determinant of whether the specimen reaches stress equilibrium.

QinetiQ has been involved in the development of physically-based material models for polymer composites, using basic polymer theory. There is a great need to have a reliable means of validating the models, particularly at high strain rates.

This paper aims to highlight the issues with the current techniques in terms of reliably comparing a simulation with an experiment. The paper then outlines a method for reliable comparison, which also sheds great insight into the SHPB test in general. Some recommendations are also made for future studies.

2. EXPERIMENTS

The Standard SHPB set-up consists of a striker bar hitting an input bar and an output bar with a specimen between the two bars, as shown in Fig. 1.

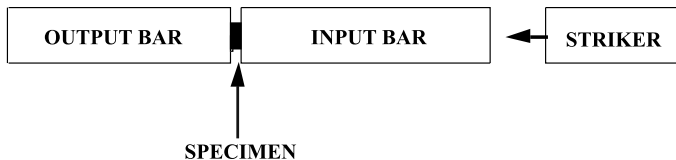


FIG. 1. Standard SHPB set-up.

The general technique is to use strain gauges on the input and output bars which are used to monitor the input, reflected and transmitted pulses. The standard 1D equations attributable to KOLSKY [1] are then applied to derive the stress and strain in the specimen. However, there are a number of fundamental assumptions in these equations, in particular related to the stress equilibrium in the specimen and no volume change in the specimen during the duration of the test. This analysis is also commonly referred to as a one-wave analysis, since it relies on the transmitted pulse to calculate the stress and strain in the sample.

A more sophisticated analysis is to use the so-called 3-wave analysis which uses the relation between the input, reflected and transmitted pulse and it is therefore a more complete analysis. However, even this assumes equilibrium and volume conservation in the specimen. To illustrate how complex these analyses

are a comparison of a 1-wave and a 3-wave analysis for a polymer composite is shown in Fig. 2.

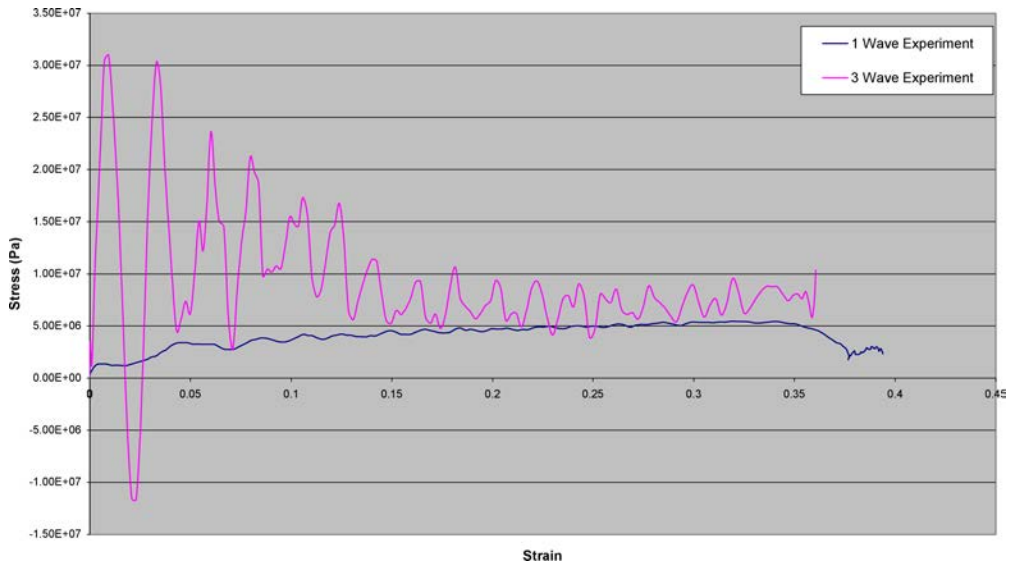


FIG. 2. Comparison of 1-wave and 3-wave analysis for polymer composite.

The assumption is made that the specimen is in equilibrium when the 1-wave and 3-wave analyses are similar. From the figure this is only true at relatively high strains above 0.2 and even then the judgment is subjective. The stress/strain trace is further complicated since there are significant oscillations, resulting from the Pochhammer-Chree (P-C) oscillations present when an elastic wave propagates down the bar. Therefore, it is very difficult to ascertain the true stress/strain behaviour in the sample.

The way to overcome this is to simply use the raw gauge data from the input and output bars for the incident, reflected and transmitted pulses directly. Thus, there are no implicit assumptions about the stress equilibrium or volume conservation in the specimen as the gauges only measured waves in elastic bars. One issue is that for soft materials the transmitted pulse is very small and thus the gauges have to be sufficiently sensitive to resolve these small stresses. This requires the use of semi-conductor gauges to ensure that the signal to noise ratio is sufficiently small. An example of the input, reflected and transmitted pulses for a polymer composite is shown in Fig. 3, where it is noted that the “noise” level on the traces is sufficiently low to enable the stress to be monitored.

The 1-wave and 3-wave analyses are still of value as these are the only means of comparing with an analytic model for the polymer composite material.

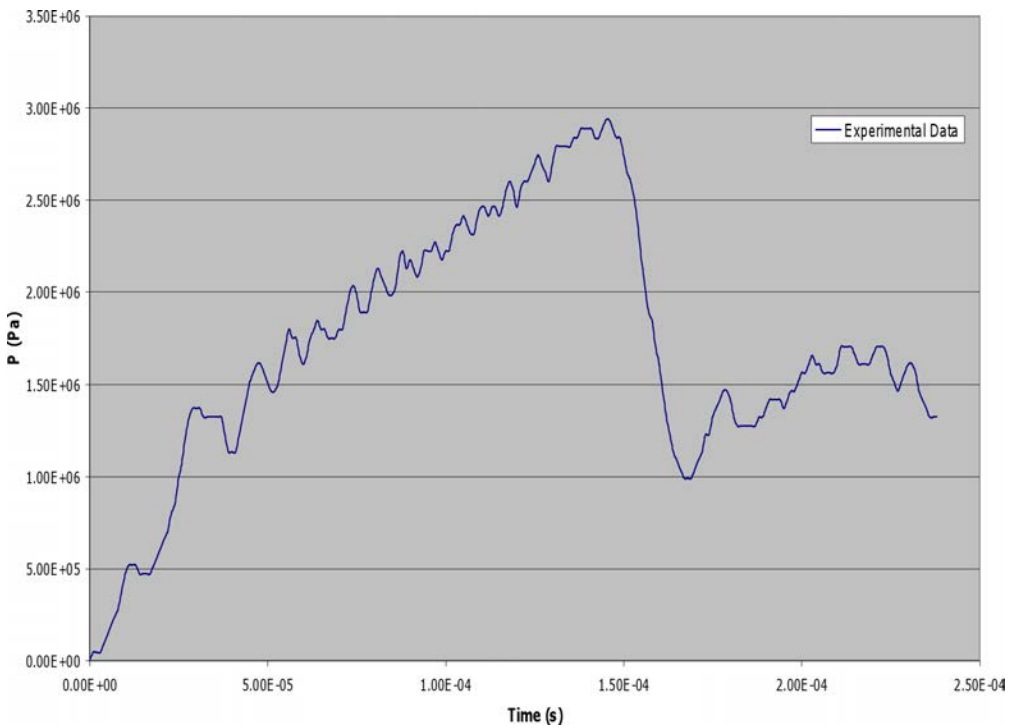
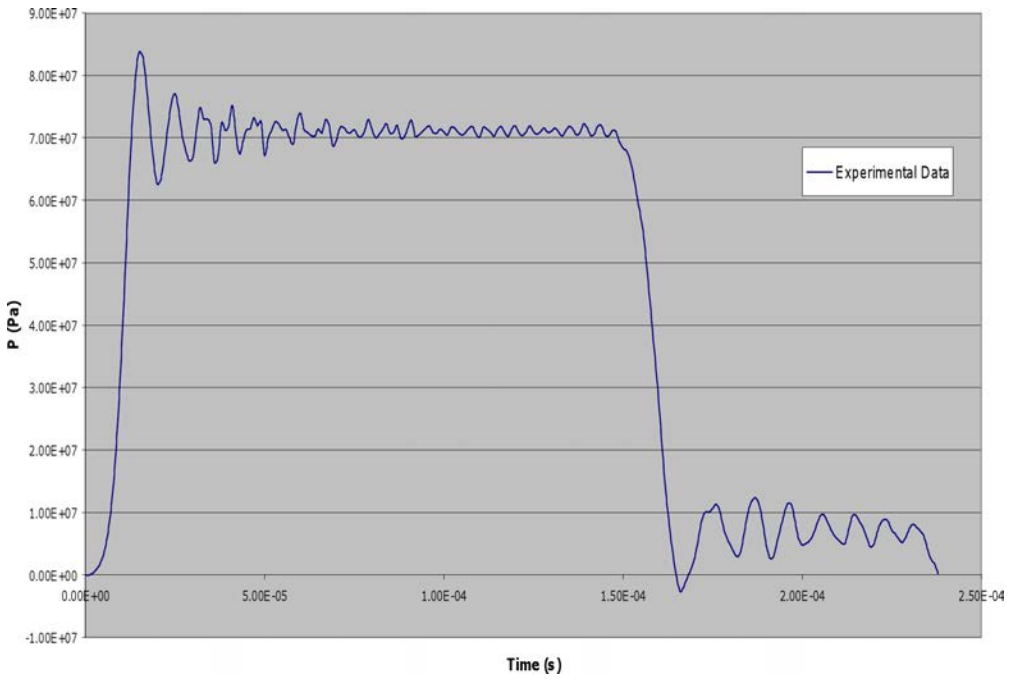


FIG. 3. Experimental input and output SHPB traces for a polymer composite.

3. MATERIAL MODEL

QinetiQ has recently developed the Porter Gould model for polymer composites which uses properties of the particles, the binder and the particle size distribution to determine properties of the composite as described by PORTER and CORNISH [3, 4]. The model assumes that the material follows Hooke's Law but that the secant modulus is a function of the damage in the composite. So the stress/strain curve for uniaxial tension or compression is generated by:

$$\sigma = E_c \varepsilon.$$

The composite, designated QRX221, comprises RDX explosive crystals in an HTPB binder. The particles in the composite range in size from below 1 μm to above 1 mm so we split the particle size distribution into four mass fractions: of order 1 μm , of order 10 μm , of order 100 μm and of order 1 mm. The particle size distribution is known so these mass fractions can be calculated.

The composite modulus, E_c , is calculated by considering each length scale in turn. It is assumed that, at the 1 μm length scale, the larger particles play no part in determining modulus. Thus, by denoting the particle modulus as E_p and binder modulus as E_b we calculate the composite modulus at this level as:

$$\frac{1}{E_{c,1}} = \frac{V_1}{E_p} + \frac{1 - V_1}{E_b},$$

where V_1 is the volume fraction of particles at this length scale.

At the 10 μm length scale we assume that the smaller length scale is sufficiently small that it appears as a continuum and so calculate modulus at this scale as:

$$\frac{1}{E_{c,10}} = \frac{V_2}{E_p} + \frac{1 - V_2}{E_{c,1}}.$$

Similarly at the 100 mm length scale:

$$\frac{1}{E_{c,100}} = \frac{V_3}{E_p} + \frac{1 - V_3}{E_{c,10}}.$$

Finally, the composite modulus for the entire material is:

$$\frac{1}{E_c} = \frac{V_4}{E_p} + \frac{1 - V_4}{E_{c,100}}.$$

Damage to the composite material is assumed to occur by a Griffith-type debonding process whereby work done to the material activates cracking in the binder. This cracking causes a loss of constraint and thereby reduces the modulus of the binder. We define two binder moduli, E_{dam} and E_{undam} , where E_{dam} is the damaged modulus and E_{undam} is the undamaged modulus. Each small local volume of binder is equally likely to crack and so we consider each to be a separate

state. The fraction of failed states – that is the fraction of small local volumes that have cracked and thereby have E_{dam} rather than E_{undam} – is denoted f . The binder modulus is therefore:

$$E_b = E_{\text{undam}} - f \cdot (E_{\text{undam}} - E_{\text{dam}}).$$

We now need to know the work done that the binder sees. This is a function of the compliances. The “binder” at the highest length scale sees a fraction of the work done on the composite:

$$W_{c,100} = \frac{E_p}{E_p + E_{c,100}} W_c$$

and so at lower length scales:

$$W_{c,10} = \frac{E_p}{E_p + E_{c,10}} W_{c,100},$$

$$W_{c,1} = \frac{E_p}{E_p + E_{c,1}} W_{c,10},$$

$$W_b = \frac{E_p}{E_p + E_b} W_{c,1}.$$

The probability of cracking is an activated process. If W_0 is an energy density characteristic of failure in the binder then the fraction of failed states is:

$$f = \frac{2 \cdot \exp(-W_0/W_b)}{1 + \exp(-W_0/W_b)}.$$

The model presumes that all temperature and strain-rate dependency is in the binder response as this dominates the mechanical response of the polymer composite. The model therefore uses a single particle shear modulus of 5.0×10^9 Pa, and a particle Poisson’s ratio of 0.3 under all conditions. The binder Poisson’s ratio is taken to be 0.4998. The particle size distribution is assumed to be as shown in Table 1.

Table 1. Particle size distribution for QRX221 composite.

lengthscale	V	$1 - V$
1	0	1
2	0.378	0.622
3	0.469	0.531
4	0	1

Implementation of the model into numerical schemes needs the full 3D behaviour and the shear modulus, G , is more appropriate than Young's modulus. The above equations are still used, however, via the relation:

$$G = \frac{E}{2(1 + \nu)},$$

where ν is Poisson's ratio. The constitutive model seeks predictions of G (undamaged), G (damaged) and W_0 for the binder as a function of strain-rate and temperature. All units are SI. The strain rate and temperature are first transformed via:

$$X = C_1 - C_2 \cdot [T - C_3 \cdot \ln(\dot{\varepsilon})],$$

where T and $\dot{\varepsilon}$ are temperature and strain rate and C_1, C_2, C_3 are constants as an attempt to mimic time-temperature superposition. The constants are chosen so that X increases with increasing rate and decreasing temperature and should always be positive for any condition likely to be found in reality. In practice, the data consists of temperature series at two different rates and the constants are chosen so that the two temperature series at the two rates form a continuous smooth curve.

The following equations are then used:

$$G_{\text{undamaged}} = A \cdot \exp[C_4 + C_5 \cdot \exp(X)] + S \cdot 9 \cdot \frac{1 - 2 \cdot \nu}{1 + \nu} \cdot P,$$

$$G_{\text{damaged}} = A \cdot \exp[C_6 + C_7 \cdot \exp(X)] + S \cdot 9 \cdot \frac{1 - 2 \cdot \nu}{1 + \nu} \cdot P,$$

$$E_0 = B \cdot \exp[C_8 + C_9 \cdot X].$$

The fitting constants for the QRX221 compositions are:

Table 2. Constants for Porter-Gould model for QRX221 composition.

constant	Value	unit
C_1	5	
C_2	0.01	K ⁻¹
C_3	10	K
C_4	13.5	
C_5	0.14	
C_6	10.3	
C_7	0.21	
C_8	11	
C_9	0.45	

The constants A and B are not fitting constants but are used to convert G and E_0 to the correct units. For SI units $A = 1$ Pa and $B = 1$ Jm⁻³. S is a switch constant to turn pressure-dependency off or on and so takes values of either 0 or 1. P is the pressure and ν is Poisson's ratio = 0.4998. An example of the model comparison to SHPB data for the QRX221 is shown in Fig. 4.

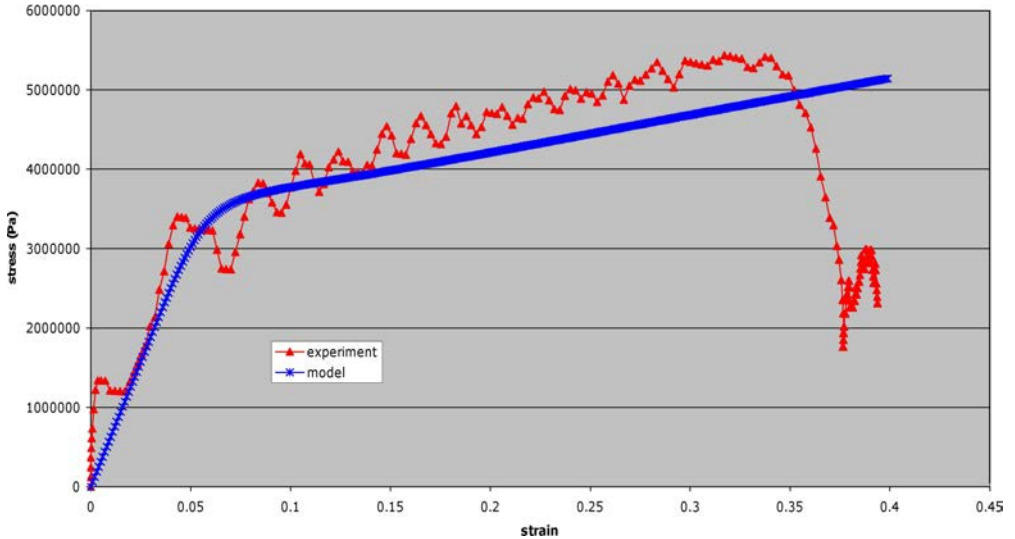


FIG. 4. Comparison of stress v strain from Porter-Gould model to SHPB test at room temperature for QRX221.

4. SIMULATIONS

The whole point of the SHPB test is that it is a high strain rate validation test for constitutive models in hydrocodes. As described above it is problematic to compare the hydrocode output directly with the stress/strain output from the experiment. The proposed route forward is to use the hydrocode to compare directly with the input, reflected and output gauge pulses. However, this implies that the hydrocode is capable of capturing all the physics in the SHPB in terms of the input, reflected and output pulses. This is actually quite complicated since the nature of the P-C oscillations must also be accounted for, since this produces a load/unload cycle in the specimen.

In terms of the input pulse, a typical comparison of simulation and experiment using the DYNA3D Lagrangian hydrocode is shown in Fig. 5. As can be seen the comparison is very good even in terms of the general P-C oscillations. This comparison is largely insensitive to artificial viscosity in the hydrocode.

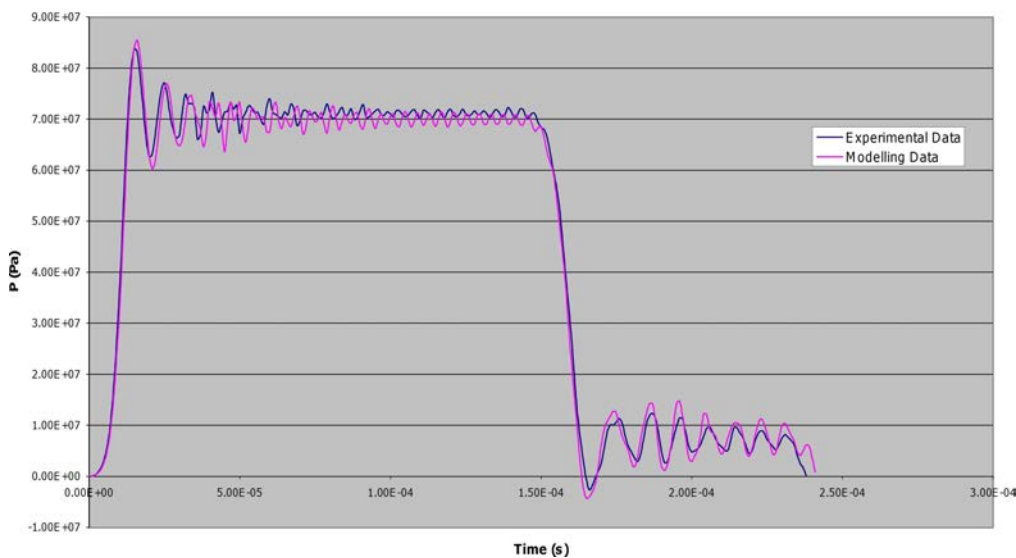


FIG. 5. Comparison of simulation and experiment for input pulses.

It is worth noting that the P-C oscillations can be removed by putting a curved impact face on the striker bar as shown in Fig. 6. This is useful

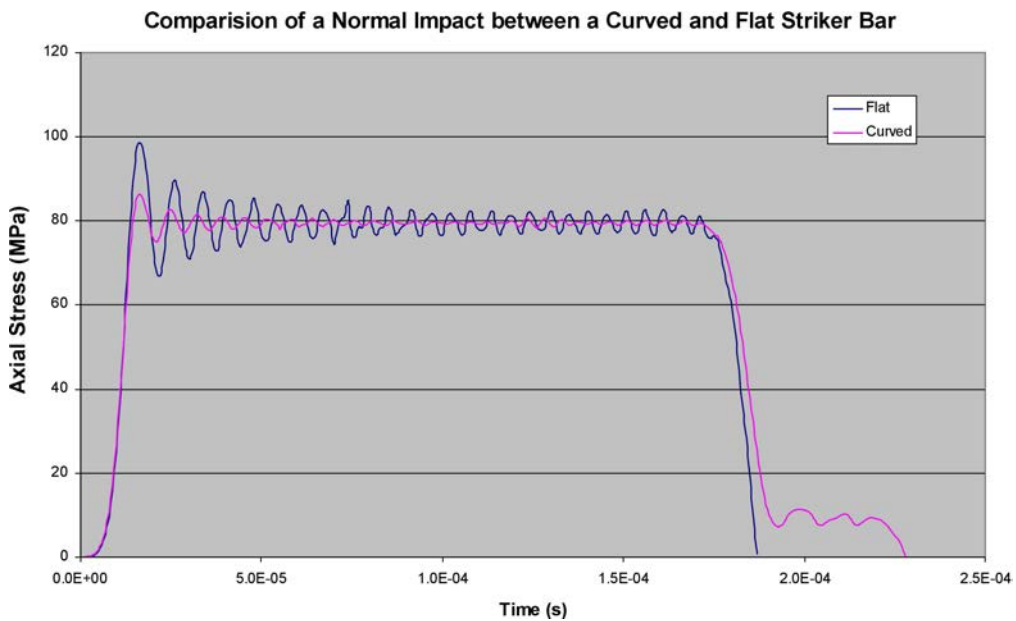


FIG. 6. Comparison of input pulses for flat and curved impact face on the striker bar for SHPB.

since it means that SHPB tests can be performed where the P-C oscillations are minimised and so the output can be compared directly with analytic models. Conversely, the P-C oscillations provide a load/unload cycle on the sample which is a very stringent test of the material model when implemented into the hydrocode.

The comparison between the hydrocode model and experiment for the output pulse is shown in Fig. 7, where there are no implicit assumptions concerning specimen equilibrium or volume conservation.

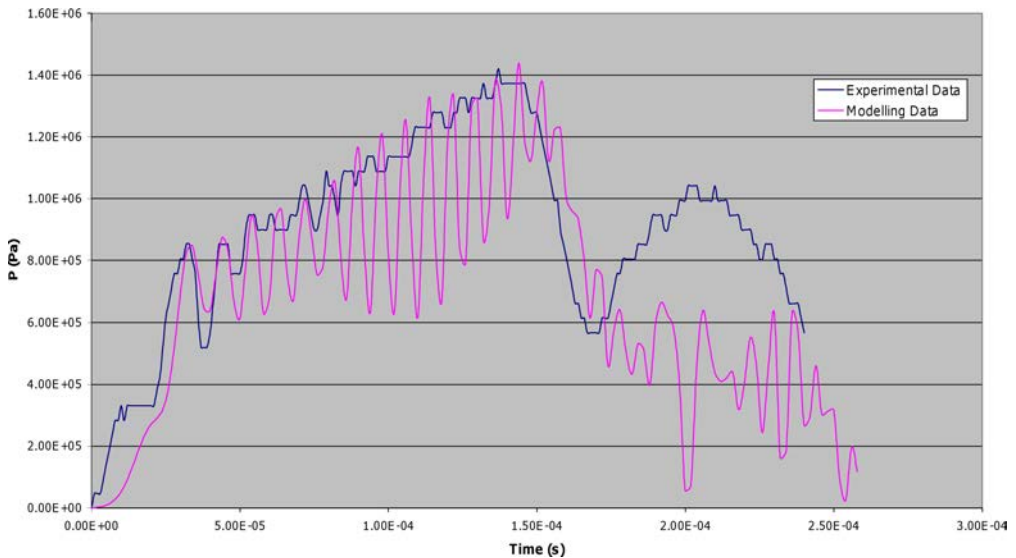


FIG. 7. Comparison of model against experiment for output pulse for QRX221.

The level of agreement for the general stress level and pulse length is good, although it is noted that the model exhibits significantly more oscillation than the experiment. The main reason for this is that the load/unload capability of the model is still limited and requires a true physically-based model for the polymer, which is being developed. However, without a robust method of comparing hydrocode with experiment it would be unclear where the deficiencies in the model lay. In addition the model does not pick up the very high initial modulus in the output pulse, which also requires further theoretical analysis. One can also still perform the 1-wave and 3-wave analyses on the pulses for comparison with experiment as shown in Fig. 8 for the 1-wave analysis.

To further demonstrate the power of the approach a comparison with an SHPB test performed at 223 K is shown in Fig. 9.

The level of agreement is very impressive in terms of the stress level. The length of the pulse is different since the specimen exhibited radial cracks during

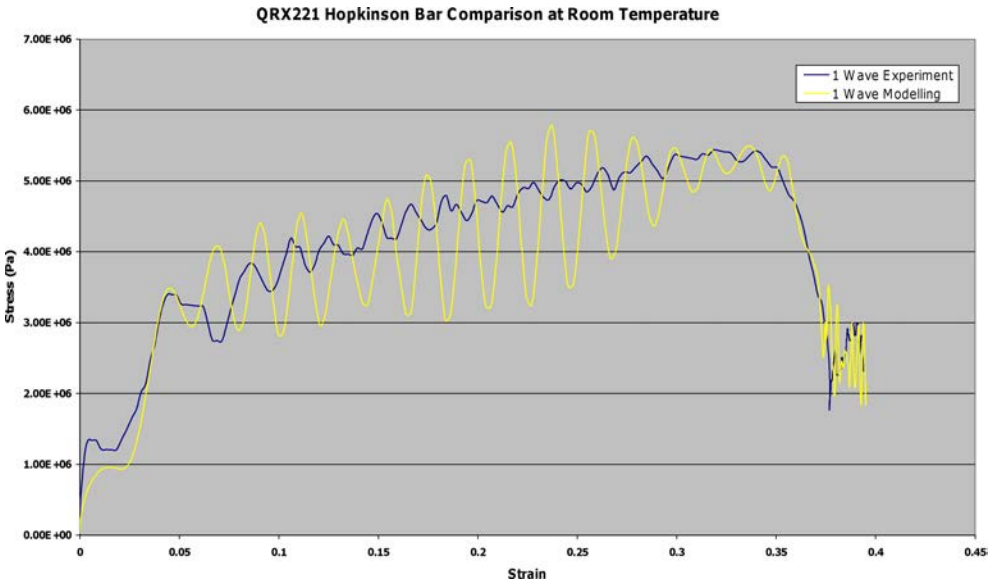


FIG. 8. Comparison of modelling and experiment for 1-wave analysis for QRX221.

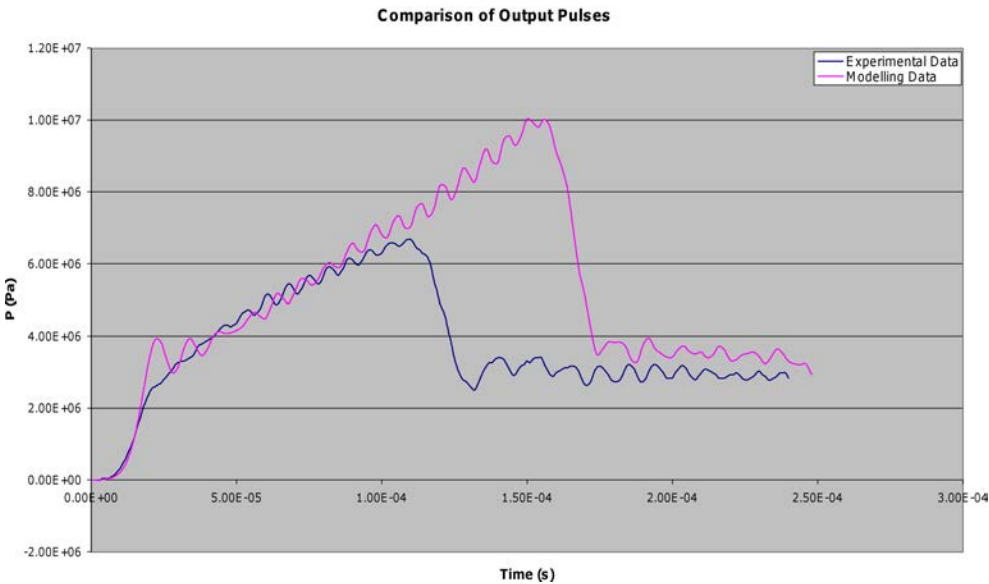


FIG. 9. Comparison of model and experiment for QRX221 at 223 K.

the test. Indeed the time of the pulse can be directly correlated to the timescale of the macroscopic fracture in the specimen. This general level of agreement gives enhanced confidence that the models are suitable for use in real applications such as hazard assessment of munitions, gun launch, etc.

5. CONCLUSIONS

1. A methodology for effective comparison of simulations with SHPB experiments has been defined based on comparison of the simulations with the raw gauge data. The methodology is robust for general “soft” materials over a range of temperatures.
2. This has been demonstrated for the QRX221 polymer composite and has highlighted further required developments to the model in the form of a physically based polymer model and better load/unload functionality.
3. The P-C oscillations are a good test of the material model as they provide a load/unload cycle in the specimen during the test.
4. The approach gives added confidence that the models can be effectively applied to real scenarios.

ACKNOWLEDGMENT

This work has been supported by UK Ministry of Defence over a range of research contracts.

REFERENCES

1. H. KOLSKY, *An Investigation of the Mechanical Properties of Materials at Very High Rates of Loading*, Proc. Phys. Soc. Lond., **B62**, 676–700, 1949.
2. G. GRAY, *High Strain Rate Testing of Materials: Split Hopkinson Pressure Bar*, LANL report LA-UR-97-4419, 1997, Los Alamos, USA.
3. D. PORTER, *Group Interaction of Polymer Properties*, Marcel Dekker, New York, 1995.
4. R. CORNISH, D. PORTER, P. CHURCH, P. GOULD, T. ANDREWS, B. PROUD, D. DRODGE, C. SIVIOUR, *Comparison of Porter-Gould Constitutive model with Compression Test Data for HTPB/Sugar*, APS conference, Hawaii, 2007.

Received January 11, 2011; revised version July 21, 2011.

DEVELOPMENT OF A NUMERICAL MODEL OF THE 9 MM PARABELLUM FMJ BULLET INCLUDING JACKET FAILURE

Ch. Maréchal¹⁾, F. Bresson²⁾, G. Haugou¹⁾

¹⁾ **Université Lille Nord de France**

F-59000 Lille, France

UVHC, LAMIH

F-59313 Valenciennes, France

CNRS, FRE 3304

F-59313 Valenciennes, France

²⁾ **Institut National de Police Scientifique**

Laboratoire de Police Scientifique de Lille

7 bd Vauban, 59000 Lille, France

Even though ballistic experiments are widely accepted as the only reliable way to probe terminal effects, we demonstrate that computer simulation can be a useful alternative. Particularly, the high energy projectiles are seldom studied in the field of forensic sciences. That situation being favorable to computer simulation, a 3D finite element model of the worldwide-used 9 mm Parabellum bullet has been developed with Abaqus explicit software. A Johnson-Cook constitutive model, fed with the split Hopkinson pressure bar experimental parameters, accurately describes the materials' behavior (lead and brass). Experiments were performed with a handgun and a hard steel plate target in order to discuss the reliability of the model. Accurate predictions about bullet deformation and failure were obtained without any post-calculation adjustment of parameters.

Key words: ballistics, FEM, Johnson-Cook.

1. INTRODUCTION

Gunshot investigation is a key activity of any forensic science institute. The shooter's position is classically estimated from a post impact examination of a scene (multiple impacts). The line passing by the center of each impact figure is materialized with a laser beam or a set of metallic rods. It can also be calculated from an accurate 3D positioning of each impact. A correction of the bullet's path deflection (under the influence of its weight) can be considered in some particular cases (long distance shooting). As a consequence, if a gunshot involves only a single impact no information about the position of the shooter can be given. The second limitation is the lack of knowledge about impact

phenomena (deflection, velocity loss, bullet's integrity and stability) which are known qualitatively but not quantitatively. A specific procedure involving target examination (gunshot residue scattering, smoke or multi-projectile dispersion, the Griess test) is also applied to estimate the shooting distance (not the angle), but besides the specific case of shotgun (multi-projectile), the efficiency range of these methods is typically limited to a few meters.

In that context, it has already been demonstrated that comparing the bullet deformation with experiments can bring up some information about the shooting distance, in the case of a hard target (metal, concrete [1]) or a soft target (human body [2, 3]). The method used to determine the ballistic parameters is the experimental way, the main reason being the lack of adequate computer simulation of material deformation in the ballistic domain. The source of this inadequateness can be found in the complexity of the problem itself, and also in the low number of applications. The deformation state under ballistic impact velocities (from 100 to 1000 ms^{-1}) can only be described by rather complex and multi-parameter laws. Identifying each parameter is a problem, the complexity of which increases with the impact velocity. The ballistic domain stands between the Lagrangian (solid) and Eulerian (fluid) formulation. Unifying these formulations is still an issue. On the application side, military requirements (effects of a given structure of projectile hitting a given structure of target) are quite easy to investigate with experimental tools. In forensic applications (recovery of pre-impact information from post impact examination), computer simulation could be an alternative to experiments when a gunshot cannot be accurately reproduced (excessive distance, accuracy or cost), but this demand was only formulated lately.

In the present study, the worldwide- used 9 mm Parabellum FMJ (Full Metal Jacket) bullet was selected as a representative sample. A 3D finite element model has been developed with Abaqus explicit software. The constitutive model for lead and brass is based on the Johnson-Cook relation without failure formulation. The split Hopkinson pressure bar experimental data were used to identify the missing parameters. The predictions were compared with ballistic experiments performed with a semi-automatic Glock 26 compact pistol and homemade ammunition with muzzle velocity ranging from 30 to 200 ms^{-1} .

2. BALLISTIC EXPERIMENTS

The thrower is a Glock 26 semi-automatic pistol. The target is a 30 mm thick iron plate. The shooting distance is set to 2 m. Different velocities were obtained by varying the amount of propellant (Vectan Ba 9) in home-made 9 mm Parabellum cartridges. The bullets are 9 mm Parabellum lead core FMJ weighting 115 gr (grain), i.e., 7.45 g (actually ranging from 7.39 to 7.49 g in our

experiments). Impact velocities are measured half way between the handgun and the target with a chronograph (Pro Chrono, Competition Electronics Inc, USA). Very low velocities (down to 60 ms^{-1}) were repeatedly obtained.

The way we chose to describe both the length reduction and diameter expansion was to define a deformation criteria C as follow:

$$(2.1) \quad C = \sqrt{\frac{1}{2} \cdot \left[\left(\frac{\Delta l}{l_0} \right)^2 + \left(\frac{\Delta d}{d_0} \right)^2 \right]},$$

with $\Delta l = l - l_0$ and $\Delta d = d - d_0$. l_0 and d_0 are respectively the length and the diameter of the bullet before impact. The nature of C (single value) is more suitable for comparison. This criteria can theoretically be higher than 1.

For each experiment, the length (l) and the diameter (d) of the bullet were measured using a micrometer and finally C was calculated. The behavior of C versus impact velocity is given in Fig. 1. The blue dots are the experimental data; the red lines are the least square approximation in the two distinctive areas. In the second area, the last two dots have not been considered for the least square approximation as they demonstrate a saturation behavior slightly below fragmentation.

Figure 1 demonstrates that C follows two rather linear behaviors, with a velocity threshold triggering jacket fracture in-between. The so-called frac-

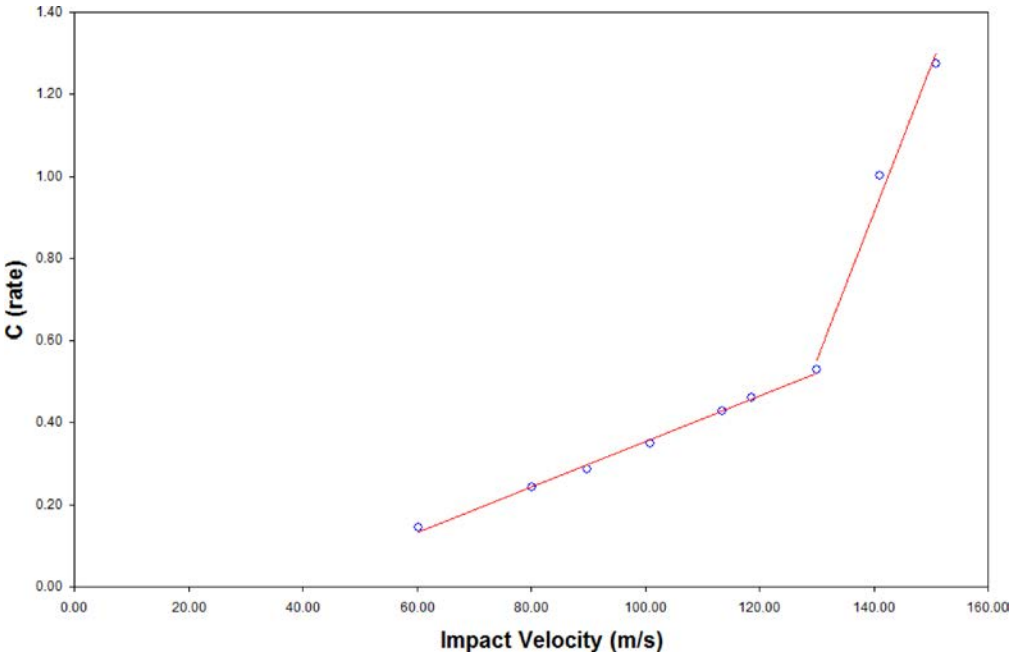










FIG. 1. Behavior of C versus impact velocity.

ture threshold is 130 ms^{-1} in the experimented case. The slope of the curve is $5.6 \cdot 10^{-3} \text{ s m}^{-1}$ below the fracture threshold. Beyond the fracture threshold, the slope of the curve is 6 times higher ($3.4 \cdot 10^{-2} \text{ s m}^{-1}$) before reaching a saturation behavior and then approaching the fragmentation threshold. A core fragmentation has been observed with an experimental impact velocity of 176 ms^{-1} . Core and jacket fragmentation has been observed with an impact velocity slightly higher (182 ms^{-1}). This area cannot be described with C . With an impact velocity of 203 ms^{-1} , a part of the core remained soldered to the target. Beyond the fragmentation threshold, the size of the fragments decreases as the velocity increases. We believe, however, that a very little quantitative prediction can be gathered from a statistical fragment sizing.

Table 1 exhibits the shape of the deformation and eventually a fracture and fragmentation of few bullets for impact velocities ranging from 60 to 200 ms^{-1} .

Table 1. Deformation shape, fracture and fragmentation of the projectile for various impact velocities.

Impact Velocity [ms^{-1}]	60	80	101	119	141	164	182	203
C (rate)	0.14	0.24	0.35	0.46	1	1.46		
								

The experimental fracture and fragmentation speed thresholds will increase dramatically when the target cannot withstand ballistic load without deformation, as in most of the forensic cases. In that situation, any new target, new material or new target shape actually need a new study, pointing out to the usefulness of a FEM simulation tool.

3. FEM MODEL

3.1. Materials models

This part describes the determination of the mechanical properties of the quasi-pure lead extracted from the bullets by heating process ($\rho = 11300 \text{ kg m}^{-3}$ and $\nu = 0.42$). The purpose is to determine the true plastic laws from quasi-static to dynamic loadings under compression loading. Finally, parameters of the constitutive simplified Johnson-Cook model are calculated without considering heat transfer, as shown in Eq. (3.1) [4].

$$(3.1) \quad \sigma = (\sigma_0 + K \cdot \varepsilon^n) \times \left(1 + D \cdot \ln \left(\frac{\dot{\varepsilon}}{\dot{\varepsilon}_0} \right) \right),$$

σ_0 is the yield stress, K is the hardening parameter, n is the exponent for the static law and D is the parameter which determine the viscosity effects. $\dot{\epsilon}_0$ describes the activation of the strain rate effects.

The experimental setup includes the cylindrical samples ($\varnothing = 8$ mm, $l_0 = 7$ mm) submitted to the compression loadings from:

- A high-speed hydraulic machine (VHS) with a strain rates ranging from 0.15 to 20 s⁻¹ (Fig. 2a),
- A set of nylon split Hopkinson pressure bars with a strain rate ranging from 800 to 2000 s⁻¹ (Fig. 2b).



FIG. 2. a) VHS setup, b) Hopkinson bars setup.

Figure 3b illustrates the behaviour of the considered materials used for the determination of the Johnson-Cook parameters. The materials responses are determined from:

- strain gauges for Hopkinson tests,
- piezoelectric load cells coupled with electro-optical extensometers for VHS tests.

The raw signals have been recorded using a numerical recorder at adaptive sampling rates. For the Hopkinson calculations, the visco-elasticity and punching corrections have been considered [5, 6].

The Johnson-Cook parameters have been determined after keeping plastic relations at 0.15, 20800 and 1500 s⁻¹ (dotted line in Fig. 3b). A classical calculation based on least squares interpolation has been used. The results are sum up in Table 2.

Lead has revealed a visco-elasto-plastic behaviour under compression loadings, but the authors have considered only visco-plasticity as a first step.

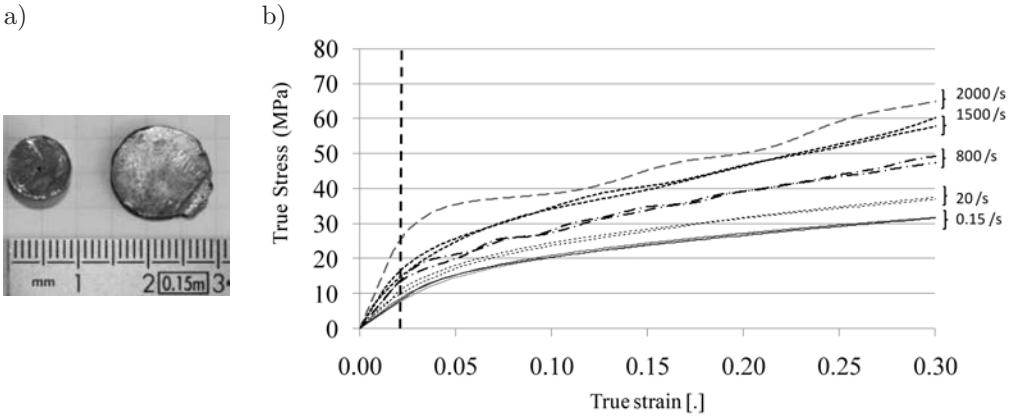


FIG. 3. a) Initial and final shapes of specimens; b) behaviour laws under compression loadings from 0.15 to 2000 s^{-1} .

Table 2. Johnson-Cook parameters for lead samples ($R^2 = 0.9891$).

E_{STATN}	E_{DYN}	σ_0	K	n	D
0.41 GPa	1.3 GPa	5.15 MPa	35.35 MPa	0.5	0.0628

3.2. Numerical model

The numerical simulation was developed by Abaqus finite element model software with the explicit numerical algorithm formulation. The projectile and the target were designed using a 3D axi-symmetric solid model. The impact has been considered as an axi-symmetric phenomenon by neglecting spinning effects of the projectile (spinning energy represents only few percent of the total kinetic energy). Furthermore, bullets didn't undergo any twisted deformation in the experiments. The main interest of the axi-symmetric simulation was to save computation time without decreasing the accuracy.

The bullet was meshed in 4 nodes elements with reduced integration. The projectile grid is composed of 6000 elements. The mechanical behaviour of the projectile is the main issue of the simulation as the steel target has been considered as a pure elastic solid ($E = 210000 \text{ MPa}$, $\rho = 7800 \text{ kg m}^{-3}$, $\nu = 0.33$). The shape of the bullet was extracted from a picture of a cut-off bullet by a Matlab routine. Figure 4 presents the finite element model of the bullet (b) and the picture of the cut-off bullet (a).

The bullet design includes two materials: a lead core and a brass jacket (a copper alloy also known as tumbac, 90% Cu and 10% Zn). A Johnson-Cook constitutive model has been used for each component. The parameters of lead are given in Table 2. The parameters of tumbac are extracted from the literature [7, 8]. The model didn't include fracture, but the fracture threshold criterion

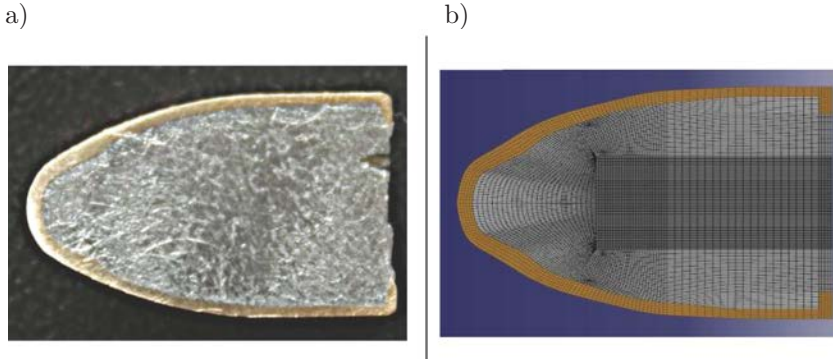


FIG. 4. Cut-off picture (a) and FEM (b) of the bullet.

proposed by COCKCROFT and LATHAM [9] has been compared to the maximum load observed at the experimental fracture threshold (130 ms^{-1}). We also made sure that the plastic work, W_p , level overlaps the critical value proposed by BØRVIK *et al.* [10] for the brass jacket ($W_p = 914 \text{ MPa}$).

Contact was considered without friction between the target and the bullet. Sliding was allowed between the lead core and the brass jacket, according to the experimental observations presented in Fig. 5.

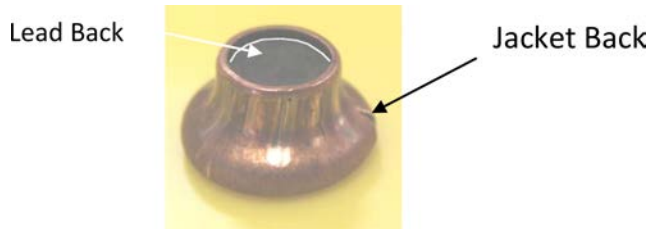


FIG. 5. Sliding between lead and jacket.

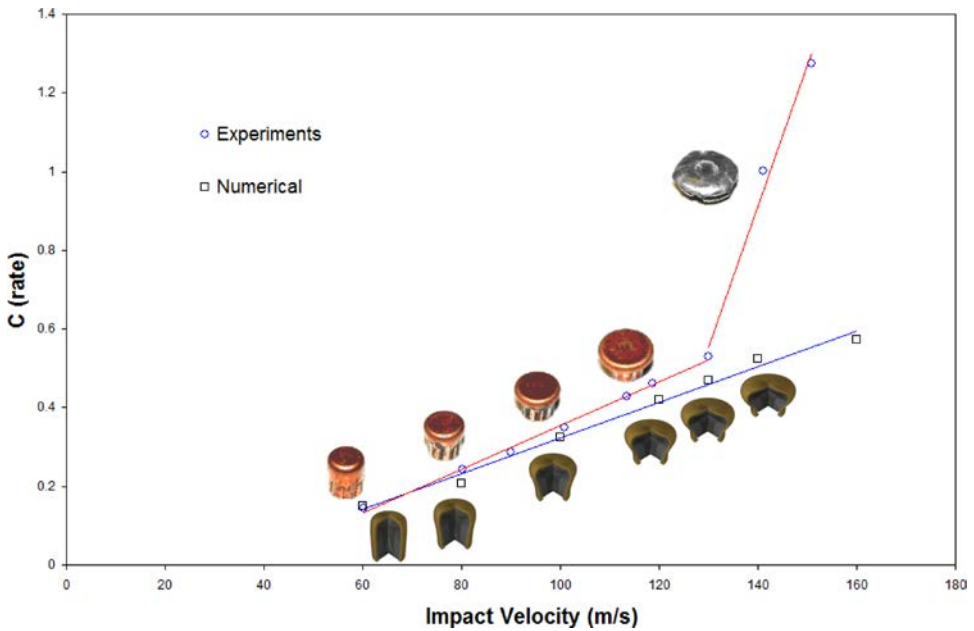
3.3. Correlation with experimental investigation

The model was run with velocities ranging from 60 to 160 ms^{-1} . The displacement and plastic work data were monitored from impact time (t) to $t + 3 \text{ m/s}$ (until the bullet reaches its steady post-impact state). Bullet diameter and length were extracted to calculate C for each simulation. Table 3 and the Fig. 6 show the results.

The numerical model and experimental results show a very good similarity until an impact velocity ranging from 130 to 140 ms^{-1} occurs. The experimental data exhibited fracture triggering at the same velocity. The fracture, allowing stress relaxation in the jacket, can not be considered in the model (not allowed in the axi-symmetric configuration). Such a structural weakening increases crushing and the criterion C . The lack of stress relaxation in the model explains the

Table 3. Experiment and numerical results.

Experiments				Numerical				
Velocity [ms ⁻¹]	Diameter [mm]	Length [mm]	C	Velocity [ms ⁻¹]	Diameter [mm]	Length [mm]	C	WpMax [MPa]
60.3	9.46	11.23	0.14	60	9.08	11.67	0.15	478
80.2	10.8	10.10	0.24	80	10	10.18	0.21	484
89.9	11.35	9.73	0.29	100	11.3	8.7	0.32	447
100.9	12.1	9.12	0.35	120	12.36	7.62	0.42	614
113.4	13.05	8.45	0.43	130	12.9	7.08	0.47	687
118.6	13.4	8.08	0.46	140	13.54	6.5	0.52	2380
130.1	14.2	7.47	0.53	160	14.13	6.03	0.57	5586
141.1	20	4.3	1					
150.9	23.50	3.22	1.27					

**FIG. 6.** Experiment and numerical behavior of C versus impact velocity.

difference between the experimental and the numerical results beyond 130 ms^{-1} . As explained above, the plastic work level has been used as an evidence to point out the emergence of fractures in the model. Figure 7 shows the evolution of the maximum plastic work of the jacket versus an impact velocity. The Børvik threshold criterion was overlapped with an impact velocity of 130 ms^{-1} . The non-linear increase of the plastic work is not realistic because of the enactment

of element in the model when the fracture phenomena appear. Modifications of the loading mode were observed in the model between 130 and 140 ms^{-1} . The jacket, which was in compression until 130 ms^{-1} , changed into a buckling mode. This change explains the fracture's triggering and the very important plastic work increase (according to a plastic strain increase). The agreement with experimental data is also very satisfactory.

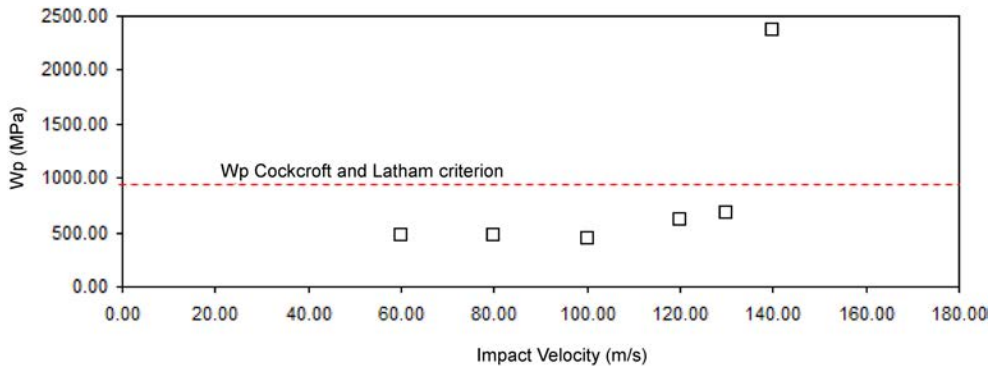


FIG. 7. Numerical results for maximum plastic work versus impact velocity.

Extra simulations (not reported here) demonstrated that a particular care must be taken about the jacket thickness variations. A maximum thickness is clearly visible near but off the tip (c.f., Fig. 4a). The approximation of a uniform thickness or even a slightly wrong shape induces a dramatic discordance with the experimental results.

4. CONCLUSIONS

This paper demonstrates the good correspondence between the FEM model using explicit formulation and the experiment in the ballistic field. The sine qua non condition for such a good behavior of the model was to provide accurate parameters for the Johnson-Cook constitutive model of each component. The parameters were extracted from the literature for tambac, from the Hopkinson bar experiments for the lead, and no extra adjustment were made. In that drastic situation, a very good concordance has been observed as far as the dynamic load did not exceed the fracture threshold.

For the explored velocity range, it has not been necessary to consider spin and heat transfer, but the results pointed out that a very good care about the jacket thickness is necessary to accurately reproduce the shape of the experimental deformations. Ongoing researches will include fracture and heat transfer in order to minimize the limitation of the Lagrangian formulation in the ballistic domain.

ACKNOWLEDGMENT

The authors would like to thank D. Lesueur for his helpful hand. The present research work has been supported by International Campus on Safety and Intermodality in Transportation- the Nord-Pas-de-Calais Region, the European Community, the Regional Delegation for Research and Technology, the Ministry of Higher Education and Research, and the National Center for Scientific Research. The authors gratefully acknowledge the support of these institutions.

REFERENCES

1. F. BRESSON, O. FRANCK, *Estimating the shooting distance of a 9 mm Parabellum bullet via ballistic experiment*, *Forensic Science International*, **192**, 1–3, 17–20, 2009.
2. K. G. SELIER, B. P. KNEUBUEHL, *Wound ballistic and the scientific background*, Elsevier 1994.
3. F. BRESSON, O. FRANCK, *Comparing ballistic wounds with experiments on body simulator*, *Forensic Science International*, **198**, 1–3, 23–27, 2010.
4. G. R. JOHNSON, W. H. COOK, *A constitutive model and data for metals subjected to large strains, high strain rates and high temperatures*, Proceedings of seventh international symposium on ballistics, The Hague, the Netherlands, 1983.
5. G. GARY, V. DEGREEF, David, *Labview Version, Users manual version*, LMS Polytechnique, Palaiseau, 2008.
6. K. SAFA, G. GARY, *Displacement correction for punching at a dynamically loaded bar end*, *International Journal of Impact Engineering*, **37**, 4, 371–384, 2010.
7. S. CHOCRON, C. E. ANDERSEN Jr, D. J. GROSCH, C. H. POPELAR, *Impact of the 7.62 mm APM2 projectile against the edge of a metallic target*, *International Journal of Impact Engineering*, **25**, 23–37, 2001.
8. C. E. ANDERSEN Jr, M. S. BURKINS, J. D. WALKER, W. A. GOOCH, *Time-resolved penetration of B₄C tiles by the APM2 bullet*, *Computer Modeling in Engineering & Sciences*, **8**, 2, 91–104, 2005.
9. M. G. COCKROFT, D. J. LATHAM, *Ductility and the workability of metals*, *Journal of the Institute of Metals*, **96**, 33–39, 1968.
10. T. BØRVIK, S. DEY, A. H. CLAUSEN, *Perforation resistance of five different high-strength steel plates subjected to small-arms projectiles*, *International Journal of Impact Engineering*, **36**, 7, 948–964, 2009.

Received March 29, 2011; revised version July 21, 2011.

YIELD CRITERION ACCOUNTING FOR THE THIRD INVARIANT OF STRESS TENSOR DEVIATOR.

PART I. PROPOSITION OF THE YIELD CRITERION BASED ON THE CONCEPT OF INFLUENCE FUNCTIONS

M. Nowak¹⁾, J. Ostrowska-Maciejewska¹⁾,
R.B. Pęcherski¹⁾, P. Szeptyński^{1,2)}

¹⁾ **Institute of Fundamental Technological Research
Polish Academy of Sciences**

Pawińskiego 5B, 02-106 Warszawa, Poland

²⁾ **AGH University of Science and Technology
Faculty of Mechanical Engineering and Robotics
Department of Strength, Fatigue of Materials and Structures**

Al. A. Mickiewicza 30, 30-059 Krakow, Poland

A proposition of an energy-based hypothesis of material effort for isotropic materials exhibiting strength-differential (SD) effect, pressure-sensitivity and Lode angle dependence is discussed. It is a special case of a general hypothesis proposed by the authors in [11] for anisotropic bodies, based on BURZYŃSKI'S concept of influence functions [2] and RYCHLEWSKI'S concept of elastic energy decomposition [16]. General condition of the convexity of the yield surface is introduced, and its derivation is given in the second part of the paper. Limit condition is specified for Inconel 718 alloy, referring to the experimental results published by IYER and LISSENDEN [7].

1. INTRODUCTION

1.1. Motivation

In recent years, the number of new materials (e.g. composites, modern alloys) exhibiting certain uncommon properties – such as low elastic symmetry, pressure sensitivity, Lode angle dependence, strength differential effect – still increases and they become more and more commonly used. Furthermore, the precision of the measurement tools and accuracy of mathematical or numerical models used for the description of industrial processes is still improved, so some of the mentioned phenomena, which for decades have been considered negligible, now seem to be necessary to be involved in the mechanical analysis of the considered processes. Classical yield criteria, which are still commonly used

both in elastic and plastic analysis (as limit conditions or plastic potentials in case of associated flow rule), cannot deal with those specific features of modern materials in a satisfactory way.

Many propositions of the yield criteria for anisotropic bodies were already stated (e.g. MISES [10], BURZYŃSKI [2], HILL [4], HOFFMAN [5], TSAI-WU [20], RYCHLEWSKI [15], THEOCARIS [19] etc.), however some of them were poorly motivated physically being just of purely mathematical nature [5] or having only empirical character [19, 20]. Such approach enables one-to-one correlation between the final values of the parameters of the criterion and the limit quantities obtained from the experiment. Despite its great practical meaning, such an approach makes no contribution to the research on the nature of material effort. Furthermore, mathematical form of the criterion (arbitrary chosen by author) often constrains it in such a way that it is not possible to account for some of the phenomena mentioned above. In case of physically motivated limit criteria by BURZYŃSKI [2] and RYCHLEWSKI [15], other problems occur. Strictly energy-based limit condition by Rychlewski as a quadratic function of stress cannot account for the strength differential. In case of Burzyński's hypothesis, some misstatements in the final formulation of the limit condition for anisotropic solids were recently found and discussed in [18].

1.2. General proposition of a yield criterion for anisotropic bodies exhibiting SD effect

In [11] the authors have introduced a new proposition of a limit condition for anisotropic materials with asymmetric elastic range. It was directly motivated by ideas of spectral decomposition of compliance tensor \mathbf{C} and elastic energy decompositions introduced by RYCHLEWSKI [15, 16] and the idea of stress state dependent influence functions introduced by BURZYŃSKI [2], which enabled him improvement of the classical HUBER–MISES [6] condition so that it accounted for the SD effect. It is stated that as a measure of material effort one can consider the following combination:

$$(1.1) \quad \eta_1 \Phi(\boldsymbol{\sigma}_1) + \dots + \eta_\chi \Phi(\boldsymbol{\sigma}_\chi), \quad \chi \leq 6$$

such that:

$$(1.2) \quad \begin{cases} \mathcal{T}_{\text{sym}}^2 = \mathcal{H}_1 \oplus \dots \oplus \mathcal{H}_\chi \\ \mathcal{H}_\alpha \perp \mathcal{H}_\beta \text{ for } \alpha \neq \beta \end{cases} \Rightarrow \begin{cases} \boldsymbol{\sigma} = \boldsymbol{\sigma}_1 + \dots + \boldsymbol{\sigma}_\chi, & \boldsymbol{\sigma}_\alpha \in \mathcal{H}_\alpha, \\ \boldsymbol{\sigma}_\alpha \bullet \boldsymbol{\sigma}_\beta = \boldsymbol{\sigma}_\alpha \cdot (\mathbf{C} \cdot \boldsymbol{\sigma}_\beta) = 0 & \text{for } \alpha \neq \beta, \end{cases}$$

where η_α is a certain stress-state dependent function. To keep mutual independence of the terms of the criterion, it is assumed that it depends only on the

stress state component corresponding with the proper elastic energy density σ_α (the projection of σ onto \mathcal{H}_α)

$$(1.3) \quad \eta_\alpha = \eta_\alpha(\sigma_\alpha)$$

and that it is isotropic in its domain (subspace \mathcal{H}_α), thus it can be expressed only in terms of invariants of σ_α

$$(1.4) \quad \eta_\alpha(\sigma_\alpha) = \eta_\alpha(I_1(\sigma_\alpha); I_2(\sigma_\alpha); I_3(\sigma_\alpha)).$$

More details can be found in [11].

Among all possible energetically orthogonal decompositions of the space of symmetric second order tensors $\mathcal{T}_{\text{sym}}^2 = \mathcal{H}_1 \oplus \dots \oplus \mathcal{H}_\chi$, the choice of the decomposition into eigensubspaces of compliance tensor \mathbf{C} is the best motivated both physically (due to clear physical interpretation of those subspaces) and mathematically (since it is the only decomposition of $\mathcal{T}_{\text{sym}}^2$ which is both orthogonal and energetically orthogonal).

2. GENERAL LIMIT CONDITION FOR PRESSURE-SENSITIVE, LODE ANGLE DEPENDENT ISOTROPIC BODIES EXHIBITING SD EFFECT

Even in case of the simplest materials, namely those macroscopically homogeneous and isotropic, such as modern alloys, many classical yield criteria (i.e. HUBER–MISES [6, 9], BURZYŃSKI [2], DRUCKER–PRAGER [3] etc.) fail to describe them correctly either due to lack of pressure-sensitivity or the Lode angle dependence. The special isotropic case of the yield criterion introduced above is found suitable for accounting for the influence of both the pressure and Lode's angle.

From the spectral decomposition of isotropic compliance tensor we obtain a one-dimensional subspace of spherical tensors (hydrostatic stresses) and five-dimensional subspace of deviators (shears). Energy density is decomposed into energy density of distortion Φ_f and energy density of volume change Φ_v . Yield condition (1.1) can be rewritten in the following form:

$$(2.1) \quad \tilde{\eta}_v(I_1(\mathbf{A}_\sigma); I_2(\mathbf{A}_\sigma); I_3(\mathbf{A}_\sigma))\Phi_v + \tilde{\eta}_f(J_1, J_2, J_3)\Phi_f = 1,$$

where \mathbf{A}_σ is the isotropic component of the stress tensor and J_1, J_2, J_3 are invariants of the stress tensor deviator. It is known that:

$$(2.2) \quad \begin{aligned} I_1(\mathbf{A}_\sigma) &= 3p, & I_2(\mathbf{A}_\sigma) &= 3p^2, & I_3(\mathbf{A}_\sigma) &= p^3, \\ J_1 &= 0, & J_2 &= \frac{1}{2}q^2, & J_3 &= \frac{1}{3\sqrt{6}}q^3 \cos(3\theta), \\ \Phi_v &= \frac{p^2}{2K}, & \Phi_f &= \frac{q^2}{4G}, \end{aligned}$$

where K is the Helmholtz bulk modulus, G is the Kirchhoff shear modulus, p is the hydrostatic stress, q deviatoric component of stress and θ is the Lode angle – they can be expressed in terms of stress state components in any coordinate system as well as in principal stresses:

$$\begin{aligned}
 p &= \frac{1}{3}(\sigma_{11} + \sigma_{22} + \sigma_{33}) = \frac{1}{3}(\sigma_1 + \sigma_2 + \sigma_3), \\
 q &= \sqrt{\frac{1}{3} [(\sigma_{22} - \sigma_{33})^2 + (\sigma_{33} - \sigma_{11})^2 + (\sigma_{11} - \sigma_{22})^2 + 6(\sigma_{23}^2 + \sigma_{31}^2 + \sigma_{12}^2)]} \\
 (2.3) \qquad &= \sqrt{\frac{1}{3} [(\sigma_2 - \sigma_3)^2 + (\sigma_3 - \sigma_1)^2 + (\sigma_1 - \sigma_2)^2]}, \\
 \theta &= \frac{1}{3} \arccos \left[\frac{3\sqrt{3}}{2} \frac{J_3}{(J_2)^{3/2}} \right].
 \end{aligned}$$

Please note that the second invariants of the spherical and deviatoric part of the stress tensor are proportional to the volumetric and distortional part of the elastic energy density respectively. Since all invariants of the hydrostatic component of the stress state depend on p , it is enough to state that $\eta_v = \eta_v(p)$. It is also clear that it is the third invariant of the stress tensor deviator which makes the qualitative, not only quantitative, distinction between various modes of shearing, so it is assumed that the influence function corresponding to the distortional part of energy density depends only on Lode angle θ . Including constant parameters (i.e. elastic moduli) in the influence functions, the limit condition (1.1) can be finally obtained in the following form:

$$(2.4) \qquad \eta_v(p)p^2 + \eta_f(\theta)q^2 = 1.$$

2.1. Influence functions

Many authors have been already considering various functions describing the influence of pressure or Lode's angle on the material effort. It seems that in case of pressure influence function, the one proposed by Burzyński is one of the most general – it enables description of various relations between hydrostatic and deviatoric stresses – linear, paraboloidal, hyperboloidal and elliptical. It is a two-parameter rational function of the following form:

$$(2.5) \qquad \eta_v(p) = \left(\omega + \frac{\delta}{p} \right).$$

There is a large variety of different functions describing the influence of the Lode angle – valuable summary of propositions of Lode angle dependences was

made by BARDET and published in [1]. Some other suggestions of the Lode angle influence function were also presented in [12]:

- Two-parameter power function (RANIECKI, MRÓZ [14])

$$\eta_f(\theta) = [1 + \alpha \cos(3\theta)]^\beta.$$

- Two-parameter exponential function (RANIECKI, MRÓZ [14])

$$\eta_f(\theta) = 1 + \alpha [1 - e^{-\beta(1+\cos(3\theta))}].$$

- One-parameter trigonometric function (LEXCELLENT [8])

$$\eta_f(\theta) = \cos \left[\frac{1}{3} \arccos [1 - \alpha(1 - \cos(3\theta))] \right].$$

- Two-parameter trigonometric function (PODGÓRSKI [13])

$$\eta_f(\theta) = \frac{1}{\cos(30^\circ - \beta)} \cos \left[\frac{1}{3} \arccos (\alpha \cdot \cos(3\theta)) - \beta \right].$$

It is often assumed that the Drucker's postulates are true – as a consequence of this assumption, the yield surface should be convex. Convexity condition for the limit surface determined by yield condition (2.4) for arbitrary chosen form of influence function was derived and will be published in the second part of the current paper [17].

3. LIMIT CRITERION SPECIFICATION

An attempt to specify the limit condition referring to experimental data available in the literature was made. A series of experiments performed by IYER, LISSENDEN [7] for Inconel 718 alloy was taken as the reference data. Analysis of the results obtained by Iyer and Lissenden, both in experiments and numerical simulation, lead to the choice of Burzyński's pressure influence function with $\omega = 0$ (paraboloid yield surface) and slightly modified Podgórski's Lode angle influence function with $\alpha = 0.8$, $\beta = 30^\circ$ – for details see [12]. The Levenberg–Marquardt algorithm was used to find the values of the rest of parameters of the criterion by optimal fitting the assumed surface to the twelve points obtained from the experiments. The final form of the yield criterion was obtained as follows:

$$(3.1) \quad \frac{q^2}{\cos(30^\circ - \beta)} \cos \left[\frac{1}{3} \arccos [\alpha \cdot \cos(3(\theta - 90^\circ))] - \beta \right] + \left(\omega + \frac{\delta}{p} \right) \cdot p^2 - H = 0,$$

where $\alpha = 0.8$, $\beta = 30^\circ$, $\delta = 215.95$ MPa, $\omega = 0$, $H = 201670.46$ MPa². The plot of the limit surface and its cross-sections at octahedral plane and BURZYŃSKI's plane [21] are given in Figs. 1–3. In the latter figure the cross-sections of the yield

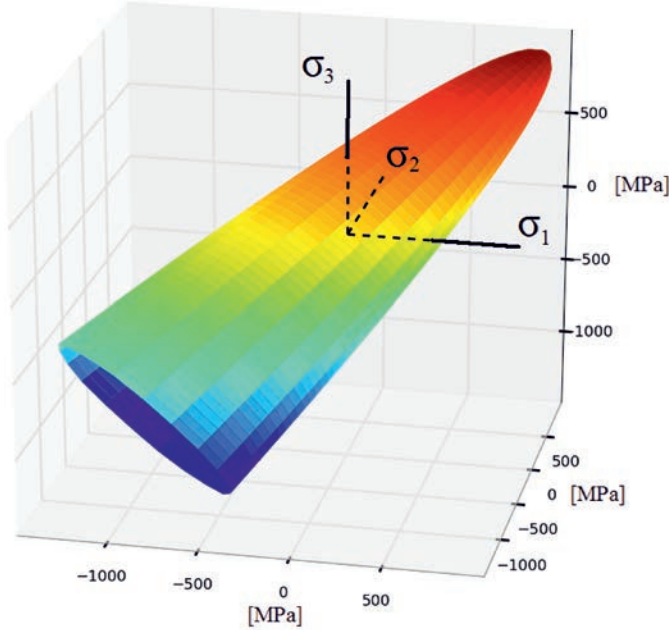


FIG. 1. Yield surface given by Eq. (3.1).

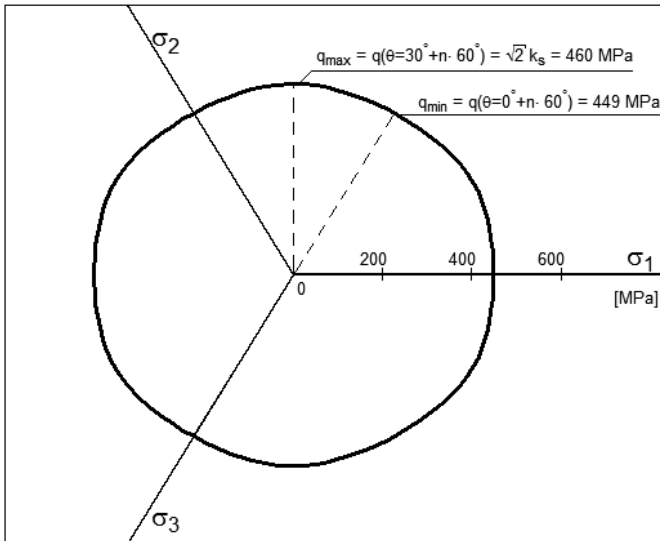


FIG. 2. Lode angle dependence – cross-section of the yield surface given by (3.1) at octahedral plane.

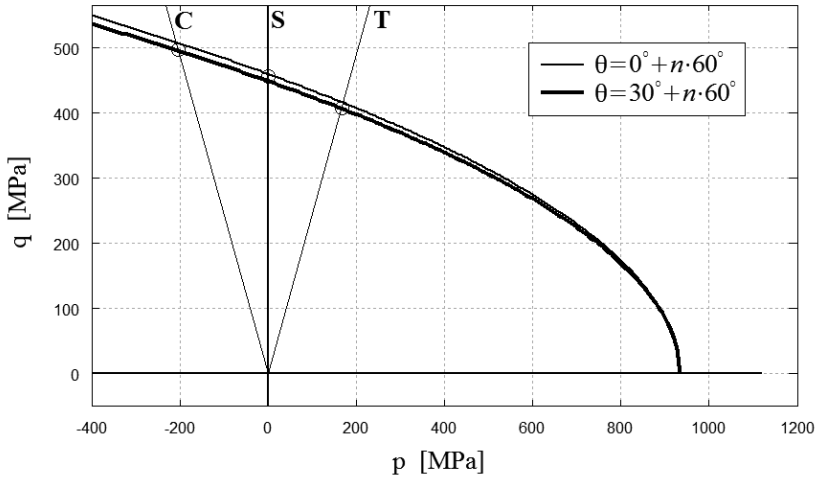


FIG. 3. Pressure-sensitivity – cross-section of the yield surface given by (3.1) at Burzyński's plane. Straight lines denoted C, S and T determine uniaxial compression, shear and uniaxial tensile stress states respectively.

surface (3.1) at Burzyński's plane for two values of the Lode angle is presented – $\theta = 0^\circ + n \cdot 60^\circ$ ($n \in \mathbb{N}$), which corresponds with uniaxial stress states, and $\theta = 30^\circ + n \cdot 60^\circ$ which corresponds with pure shears.

4. SUMMARY

A new proposition of a limit condition for the pressure-sensitive isotropic and homogeneous bodies exhibiting Lode's angle dependency and strength differential effect was presented. The straightforward derivation of the discussed yield criterion from the general idea of an energy-based limit condition for anisotropic bodies with asymmetric elastic range introduced by authors in [11] was shown. Some propositions of the pressure and Lode's angle influence functions were given. Condition for convexity of the yield surface corresponding with the discussed limit condition will be presented in the second part of the paper. Specification of the limit criterion for assumed influence functions referring to the experimental data published in [7] was presented.

ACKNOWLEDGMENT

The paper has been prepared within the framework of the research project N N501 1215 36 of the Ministry of Science and Higher Education of Poland.

REFERENCES

1. J. P. BARDET, *Lode dependences for isotropic pressure sensitive materials*, J. Appl. Mech., **57**, 498–506, 1990.
2. W. BURZYŃSKI, *Studium nad hipotezami wyężenia*, Akademia Nauk Technicznych, Lwów, 1928; see also: *Selected passages from Włodzimierz Burzyński's doctoral dissertation "Study on material effort hypotheses"*, Engng. Trans., **57**, 3–4, 185–215, 2009.
3. D. C. DRUCKER, W. PRAGER, *Soil mechanics and plastic analysis for limit design*, Quart. Appl. Math., **10**, 2, 157–165, 1952.
4. R. HILL, *A theory of the yielding and plastic flow of anisotropic metals*, Proc. Roy. Soc. London, **193**, 281–297, 1948.
5. O. HOFFMAN, *The brittle strength of orthotropic materials*, J. Comp. Mater., **1**, 200–206, 1967.
6. M. T. HUBER, *Właściwa praca odkształcenia jako miara wyężenia materiału*, Czasopismo Techniczne, 15, Lwów, 1904; see also: *Specific work of strain as a measure of material effort*, Arch. Mech., **56**, 3, 173–190, 2004.
7. S. K. IYER, C. J. LISSENDEN, *Multiaxial constitutive model accounting for the strength-differential in Inconel 718*, Int. J. Plast., **19**, 2055–2081, 2003.
8. C. LEXCELLENT, A. VIVET, C. BOUVET, S. CALLOCH, P. BLANC, *Experimental and numerical determinations of the initial surface of phase transformation under biaxial loading in some polycrystalline shape-memory alloys*, J. Mech. Phys. Sol., **50**, 2717–2735, 2002.
9. R. VON MISES, *Mechanik der festen Körper im plastisch deformablen Zustand*, Göttin. Nachr. Math. Phys., **1**, 582–592, 1913.
10. R. VON MISES, *Mechanik der plastischen Formänderung von Kristallen*, Z. Angew. Math. u. Mech., **8**, 161–185, 1928.
11. J. OSTROWSKA-MACIEJEWSKA, R. B. PĘCHERSKI, P. SZEPTYŃSKI, *Limit condition for anisotropic materials with asymmetric elastic range*, Engng. Trans. (submitted for publication).
12. R. B. PĘCHERSKI, P. SZEPTYŃSKI, M. NOWAK, *An extension of Burzyński hypothesis of material effort accounting for the third invariant of stress tensor*, Arch. Metall. Mat., **56**, 2, 503–508, 2011.
13. J. PODGÓRSKI, *Limit state condition and the dissipation function for isotropic materials*, Arch. Mech., **36**, 3, 323–342, 1984.
14. B. RANIECKI, Z. MRÓZ, *Yield or martensitic phase transformation conditions and dissipation functions for isotropic, pressure-insensitive alloys exhibiting SD effect*, Acta. Mech., **195**, 81–102, 2008.
15. J. RYCHLEWSKI, *"CEIHNOSSTTUV" Matematicheskaya struktura uprugih tel*, Preprint 217, IPM AN SSSR, Moscow, 1983.
16. J. RYCHLEWSKI, *Razlozheniya uprugoi energii i kriterii predelnosti*, Uspehi mehaniki, **7**, 51–80, 1984; see also: *Elastic energy decomposition and limit criteria*, Engn. Trans., **59**, 1, 31–63, 2011.

17. P. SZEPTYŃSKI, *Yield criterion accounting for the influence of the third invariant of stress tensor deviator. Part II: Analysis of convexity condition of the yield surface*, Engng. Trans., **59**, 4, 283–297, 2011.
18. P. SZEPTYŃSKI, *Some remarks on Burzyński's failure criterion for anisotropic materials*, Engng. Trans., **59**, 2, 119–136, 2011.
19. P. S. THEOCARIS, *The elliptic paraboloid failure criterion for cellular solids and brittle foams*, Acta Mech., **89**, 93–121, 1991.
20. S. W. TSAI, E. M. WU, *A general theory of strength for anisotropic materials*, J. Comp. Mater., **5**, 58–80, 1971.
21. M. ŻYCZKOWSKI, *Combined loadings in the theory of plasticity*, PWN, Warszawa, 1981.

Received July 7, 2011; revised version October 21, 2011.

YIELD CRITERION ACCOUNTING FOR THE INFLUENCE OF THE THIRD INVARIANT OF STRESS TENSOR DEVIATOR. PART II. ANALYSIS OF CONVEXITY CONDITION OF THE YIELD SURFACE

P. S z e p t y ń s k i

AGH University of Science and Technology
 Faculty of Mechanical Engineering and Robotics
 Department of Strength, Fatigue of Materials and Structures

Al. A. Mickiewicza 30, 30-059 Krakow, Poland
 e-mail: pszept@agh.edu.pl

General form of yield condition for isotropic and homogeneous bodies is considered in the paper. In the space of principal stresses, the limit condition is graphically represented by a proper regular surface which is assumed here to be at least of C^2 class. Due to Drucker's Postulate, the yield surface should be convex. General form of convexity condition of the considered surface is derived using methods of differential geometry. Parametrization of the yield surface is given, the first and the second derivatives of the position vector with respect to the chosen parameters are calculated, what enables determination of the tangent and unit normal vectors at given point, and also determination of the first and the second fundamental form of the considered surface. Finally the Gaussian and mean curvatures, which are given by the coefficients of the first and the second fundamental form as the invariants of the shape operator, are found. Convexity condition of the considered surface expressed in general in terms of the mean and Gaussian curvatures, is formulated for any form of functions determining the character of the surface.

Key words: yield surface, convexity condition.

1. INTRODUCTION

Let us consider ideally elastic-plastic material. In the range of elastic deformation, linear constitutive law (Hooke's Law) is considered true:

$$(1.1) \quad \begin{cases} \boldsymbol{\sigma} = \mathbf{S} \cdot \boldsymbol{\varepsilon} \\ \boldsymbol{\varepsilon} = \mathbf{C} \cdot \boldsymbol{\sigma} \\ \mathbf{C} \circ \mathbf{S} = \mathbf{I}^S \end{cases} \Leftrightarrow \begin{cases} \sigma_{ij} = S_{ijkl} \varepsilon_{kl} \\ \varepsilon_{ij} = C_{ijkl} \sigma_{kl} \\ S_{ijkl} C_{klmn} = \frac{1}{2} (\delta_{im} \delta_{jn} + \delta_{in} \delta_{jm}) \end{cases} \quad i, \dots, n = 1, 2, 3,$$

where $\boldsymbol{\sigma}$ and $\boldsymbol{\varepsilon}$ are the second order symmetric Cauchy stress tensor and infinitesimal strain tensor (symmetric part of the displacement gradient) respectively,

\mathbf{S} and \mathbf{C} are the fourth order symmetric stiffness and compliance tensors respectively and \mathbf{I}^S is the identity operator in the linear space of symmetric second order tensors. The range of validity of the Hooke's Law is defined by a general limit (yield) condition of form

$$(1.2) \quad W(\boldsymbol{\sigma}) < 0.$$

Plastic flow rule is assumed to be of the following form:

$$(1.3) \quad \dot{\boldsymbol{\varepsilon}}^p = \dot{\lambda} \boldsymbol{\partial}_{\boldsymbol{\sigma}} F \Leftrightarrow \dot{\varepsilon}_{ij}^p = \dot{\lambda} \frac{\partial F}{\partial \sigma_{ij}},$$

where $\dot{\boldsymbol{\varepsilon}}^p$ is the plastic strain rate tensor, F is the plastic potential.

In 1950's DRUCKER has introduced and developed a proposition of the idea of a stable plastic material [1]. Drucker stated that the material is stable if the total work performed by the increment of load through the caused displacement is non-negative. It is always fulfilled in case of elastic deformation. If the final stress reaches the limit state determined by the yield condition, then plastic deformation occurs and the Drucker's postulate can be written in form of the following inequality

$$(1.4) \quad dL = (\boldsymbol{\sigma} - \boldsymbol{\sigma}^0) \cdot d\boldsymbol{\varepsilon}^p \geq 0.$$

In particular, if the stress increment is infinitesimal, one can write simply:

$$(1.5) \quad dL = d\boldsymbol{\sigma} \cdot d\boldsymbol{\varepsilon}^p \geq 0.$$

Let us consider that the initial stress state is the limit stress-state. All limit states, which are given by the yield condition of general form $W(\boldsymbol{\sigma}) = 0$ are represented in the space of principal stresses as a three-dimensional surface. If no hardening is assumed, then any stress increment vector $d\boldsymbol{\sigma}$ connects two points, both of which belong to the surface. In case of an infinitesimal increment of stress at the limit state this is a tangent vector to the yield surface at the considered point. It can be shown that at current assumptions on the model of material, validity of Drucker's postulate requires that the flow rule (1.3) must be associated with the limit condition (1.2), namely $F(\boldsymbol{\sigma}) = W(\boldsymbol{\sigma})$ – then the infinitesimal strain increment vector corresponding to the considered stress increment is represented by a vector perpendicular to the yield surface. In this case, the Drucker's postulate (1.5) can be interpreted as a requirement of non-negativeness of the scalar product of tangent and normal vector at any point of the yield surface. It is equivalent to the statement that whole surface is non-concave. If the flow rule is not associated with the yield condition, convexity of the yield surface is often assumed as well.

The aim of this paper is to show the application of the general convexity analysis of three-dimensional surfaces in mechanics of solids. In particular, the convexity of a new yield surface for isotropic homogeneous solids proposed in the first part of the paper [3] is analyzed. As a result, a general form of convexity condition for arbitrary chosen form of pressure and Lode angle influence functions appearing in the proposed yield surface formulation is derived. Those conditions may be applied as an inequality constraints in an optimization problem of material identification. Material parameters determined in the process of fitting the results obtained from the simulation using assumed model to those obtained from experiment with use of the aforementioned condition, guarantee convexity of the determined yield surface.

General methodology of the differential geometry in the analysis of convexity of the given surface \mathcal{S} in E^3 is as follows:

- Surface parametrization

$$(1.6) \quad \mathbf{x} \in \mathcal{S} \rightarrow \mathbf{x} = \mathbf{x}(\alpha, \beta).$$

- Finding the tangent vectors (first derivatives of the position vector with respect to the chosen surface parameters) at any point

$$(1.7) \quad \begin{aligned} \mathbf{x}_\alpha &= \frac{\partial}{\partial \alpha} \mathbf{x}(\alpha, \beta), \\ \mathbf{x}_\beta &= \frac{\partial}{\partial \beta} \mathbf{x}(\alpha, \beta). \end{aligned}$$

- Finding the second derivatives of the position vector with respect to the chosen surface parameters at any point

$$(1.8) \quad \begin{aligned} \mathbf{x}_{\alpha\alpha} &= \frac{\partial^2}{\partial \alpha^2} \mathbf{x}(\alpha, \beta), \\ \mathbf{x}_{\beta\beta} &= \frac{\partial^2}{\partial \beta^2} \mathbf{x}(\alpha, \beta), \\ \mathbf{x}_{\alpha\beta} &= \frac{\partial^2}{\partial \alpha \partial \beta} \mathbf{x}(\alpha, \beta). \end{aligned}$$

- Finding the external unit normal vector at any point as a scaled cross-product of the tangent vectors

$$(1.9) \quad \boldsymbol{\nu} = \pm \frac{\mathbf{x}_\alpha \times \mathbf{x}_\beta}{|\mathbf{x}_\alpha \times \mathbf{x}_\beta|}.$$

- Determination of the coefficients of the first fundamental form referring to the tangent vectors

$$\begin{aligned}
 E &= \mathbf{x}_\alpha \cdot \mathbf{x}_\alpha, \\
 F &= \mathbf{x}_\alpha \cdot \mathbf{x}_\beta, \\
 G &= \mathbf{x}_\beta \cdot \mathbf{x}_\beta.
 \end{aligned}
 \tag{1.10}$$

- Determination of the coefficients of the second fundamental form referring to the normal vectors and second derivatives of the position vector

$$\begin{aligned}
 e &= \boldsymbol{\nu} \cdot \mathbf{x}_{\alpha\alpha}, \\
 f &= \boldsymbol{\nu} \cdot \mathbf{x}_{\alpha\beta}, \\
 g &= \boldsymbol{\nu} \cdot \mathbf{x}_{\beta\beta}.
 \end{aligned}
 \tag{1.11}$$

- Determination of the shape operator and its invariants – Gaussian curvature κ_G and mean curvature κ_M – in terms of the coefficients of the first and the second fundamental form

$$\begin{aligned}
 \kappa_G &= \frac{eg - f^2}{EG - F^2}, \\
 \kappa_M &= \frac{eG - 2fF + gE}{2(EG - F^2)}.
 \end{aligned}
 \tag{1.12}$$

- Formulation of the convexity condition in terms of Gaussian and mean curvatures:

$$\begin{aligned}
 \kappa_M &< 0, \\
 \kappa_G &> 0.
 \end{aligned}
 \tag{1.13}$$

2. CONVEXITY CONDITION FOR PROPOSED SURFACE

2.1. Proposition of yield condition for isotropic bodies

Let us recall a general yield condition discussed in Part I of the paper:

$$(2.1) \quad W: \tilde{\eta}_f \Phi_f + \tilde{\eta}_v \Phi_v - 1 = 0,$$

where Φ_f – density of energy of distortion, Φ_v – density of energy of volume change and $\tilde{\eta}_f$ and $\tilde{\eta}_v$ are certain stress state dependent functions called *influence functions*. Certain assumptions made on those functions, discussed in details in Part I, enable rewriting (2.1) in the following form:

$$(2.2) \quad W: \eta_f(\theta)q^2 + \eta_p(p) - 1 = 0,$$

where p – hydrostatic stress, q – deviatoric stress, θ – Lode angle. Parameters p , q , θ (Haigh-Westergaard coordinates/Lode parameters) are proportional to cylindrical coordinates (with the specified axis parallel to the p axis) in the space of principal stresses. There exists the one-to-one relation between “Cartesian” coordinates and Lode parameters:

$$(2.3) \quad \sigma_i = \sigma_i(p, q, \theta) \Rightarrow \begin{cases} \sigma_1 = p + \sqrt{\frac{2}{3}}q \cos(\theta), \\ \sigma_2 = p + \sqrt{\frac{2}{3}}q \cos\left(\theta - \frac{2\pi}{3}\right), \\ \sigma_3 = p + \sqrt{\frac{2}{3}}q \cos\left(\theta + \frac{2\pi}{3}\right), \end{cases} \quad i = 1, 2, 3$$

or equivalently:

$$(2.4) \quad \begin{cases} p = \frac{1}{3}(\sigma_1 + \sigma_2 + \sigma_3), & p \in (-\infty; \infty), \\ q = \sqrt{\frac{1}{3}[(\sigma_3 - \sigma_2)^2 + (\sigma_1 - \sigma_3)^2 + (\sigma_1 - \sigma_2)^2]}, & q > 0, \\ \theta = \frac{1}{3} \arccos \frac{\sqrt{2}(\sigma_1 - \sigma_2 - \sigma_3)(\sigma_2 - \sigma_3 - \sigma_1)(\sigma_3 - \sigma_1 - \sigma_2)}{[(\sigma_3 - \sigma_2)^2 + (\sigma_1 - \sigma_3)^2 + (\sigma_1 - \sigma_2)^2]^{3/2}} \\ \quad \quad \quad = \arctan \frac{\sqrt{3}(\sigma_2 - \sigma_3)}{2\sigma_1 - \sigma_2 - \sigma_3}, & \theta \in (0; 2\pi). \end{cases}$$

The difference between the influence functions denoted with and without tilde, is only in constant scaling parameters which are proportional to the stiffness moduli – shear modulus for $\tilde{\eta}_f$ and bulk modulus for $\tilde{\eta}_v$. Further distinction between $\tilde{\eta}_v$ and η_p is that η_p involves already term p^2 which is proportional to Φ_v – it has no influence on the derivation of the convexity condition since $\tilde{\eta}_v$ is otherwise only pressure-dependent. This simple substitutions simplify the derivation in great extent.

A general form of convexity condition for any form of influence functions will be derived in the paper. The derivation will base on classical methods of differential geometry, namely – convexity analysis of three-dimensional surfaces.

2.2. Surface parametrization

Typical methods mentioned above require calculating both the tangent and normal vectors of the surface. Tangent vectors can be obtained through differentiating position vector of a point on the surface. Three-dimensional regular

surface is in fact a two-dimensional differentiable manifold, thus position of any point belonging to the surface can be explicitly determined by at most two independent parameters. To avoid differentiating in curvilinear coordinate system, we should express the position vector in “Cartesian” coordinates of principal stresses, however each component of this vector should be expressed by two parameters determining the surface. Let us assume that those parameters are p and θ :

$$(2.5) \quad \sigma_i \in W \rightarrow \sigma_i = \sigma_i(p, \theta), \quad i = 1, 2, 3.$$

Then using condition (2.2) and relations (2.4) and remembering that q as the norm of the stress tensor deviator has to be positive, we can write:

$$(2.6) \quad q = \sqrt{\frac{1 - \eta_p(p)}{\eta_f(\theta)}}.$$

Physical interpretation of η_f should be used now – since distortional strains and shearing stresses which correspond with q are in the greatest extent responsible for material effort, one should expect that $\forall \theta \eta_f(\theta) > 0$ for any given p – it agrees with intuition and it is confirmed by experiments.

It should be also assumed that $\eta_p(p) \leq 1$. Indeed, since η_f is assumed to be positive then any stress state σ corresponding with arbitrarily chosen value of q is a limit state (it belongs to the limit surface W) only when $\eta_p(p) \leq 1$. If there exists such value of p equal p_0 for which $\eta_p(p_0) > 1$, then there exists no real q for which Eq. (2.2) is fulfilled and there is no point on the surface corresponding with such value of parameter p – only part of infinite domain of $p \in (-\infty; \infty)$ is used to parametrize the surface. Coordinates of any point belonging to W can be thus written as follows:

$$(2.7) \quad W : \begin{cases} \sigma_1(p; \theta) = p + \sqrt{\frac{2}{3}} \sqrt{\frac{1 - \eta_p(p)}{\eta_f(\theta)}} \cos(\theta), \\ \sigma_2(p; \theta) = p + \sqrt{\frac{2}{3}} \sqrt{\frac{1 - \eta_p(p)}{\eta_f(\theta)}} \cos\left(\theta - \frac{2\pi}{3}\right), \\ \sigma_3(p; \theta) = p + \sqrt{\frac{2}{3}} \sqrt{\frac{1 - \eta_p(p)}{\eta_f(\theta)}} \cos\left(\theta + \frac{2\pi}{3}\right). \end{cases}$$

2.3. First and second derivatives of the position vector, tangent and normal vectors

Since $W \in C^2$, having the position vector expressed by surface parameters, we can calculate now components of vectors tangent to the surface:

$$(2.8) \quad \frac{\partial \sigma_i}{\partial p} = 1 - \frac{1}{\sqrt{6\eta_f[1-\eta_p]}} \frac{\partial \eta_p}{\partial p} \cos(\theta + \alpha_i),$$

$$(2.9) \quad \frac{\partial \sigma_i}{\partial \theta} = -\sqrt{\frac{2}{3}[1-\eta_p][\eta_f]^{3/2}} \cdot \left[\eta_f \sin(\theta + \alpha_i) + \frac{1}{2} \frac{\partial \eta_f}{\partial \theta} \cos(\theta + \alpha_i) \right],$$

where $i = 1, 2, 3$ and $\alpha_1 = 0$, $\alpha_2 = -2\pi/3$, $\alpha_3 = 2\pi/3$. Further derivatives of position vector are equal

$$(2.10) \quad \frac{\partial^2 \sigma_i}{\partial p^2} = -\frac{\cos(\theta + \alpha_i)}{\sqrt{6\eta_f[1-\eta_p]^{3/2}}} \left[\frac{1}{2} \left(\frac{\partial \eta_p}{\partial p} \right)^2 + [1-\eta_p] \frac{\partial^2 \eta_p}{\partial p^2} \right],$$

$$(2.11) \quad \frac{\partial^2 \sigma_i}{\partial \theta^2} = -\sqrt{\frac{2[1-\eta_p]}{3[\eta_f]^5}} \cdot \left[-\eta_f \frac{\partial \eta_f}{\partial \theta} \sin(\theta + \alpha_i) + \frac{1}{4} \left(2\eta_f \frac{\partial^2 \eta_f}{\partial \theta^2} - 3 \left(\frac{\partial \eta_f}{\partial \theta} \right)^2 + 4[\eta_f]^2 \right) \cos(\theta + \alpha_i) \right],$$

$$(2.12) \quad \frac{\partial^2 \sigma_i}{\partial p \partial \theta} = \frac{1}{\sqrt{6[\eta_f]^3[1-\eta_p]}} \cdot \frac{\partial \eta_p}{\partial p} \cdot \left[\eta_f \sin(\theta + \alpha_i) + \frac{1}{2} \frac{\partial \eta_f}{\partial \theta} \cos(\theta + \alpha_i) \right].$$

Normal to the surface at a fixed point is perpendicular to any tangent vector at this point (see Fig. 1). Since tangent plane is a two-dimensional one, a basis

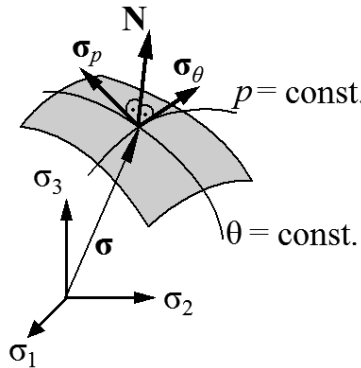


FIG. 1. Tangent and normal vectors at the given point of the surface.

in this space consists of two tangent vectors – i.e. those given by Eqs. (2.8) and (2.9). So the unit normal vector \mathbf{N} is parallel to the cross-product of those two:

$$(2.13) \quad \mathbf{N} = \frac{\nabla W}{|\nabla W|} = \frac{\boldsymbol{\sigma}_\theta \times \boldsymbol{\sigma}_p}{|\boldsymbol{\sigma}_\theta \times \boldsymbol{\sigma}_p|},$$

where $\boldsymbol{\sigma}_X$ denotes partial derivative of $\boldsymbol{\sigma}$ with respect to parameter X . The formula (2.13) specified with use of (2.8) and (2.9) leads after trigonometric simplification to the following final form. Just to make the notation clear, numerator and denominator are written separately. It is convenient to write the cross-product in the numerator as a sum of two vectors, one of which is parallel to the p axis:

$$(2.14) \quad \begin{aligned} \boldsymbol{\sigma}_\theta \times \boldsymbol{\sigma}_p &= \frac{\partial \eta_p}{\partial p} \cdot \frac{1}{2\sqrt{3}\eta_f} [1, 1, 1] \\ &\quad + \sqrt{\frac{1-\eta_p}{2[\eta_f]^3}} \left[\left(-\frac{\partial \eta_f}{\partial \theta} \sin(\theta) + 2\eta_f \cos(\theta) \right), \right. \\ &\quad \left. \left\{ \left(\sqrt{3}\eta_f + \frac{1}{2} \frac{\partial \eta_f}{\partial \theta} \right) \sin(\theta) + \left(-\eta_f + \frac{\sqrt{3}}{2} \frac{\partial \eta_f}{\partial \theta} \right) \cos(\theta) \right\}, \right. \\ &\quad \left. \left\{ \left(-\sqrt{3}\eta_f + \frac{1}{2} \frac{\partial \eta_f}{\partial \theta} \right) \sin(\theta) - \left(\eta_f + \frac{\sqrt{3}}{2} \frac{\partial \eta_f}{\partial \theta} \right) \cos(\theta) \right\} \right], \end{aligned}$$

$$(2.15) \quad \begin{aligned} L_N &= |\boldsymbol{\sigma}_\theta \times \boldsymbol{\sigma}_p| \\ &= \frac{1}{\eta_f^{3/2}} \sqrt{3(1-\eta_p) \left[\eta_f^2 + \frac{1}{4} \left(\frac{\partial \eta_f}{\partial \theta} \right)^2 \right] + \frac{1}{4} \left(\frac{\partial \eta_p}{\partial p} \right)^2 \eta_f} = L_N > 0. \end{aligned}$$

Please note that sequence of tangent vectors in the above vector cross-product influences the orientation of resultant normal vector (cross-product is bilinear skew-symmetric operation) which has significant role in convexity condition formulation. Interior of the yield surface (area of safe stress states) should be determined. The $(0,0,0)$ point should always be in the surface's interior. Let's check the orientation of a normal vector given by (2.13). At any point in the stress space (not only at those belonging to the surface), local orthonormal basis (holonomic basis respective for (p, q, θ) coordinates – see Fig. 2) can be determined, namely, these are normalized derivatives of a position vector given by (2.3) (not to be mistaken with position vector of a point belonging to the surface given by (2.7)) with respect to the corresponding parameter:

$$\begin{aligned}
 \mathbf{e}_p &= \frac{1}{\sqrt{3}}[1, 1, 1], \\
 \mathbf{e}_q &= \sqrt{\frac{2}{3}} \left[\cos(\theta), \cos\left(\theta - \frac{2\pi}{3}\right), \cos\left(\theta + \frac{2\pi}{3}\right) \right], \\
 \mathbf{e}_\theta &= \sqrt{\frac{2}{3}} \left[-\sin(\theta), -\sin\left(\theta - \frac{2\pi}{3}\right), -\sin\left(\theta + \frac{2\pi}{3}\right) \right], \\
 \mathbf{e}_K \cdot \mathbf{e}_L &= \delta_{KL}, \quad K, L = p, q, \theta.
 \end{aligned}
 \tag{2.16}$$

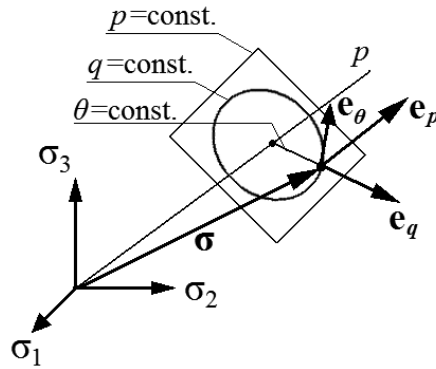


FIG. 2. Local holonomic basis respective for the Lode parameters p, q, θ .

The orientation of those vectors is already given and shown in the Fig. 2 and it is a consequence of definition (2.3) – \mathbf{e}_p is oriented along the hydrostatic stress axis pointing positive values of p – \mathbf{e}_q is oriented away from $(0, 0, 0)$ – and \mathbf{e}_θ is oriented counter-clockwise when looking at any octahedral plane (perpendicular to p axis) from the side of greater values of p . Due to the same reasons for which η_f was assumed to be positive valued, we can consider that an external normal is the one which q -component is oriented the same way as \mathbf{e}_q – safe stress states (interior of yield surface) are close to $(0, 0, 0)$ point or – more generally speaking – the safer is the stress state, the smaller should be its deviatoric component ($q \rightarrow 0$) and the closer should it be placed to the p axis. In such situation $\mathbf{N} \cdot \mathbf{e}_q > 0$ should be fulfilled. Indeed:

$$\mathbf{N} \cdot \mathbf{e}_q = \frac{\sqrt{3}}{L_N} \sqrt{\frac{(1 - \eta_p)}{\eta_f}},
 \tag{2.17}$$

which is always positive due to the assumed $1 \geq \eta_p$ and positiveness of L_N, η_f , so \mathbf{N} defined by (2.13) is an external normal.

2.4. First and second fundamental form, shape operator

Once the components of the normal vector and the tangent ones and their derivatives are calculated, one can obtain coefficients of the first and the second fundamental form and finally the values of curvatures which allow us to determine the convexity condition – typical methods of differential geometry shown e.g. in [2] will be used. The first fundamental form I is an inner (scalar) product of any two tangent vectors at a given point. As it was said before, tangent plane is a two-dimensional space in which vectors $\boldsymbol{\sigma}_p$ and $\boldsymbol{\sigma}_\theta$ form a basis (not necessarily an orthogonal or normalized one), so any two tangent vectors can be expressed as a linear combination of the two mentioned: $\mathbf{v}_1 = v_{1p}\boldsymbol{\sigma}_p + v_{1\theta}\boldsymbol{\sigma}_\theta$, $\mathbf{v}_2 = v_{2p}\boldsymbol{\sigma}_p + v_{2\theta}\boldsymbol{\sigma}_\theta$. Their scalar product is equal

$$(2.18) \quad I(\mathbf{v}_1, \mathbf{v}_2) = \mathbf{v}_1 \cdot \mathbf{v}_2 = v_{1p}v_{2p}(\boldsymbol{\sigma}_p \cdot \boldsymbol{\sigma}_p) + (v_{1p}v_{2\theta} + v_{1\theta}v_{2p})(\boldsymbol{\sigma}_p \cdot \boldsymbol{\sigma}_\theta) + v_{1\theta}v_{2\theta}(\boldsymbol{\sigma}_\theta \cdot \boldsymbol{\sigma}_\theta),$$

what can be rewritten in such matrix form:

$$(2.19) \quad I(\mathbf{v}_1, \mathbf{v}_2) = \mathbf{v}_1 \cdot \mathbf{v}_2 = \mathbf{v}_1 \cdot \mathbf{I} \cdot \mathbf{v}_2 = \begin{bmatrix} v_{1p} \\ v_{1\theta} \end{bmatrix}^T \cdot \begin{bmatrix} E & F \\ F & G \end{bmatrix} \cdot \begin{bmatrix} v_{2p} \\ v_{2\theta} \end{bmatrix}.$$

Symmetric operator \mathbf{I} can be considered as a metric tensor in the space of tangent vectors. Arc length of an infinitesimal section of a curve belonging to the surface is given as follows:

$$(2.20) \quad ds^2 = E dp^2 + 2F dp d\theta + G d\theta^2.$$

Coefficients of the first fundamental form are equal to

$$(2.21) \quad \begin{aligned} E &= |\boldsymbol{\sigma}_p|^2 = \boldsymbol{\sigma}_p \cdot \boldsymbol{\sigma}_p = 3 + \left(\frac{\partial \eta_f}{\partial p} \right)^2 \cdot \frac{1}{3\eta_f(1 - \eta_p)}, \\ F &= \boldsymbol{\sigma}_p \cdot \boldsymbol{\sigma}_\theta = \frac{1}{4(\eta_f)^2} \cdot \frac{\partial \eta_p}{\partial p} \cdot \frac{\partial \eta_f}{\partial \theta}, \\ G &= |\boldsymbol{\sigma}_\theta|^2 = \boldsymbol{\sigma}_\theta \cdot \boldsymbol{\sigma}_\theta = (1 - \eta_p) \left[\frac{1}{\eta_f} + \frac{1}{4(\eta_f)^3} \left(\frac{\partial \eta_f}{\partial \theta} \right)^2 \right]. \end{aligned}$$

Second fundamental form, just as the first one, is a bilinear form on tangent vectors at a given point of the surface defined as follows:

$$(2.22) \quad II(\mathbf{v}_1, \mathbf{v}_2) = \mathbf{S}(\mathbf{v}_1) \cdot \mathbf{v}_2,$$

where \mathbf{S} is shape operator defined as:

$$(2.23) \quad \mathbf{S} = (\mathbf{I} \mathbf{I} \mathbf{I}^{-1})^T = \begin{bmatrix} S_{11} & S_{12} \\ S_{21} & S_{22} \end{bmatrix} : \quad \mathbf{S}(\mathbf{v}) = -\mathbf{N}_{\mathbf{v}} = -\nabla \mathbf{N} \cdot \mathbf{v}.$$

Shape operator (Weingarten map, second fundamental tensor) describes variation of a unit normal of the surface with the change of direction of the tangent vector \mathbf{v} . Eigenvalues of the shape operator are equal principal (extremal) curvatures of the surface at a given point, while the corresponding eigenvectors indicate the directions of those curvatures. Invariants of the shape operator – determinant and half of the trace – are equal Gaussian and mean curvatures respectively. Second fundamental form II can be written as:

$$(2.24) \quad \begin{aligned} II(\mathbf{v}_1, \mathbf{v}_2) &= (-\mathbf{N}_{\mathbf{v}_1}) \cdot \mathbf{v}_2 \\ &= -(v_{1p}\mathbf{N}_p + v_{1\theta}\mathbf{N}_\theta) \cdot (v_{2p}\boldsymbol{\sigma}_p + v_{2\theta}\boldsymbol{\sigma}_\theta) = -v_{1p}v_{2p}(\mathbf{N}_p \cdot \boldsymbol{\sigma}_p) \\ &\quad - [v_{1p}v_{2\theta}(\mathbf{N}_p \cdot \boldsymbol{\sigma}_\theta) + v_{1\theta}v_{2p}(\mathbf{N}_\theta \cdot \boldsymbol{\sigma}_p)] - v_{1\theta}v_{2\theta}(\mathbf{N}_\theta \cdot \boldsymbol{\sigma}_\theta) \end{aligned}$$

or it can be rewritten in the following matrix form:

$$(2.25) \quad II(\mathbf{v}_1 \cdot \mathbf{v}_2) = \mathbf{v}_1 \cdot \mathbf{I} \mathbf{I} \cdot \mathbf{v}_2 = \begin{bmatrix} v_{1p} \\ v_{1\theta} \end{bmatrix}^T \cdot \begin{bmatrix} e & f \\ f & g \end{bmatrix} \cdot \begin{bmatrix} v_{2p} \\ v_{2\theta} \end{bmatrix},$$

where the coefficients of the second fundamental form are given by following relations:

$$(2.26) \quad \begin{aligned} e &= -\mathbf{N}_p \cdot \boldsymbol{\sigma}_p = \mathbf{N} \cdot \boldsymbol{\sigma}_{pp} = -\frac{\sqrt{3}}{2L_N\eta_f} \left[\frac{\partial^2 \eta_p}{\partial p^2} + \frac{1}{2} \left(\frac{\partial \eta_p}{\partial p} \right)^2 \frac{1}{(1-\eta_p)} \right], \\ f &= -\mathbf{N}_p \cdot \boldsymbol{\sigma}_\theta = -\mathbf{N}_\theta \cdot \boldsymbol{\sigma}_p = \mathbf{N} \cdot \boldsymbol{\sigma}_{p\theta} = \mathbf{N} \cdot \boldsymbol{\sigma}_{\theta p} = 0, \\ g &= -\mathbf{N}_\theta \cdot \boldsymbol{\sigma}_\theta = \mathbf{N} \cdot \boldsymbol{\sigma}_{\theta\theta} = -\frac{\sqrt{3}(1-\eta_p)}{4L_N[\eta_f]^3} \left[4(\eta_f)^2 + 2\eta_f \frac{\partial^2 \eta_f}{\partial \theta^2} - \left(\frac{\partial \eta_f}{\partial \theta} \right)^2 \right]. \end{aligned}$$

Components of \mathbf{S} can be expressed in terms of coefficients of the first and second fundamental form (Weingarten equations):

$$(2.27) \quad \begin{aligned} S_{11} &= \frac{eG - fF}{EG - F^2}, & S_{12} &= \frac{fG - gF}{EG - F^2}, \\ S_{21} &= \frac{fE - eF}{EG - F^2}, & S_{22} &= \frac{gE - fF}{EG - F^2}. \end{aligned}$$

*2.5. Invariants of \mathbf{S} , principal (extremal),
mean and Gaussian curvatures*

Since components of \mathbf{S} depend on the quantities chosen for parametrization, they are not as important as invariants of \mathbf{S} – its eigenvalues (principal curvatures – extremal of all possible values of curvature), its trace (which is proportional to the mean of the principal curvatures – mean curvature κ_M) and its determinant (product of principal curvatures – Gaussian curvature κ_G). Eigenvalues of \mathbf{S} can be found from the characteristic polynomial of \mathbf{S} :

$$(2.28) \quad \det(\mathbf{S} - \kappa \mathbf{I}) = \kappa^2 - I_1(\mathbf{S})\kappa + I_2(\mathbf{S}) = 0$$

or

$$(2.29) \quad \kappa^2 - 2\kappa_M\kappa + \kappa_G = 0,$$

where

$$(2.30) \quad \begin{aligned} \kappa_M &= \frac{1}{2}I_1(\mathbf{S}) = \frac{1}{2}\text{tr}(\mathbf{S}) = \frac{1}{2}\mathbf{I} \cdot (\mathbf{II})^{-1} = \frac{1}{2}(S_{11} + S_{22}) \\ &= \frac{eG - 2fF + gE}{2(EG - F^2)} - \text{mean curvature}, \\ \kappa_G &= I_2(\mathbf{S}) = \det(\mathbf{S}) = \frac{\det(\mathbf{I})}{\det(\mathbf{II})} = S_{11} \cdot S_{22} \\ &= \frac{eg - f^2}{EG - F^2} - \text{Gaussian curvature}. \end{aligned}$$

Values of mean and Gaussian curvatures:

$$(2.31) \quad \kappa_M = -\frac{\sqrt{3}}{4L_N\eta_f \left[3(1 - \eta_p) \left(\left(\frac{\partial\eta_f}{\partial\theta} \right)^2 + 4(\eta_f)^2 \right) + \eta_f \left(\frac{\partial\eta_p}{\partial p} \right)^2 \right]} \cdot \left[6(1 - \eta_p)\eta_f \left(2\eta_f \frac{\partial^2\eta_f}{\partial\theta^2} - \left(\frac{\partial\eta_f}{\partial\theta} \right)^2 + 4(\eta_f)^2 \right) + (1 - \eta_p) \frac{\partial^2\eta_p}{\partial p^2} \left(\left(\frac{\partial\eta_f}{\partial\theta} \right)^2 + 4(\eta_f)^2 \right) + \eta_f \left(\frac{\partial\eta_p}{\partial p} \right)^2 \left(\frac{\partial^2\eta_f}{\partial\theta^2} + 4\eta_f \right) \right],$$

$$(2.32) \quad \kappa_G = \frac{3 \left[2(1 - \eta_p) \frac{\partial^2\eta_p}{\partial p^2} + \left(\frac{\partial\eta_p}{\partial p} \right)^2 \right] \cdot \left[2\eta_f \frac{\partial^2\eta_f}{\partial\theta^2} - \left(\frac{\partial\eta_f}{\partial\theta} \right)^2 + 4(\eta_f)^2 \right]}{4L_N\eta_f \left[3(1 - \eta_p) \left(\left(\frac{\partial\eta_f}{\partial\theta} \right)^2 + 4(\eta_f)^2 \right) + \left(\frac{\partial\eta_p}{\partial p} \right)^2 \eta_f \right]}.$$

When there is a need of calculating extremal (the greatest and the smallest) values of curvature of all curvatures of any arbitrary chosen curves containing the given point and belonging to the surface, principal curvatures can be derived from mean and Gaussian curvatures. Since they are roots of characteristic polynomial, they are equal:

$$(2.33) \quad \kappa_{1/2} = \kappa_M \pm \sqrt{\kappa_M^2 + \kappa_G^2}.$$

These quantities are rather complex and it seems that writing of the full expression for principal curvatures for this very general case is to some extent useless – they can be calculated for certain forms of influence functions. Using numerical computations makes the problem even easier.

2.6. Convexity condition

If the yield surface is oriented by the aforementioned unit normal \mathbf{N} pointing exterior of the surface, then the surface will be convex (non-concave) if and only if all possible curvatures of the curves belonging to it are negative (non-positive). Since principal curvatures κ_1, κ_2 (as the eigenvalues of \mathbf{S}) are extremal (maximal and minimal), the values of curvature at given point then all curvatures will be negative if both of the principal ones are negative:

$$(2.34) \quad \begin{cases} \kappa_1 < 0 \\ \kappa_2 < 0 \end{cases} \Rightarrow \begin{cases} \kappa_1 + \kappa_2 < 0 \\ \kappa_1 \cdot \kappa_2 > 0 \end{cases} \Rightarrow \begin{cases} \kappa_M < 0 \\ \kappa_G > 0 \end{cases}.$$

Finally we obtain:

$$(2.35) \quad \begin{aligned} & \left[6\eta_f \left(2\eta_f \frac{\partial^2 \eta_f}{\partial \theta^2} - \left(\frac{\partial \eta_f}{\partial \theta} \right)^2 + 4(\eta_f)^2 \right) \right. \\ & \quad \left. + \frac{\partial^2 \eta_p}{\partial p^2} \left(\left(\frac{\partial \eta_f}{\partial \theta} \right)^2 + 4(\eta_f)^2 \right) + \frac{\eta_f}{(1-\eta_p)} \left(\frac{\partial \eta_p}{\partial p} \right)^2 \left(\frac{\partial^2 \eta_f}{\partial \theta^2} + 4\eta_f \right) \right] > 0, \\ & \left[2(1-\eta_p) \frac{\partial^2 \eta_p}{\partial p^2} + \left(\frac{\partial \eta_p}{\partial p} \right)^2 \right] \cdot \left[2\eta_f \frac{\partial^2 \eta_f}{\partial \theta^2} - \left(\frac{\partial \eta_f}{\partial \theta} \right)^2 + 4(\eta_f)^2 \right] > 0. \end{aligned}$$

These inequalities are general conditions which have to be fulfilled by the chosen influence functions, so that yield surface determined by them was convex. Since the yield condition (2.2) is formulated in a very general way, it allows us to use above conditions in the most cases of commonly used yield conditions and also to specify any new surface, since the form of influence functions can be chosen in an almost arbitrary way. Numerical analysis of positiveness of the

above expressions with respect to all constant parameters of influence functions, defines a domain of values of those parameters for which specified yield surface is convex (see similar analysis performed by RANIECKI and MRÓZ [4]).

As the process of material identification (determining functions and parameters describing properly material's behavior) is often considered as an optimization problem of fitting results of simulation using the assumed model to the data obtained from experiments (for certain objective function), conditions given by inequalities (2.35) can be used in the optimization process as the inequality constraints that have to be fulfilled by resultant optimal solution.

2.7. Pressure insensitive materials

Considering that the condition (2.2) describes pressure insensitive materials – what means that $\eta_p(p) = \text{const.}$ and all its derivatives are equal 0 – we can see that $\kappa_G = 0$. Resultant surface is a cylindrical shaped surface with its axis parallel to p -axis and its cross-section deformed by $\eta_f(\theta)$ influence function. Convexity condition is equivalent to the statement that mean curvature $\kappa_M < 0$:

$$(2.36) \quad 2\eta_f \frac{\partial^2 \eta_f}{\partial \theta^2} - \left(\frac{\partial \eta_f}{\partial \theta} \right)^2 + 4(\eta_f)^2 > 0.$$

Specific form of yield condition for pressure insensitive materials was considered by RANIECKI and MRÓZ in [4], namely $qf(y) - 1 = 0$ where $y = \cos(3\theta)$. We can obtain it by substituting $\eta_f(\theta) = [f(\cos(3\theta))]^2$ in (2.36). After proper differentiation we obtain:

$$(2.37) \quad f''(1 - y) - f'y + \frac{f}{9} > 0,$$

which is the form of convexity condition precisely analyzed by RANIECKI and MRÓZ in case of certain two-parameter power and exponential influence functions η_f .

For pressure insensitive materials it is common that yield condition is defined only on the octahedral plane thus the surface convexity condition requires only convexity of a function given on that plane. Since in many cases polar coordinates are convenient in use, sometimes yield condition has the form: $q = r(\theta)$, which can be obtained by substituting $\eta_f(\theta) = [r(\theta)]^{-2}$ into (2.36). After proper differentiation we obtain:

$$(2.38) \quad \kappa = \frac{r^2 + 2(r')^2 - rr''}{[(r')^2 + r^2]^{3/2}} > 0,$$

which is exactly the same as the classical expression for curvature of a function given in polar coordinates.

3. SUMMARY

Three-dimensional surface given by an equation in Haigh-Westergaard coordinates/Lode parameters (general form of yield condition for isotropic bodies) was considered. Condition of its convexity (being a consequence of Drucker postulate) was analyzed. Proper inequalities were formulated for arbitrary forms of influence functions using classical methods of differential geometry. Various forms of convexity condition were proposed depending on yield condition formulation and on various assumptions on properties of the influence function.

ACKNOWLEDGMENT

I would like to thank especially Mr. A. Karafiat from the Cracow University of Technology for his kind help in the studies on the presented convexity condition. The paper has been prepared within the framework of the research project N N501 1215 36 of the Ministry of Science and Higher Education of Poland.

REFERENCES

1. D. C. DRUCKER, *A more fundamental approach to plastic stress-strain relations*, Proceedings of the first US congress of applied mechanics, American Society of Mechanical Engineers, 487–491, 1952.
2. A. GRAY, *Modern Differential Geometry of Curves and Surfaces with Mathematica*, 2nd ed. Boca Raton, FL: CRC Press, 1997.
3. M. NOWAK, J. OSTROWSKA-MACIEJEWSKA, R. B. PEŁCHERSKI, P. SZEPTYŃSKI, *Yield criterion accounting for the third invariant of stress tensor deviator. Part I. Derivation of the yield condition basing on the concepts of energy-based hypotheses of Rychlewski and Burzyński*, Engng. Trans., **59**, 4, 273–281, 2011.
4. B. RANIECKI, Z. MRÓZ, *Yield or martensitic phase transformation conditions and dissipation functions for isotropic, pressure-insensitive alloys exhibiting SD effect*, Acta Mech., **195**, 81–102, 2008.

Received July 1, 2011; revised version October 21, 2011.

MICROMECHANICS OF LOCALIZED FRACTURE PHENOMENA IN INELASTIC SOLIDS GENERATED BY IMPACT-LOADED ADIABATIC PROCESSES

P. P e r z y n a

**Institute of Fundamental Technological Research
Polish Academy of Sciences**

Pawińskiego 5B, 02-106 Warszawa, Poland
e-mail: pperzyna@ippt.gov.pl

The main objective of the present paper is to discuss very efficient procedure of the numerical investigation of localized fracture in inelastic solids generated by impact-loaded adiabatic processes. Particular attention is focused on the proper description of a ductile mode of fracture propagating along the shear band for high impact velocities. This procedure of investigation is based on utilization the finite difference method for regularized thermo-elasto-viscoplastic constitutive model of damaged material. A general constitutive model of thermo-elasto-viscoplastic damaged polycrystalline solids with a finite set of internal state variables is used. The set of internal state variables consists of two scalars, namely equivalent inelastic deformation and volume fraction porosity. The equivalent inelastic deformation can describe the dissipation effects generated by viscoplastic flow phenomena and the volume fraction porosity takes into account the microdamage evolution effects. The relaxation time is used as a regularization parameter. Fracture criterion based on the evolution of microdamage is assumed.

As a numerical example we consider dynamic shear band propagation and localized fracture in an asymmetrically impact-loaded prenotched thin plate. The impact loading is simulated by a velocity boundary condition which are the results of dynamic contact problem. The separation of the projectile from the specimen, resulting from wave reflections within the projectile and the specimen, occurs in the phenomenon.

A thin shear band region of finite width which undergoes significant deformation and temperature rise has been determined. Its evolution until occurrence of final fracture has been simulated. Shear band advance, microdamage and the development of the temperature field as a function of time have been determined. Qualitative comparison of numerical results with experimental observation data has been presented. The numerical results obtained have proven the usefulness of the thermo-elasto-viscoplastic theory in the investigation of dynamic shear band propagations and localized fracture.

Key words: localized fracture, finite difference method, thermo-elasto-viscoplasticity, microdamage.

1. PROLOGUE

In technological processes fracture can occur as a result of an adiabatic shear band localization generally attributed to a plastic instability generated by in-

trinsic microdamage mechanisms within a material and thermal softening during plastic deformation.

Recent experimental observations have shown that the shear band procreates in a region of a body deformed where the resistance to plastic deformation is lower and the predisposition for localized shear band formation is higher. In the explanation of the fracture phenomenon along shear band regions very important role has the microdamage process which consists of the nucleation, growth and coalescence of microcracks. It has been found experimentally that in dynamic processes the shear band regions behave differently than adjacent zones. Within the shear band region the deformation process is characterized by very large strains (shear band strains over 100%) and very high strain rates (10^4 – 10^6 s⁻¹). The strain rate sensitivity of a material becomes very important feature of the shear band region and the microdamage process is intensified. The mechanism of final failure is a simple propagation of a macrocrack along the damaged material within the shear band region.

The main objective of the present paper is to discuss very efficient procedure of the numerical investigation of localized fracture in inelastic solids generated by impact-loaded adiabatic processes. Particular attention is focused on the proper description of a ductile mode of fracture propagating along the shear band for high impact velocities.

This procedure of investigation is based on utilization the finite difference method for regularized thermo-elasto-viscoplastic constitutive model of damaged material.

In this paper emphasis is laid on experimental and physical foundations as well as on mathematical constitutive modelling for the description of polycrystalline solids in modern technological processes. Our aim is twofold. First, particular attention will be focused on the fundamental mathematical analysis of the initial-boundary value problem (the evolution problem) and its proper numerical solution. We shall discuss the well-posedness of the evolution problem, its discretization in space and time, its approximated scheme, and its consistency, stability and convergence. Second, very important part of the discussion will also concern the physical aspects of the dispersion waves in considered numerical example. It will be proved that dispersive waves have a great influence on the results concerning the evolution of adiabatic shear bands as well as the propagation of the macrocrack path. It will be shown that cooperative phenomena generated by the interaction of dispersive and dissipative effects influence the final results concerning localized fracture of the considered specimen.

A general constitutive model of thermo-elasto-viscoplastic damaged polycrystalline solids with a finite set of internal state variables is used. The set of internal state variables consists of two scalars, namely equivalent inelastic deformation and volume fraction porosity. The equivalent inelastic deformation can

describe the dissipation effects generated by viscoplastic flow phenomena and the volume fraction porosity takes into account the microdamage evolution effects. The relaxation time is used as a regularization parameter. Fracture criterion based on the evolution of microdamage is assumed cf. PERZYNA [37–39, 42–44].

The identification procedure for the material functions and constants involved in the constitutive equations is developed basing on the experimental observations of adiabatic shear bands in an AISI 4340 steel presented by CHAKRABARTI and SPRETNAK [2].

We idealize the initial-boundary value problem investigated experimentally by CHAKRABARTI and SPRETNAK [2] by assuming the velocity driven process for a thin steel (AISI 4340) plate.

Base on the best curve fitting of the experimental results obtained by CHAKRABARTI and SPRETNAK [2] for the stress-strain relation the identification of the material constants has been done. The investigation of the stability and convergence of the numerical method based on the finite difference discretization has been presented, cf. DORNOWSKI and PERZYNA [11].

As a numerical example let us consider dynamic shear band propagation and localized fracture in an asymmetrically impact-loaded prenotched thin plate, cf. DORNOWSKI and PERZYNA [13]. The plate is made of an AISI 4340 steel. A notch (250 μm wide) is further extended by 2 mm and is situated unsymmetrically on the edge. The constant velocity $V_0 = 38$ m/s is imposed for projectile. The projectile comes into contact with the specimen over the width of 50 mm.

The impact loading is simulated by a velocity boundary condition which are the results of dynamic contact problem. The velocity imposed in specimen in front of projectile increases during the process. The separation of the projectile from the specimen, resulting from wave reflections within the projectile and the specimen, occurs in the phenomenon. All surface areas have traction free boundary conditions except where the velocity boundary condition is applied. We idealize the initial boundary value problem observed experimentally in GUDURU, ROSAKIS and RAVICHANDRAN [21], by assuming the velocity boundary condition and different material of the specimen. The discretization parameters are assumed in such a way, to solve the problem of mesomechanics properly. The dimension of the accepted mesh is of order 20 μm . A thin shear band region of finite width which undergoes significant deformation and temperature rise has been determined. Its evolution until occurrence of final fracture has been simulated.

Shear band advance as a function of time, the evolution of the Mises stress, equivalent plastic deformation, temperature, the microdamage and the crack path in the fracture region have been determined. Very important result is obtained for the evolution of temperature. The distribution of temperature along

shear band is nonuniform, cf. also GLEMA, ŁODYGOWSKI and PERZYNA [20]. This result is in agreement with the experimental observations presented by GUDURU, ROSAKIS and RAVICHANDRAN [21]. They observed that the temperature distribution along the shear band is highly nonuniform, with discrete regions of high temperature, that look like “hot spots”. The evolution of the microdamage and the crack path is very irregular and it widens steadily. It seems that in some places of the crack we can expect the branching effect as it has been observed by GUDURU, ROSAKIS and RAVICHANDRAN [21]. Qualitative comparison of numerical results with experimental observation data has been presented. The numerical results obtained have proven the usefulness of the thermo-elasto-viscoplastic theory in the numerical investigation of dynamic shear band propagation and localized fracture.

2. PHYSICAL AND EXPERIMENTAL MOTIVATION

2.1. Analysis of meso- and micro-mechanical problems

In modern technology we observe recently very important application of metals, ceramics and polymers at meso- and micro-scales. Micromachines are in this size range clearly will be of increasing technological significance. Processes that control the mechanical integrity of microelectronic devices take also place on this size scale, cf. NEEDLEMEN [31] and HUTCHINSON [24].

It is considerable experimental evidence that plastic flow and particularly localization of plastic deformation and localized fracture phenomena in crystalline solids are inherently size dependent over meso- and micro-scales. It is generally accepted that: “smaller is stronger” or “smaller is harder”.

Plastic behaviour at micro-scale range can not be characterized by conventional plasticity theories because they incorporate no material length scale and predict no size effect.

In recent years a variety of theoretical frameworks is emerging to describe inelastic deformation at the meso- and micro-scales. Four such frameworks (constitutive structures), each involving a length scale, are as follows: (i) discrete dislocation plasticity; (ii) nonlocal plasticity; (iii) the coupling of matter diffusion and deformation; (iv) elasto-viscoplasticity.

The meso- and micro-mechanical problems pose also numerical challenges. Computations on smaller size scale require smaller time steps. Since size dependent phenomena come into play when there are gradients of deformation and stress, hence numerical methods are usually needed to obtain solutions. Finite strains and rotations have to be taken into consideration.

At the meso- and micro-scale problems the dominant numerical methods are the finite element and finite difference methods.

It is noteworthy to add that the meso- and micro-scale continuum mechanics is in an early stage of development, both in terms of the theoretical framework as well as the computational methods.

In our consideration we shall use the thermo-elasto-viscoplasticity as a constitutive model of the material and apply the finite difference method in numerical computations.

2.2. Experimental investigation of the initiation and propagation of shear bands

GUDURU, ROSAKIS and RAVICHANDRAN [21] presented an experimental investigation of the initiation and propagation characteristics of dynamic shear band in C300 maraging steel. An elastic discharge machining (EDM) notch (260 μm wide) was further extended by 2 mm by fatigue loading, cf. Fig. 1.

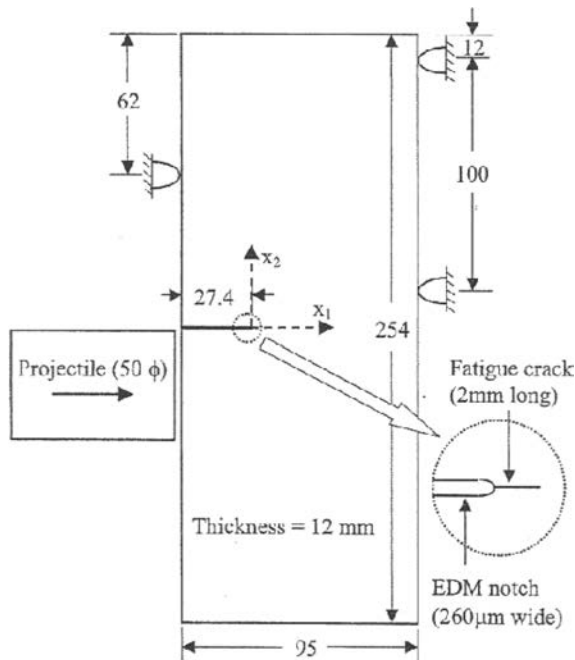


FIG. 1. Specimen geometry and impact arrangement. The projectile is 127 mm long. All dimensions shown are in millimeters (after GUDURU, ROSAKIS and RAVICHANDRAN [21]).

In experimental investigation of GUDURU, ROSAKIS and RAVICHANDRAN [21], two diagnostic techniques were used to observe the crack tip, the propagating shear band and the temperature field evolution during the initiation and propagation of the shear band. On one side of the specimen, the optical technique of coherent gradient sensing (CGS) in reflection was used to monitor the evo-

lution of the stress intensity factors as a function of time. On the other side of specimen, a newly developed full-field, high-speed infrared (IR) imaging system was employed to measure the evolving, 2-D temperature field, cf. Fig. 2. They measure the advance of the shear band and its velocity in five different experiments, cf. Fig. 3 and 4. The shear band velocity can be seen to be highly

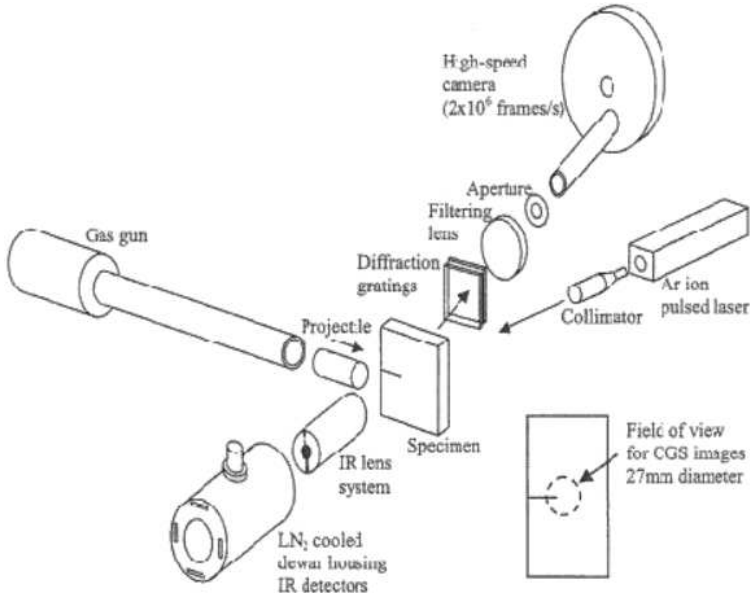


FIG. 2. Schematic illustration of the experimental setup. The CGS setup measures the out plane displacement gradients on the rear side of the specimen. Simultaneous thermal imaging is accomplished using the IR camera on the facing side of the specimen (after GUDURU, ROSAKIS and RAVICHANDRAN [21]).

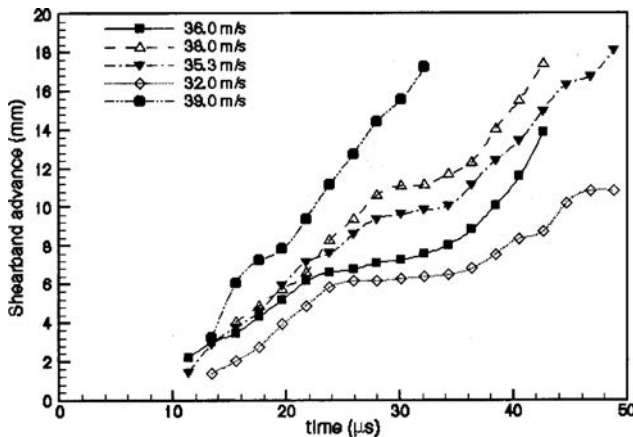


FIG. 3. Shear band advance as a function of time (after GUDURU, ROSAKIS and RAVICHANDRAN [21]).

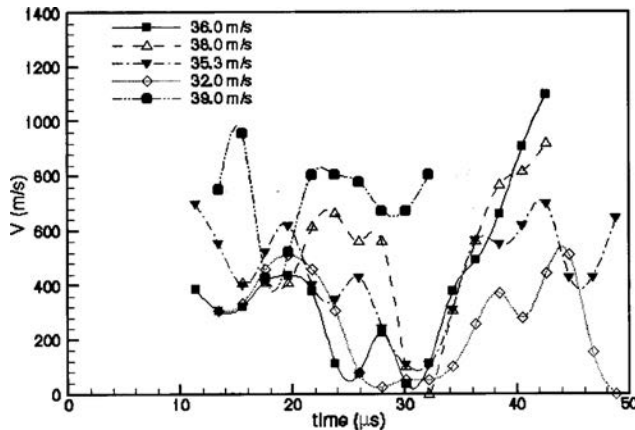


FIG. 4. Shear band velocity as a function of time (after GUDURU, ROSAKIS and RAVICHANDRAN [21]).

transient and a function of the impact speed. In all but one experiment, the band arrests momentarily at about 30 μs , before accelerating to high speeds. The maximum shear band velocity observed here is about 1100 m/s, cf. also ZHOU *et al.* [57, 58].

2.3. Fracture phenomena along localized shear bands

Fractured specimens were examined using an optical microscope to study the features of the shear bands such as its width, trajectory, the fracture surface, etc. The shear band is revealed as a white stripe. The thickness of the band is about 40 μm , cf. Fig. 5. A scanning electron microscope (SEM) image of the specimen surface that failed by shear band propagation, shows elongated voids, with sheared edges that are characteristic of such a failure mode, cf. Fig. 6. The presence of voids reveals the development of triaxiality tensile stress state that led to void growth and eventual fracture.

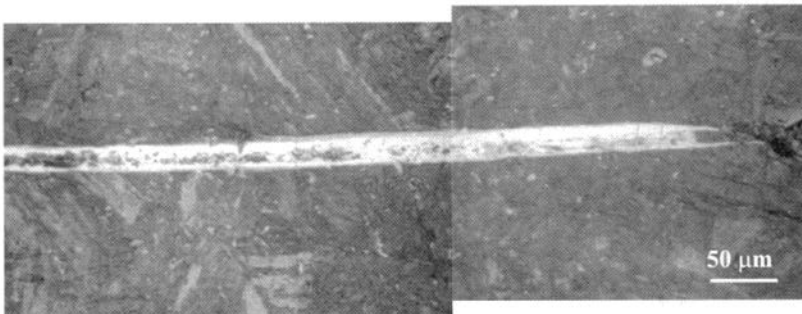


FIG. 5. An optical micrograph of an arrested shear band (after GUDURU, ROSAKIS and RAVICHANDRAN [21]).

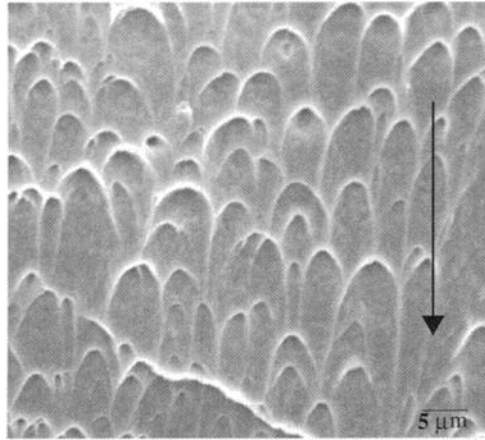


FIG. 6. An SEM image of the fracture surface that failed by shear banding. Arrow shows the crack propagation direction (after GUDURU, ROSAKIS and RAVICHANDRAN [21]).

2.4. Temperature measurement

GUDURU, ROSAKIS and RAVICHANDRAN [21] (cf. also GUDURU *et al.* [22]) performed also broad experimental observations of the temperature field evolution during the initiation and propagation of the shear band. One of their objectives of imaging the temperature field was to visualize the development of the plastic zone at the tip of the initial crack and to observe its evolution, through further localization, into a shear band. The IR camera was focussed at the tip of the fatigue crack as illustrated on the left-hand side of Fig. 7. The impact

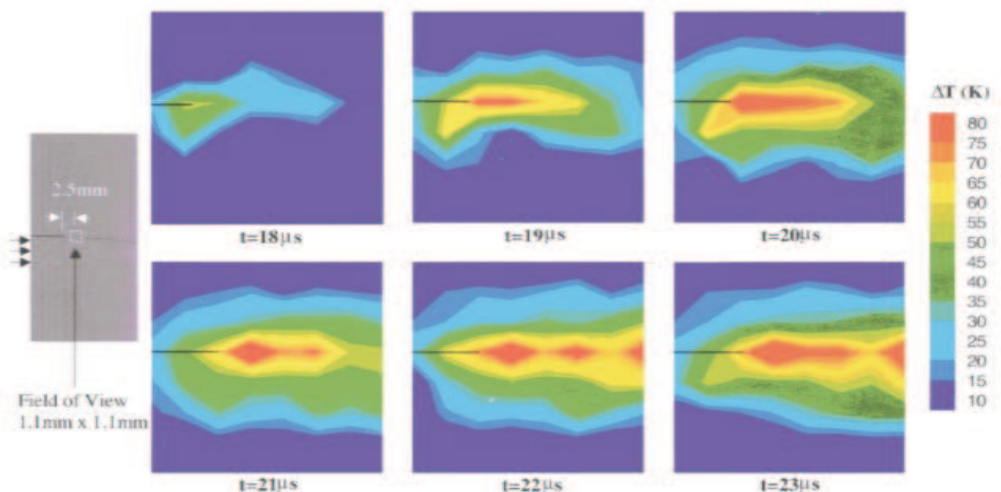


FIG. 7. A sequence of thermal images showing the transition of crack tip plastic zone into a shear band (after GUDURU, ROSAKIS and RAVICHANDRAN [21]).

speed was 35 m/s. They show a sequence of thermal images revealing the development of the temperature field as a function of time. Starting at about 21 μ s, the central hot region extends to the right, as indicated by the contour lines, signifying the process of shear localization. The measured highest temperature rise within the plastic zone when this happened was at least 80 K, cf. Fig. 7.

Let us now focus our attention on the temperature field associated with the tip of a propagating shear band. The gradual nature of temperature rise at the front end of shear band supports the notion of a very diffuse shear band tip, as opposed to a crack tip which carries a strong singularity in the field quantities.

As the shear band propagates, the material within the band progressively accumulates large plastic shear strains within short times and the temperature can quickly reach very high value. Of special interest in the investigation of GUDURU, ROSAKIS and RAVICHANDRAN [21] has been the temperature distribution along a well-defined shear band. They have been consistently observed, in all experiments where a propagating shear band was imaged, that the temperature distribution along the band is highly non-uniform, with discrete regions of high temperature, that look like “hot spots”. These hot spots are also seen to translate along the length of the band.

2.5. Possible shear band branching

GUDURU, ROSAKIS and RAVICHANDRAN [21] discussed also the possibility of shear band branching. Figure 8 shows their three micrographs that confirm previous observation about the possibility of shear band branching mode by

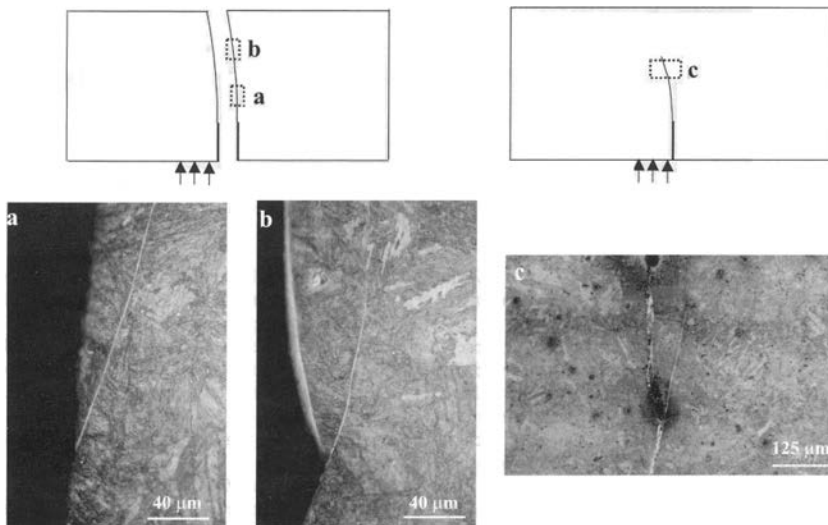


FIG. 8. Optical micrographs of possible shear band bifurcation (after GUDURU, ROSAKIS and RAVICHANDRAN [21]).

MEYERS [30]. In the first two, the left edges are the failure paths, caused by a propagating shear band. The third image is taken from an arrested shear band. The branching behaviour is clearly seen in all three cases. They added that currently there is no theoretical framework to explain such a phenomenon and they stressed that this interesting observation requires further investigation to understand the conditions under which such a bifurcation can take place.

3. THERMO-ELASTO-VISCOPLASTIC MODEL OF A MATERIAL

3.1. Basic assumptions and definitions

Let us assume that a continuum body is an open bounded set $\mathcal{B} \subset \mathbb{R}^3$, and let $\phi : \mathcal{B} \rightarrow \mathcal{S}$ be a C^1 configuration of \mathcal{B} in \mathcal{S} . The tangent of ϕ is denoted $\mathbf{F} = T\phi$ and is called the deformation gradient of ϕ .

Let $\{X^A\}$ and $\{x^a\}$ denote coordinate systems on \mathcal{B} and \mathcal{S} respectively. Then we refer to $\mathcal{B} \subset \mathbb{R}^3$ as the reference configuration of a continuum body with particles $X \in \mathcal{B}$ and to $\mathcal{S} = \phi(\mathcal{B})$ as the current configuration with points $\mathbf{x} \in \mathcal{S}$. The matrix $\mathbf{F}(\mathbf{X}, t) = \partial\phi(\mathbf{X}, t)/\partial\mathbf{X}$ with respect to the coordinate bases $\mathbf{E}_A(\mathbf{X})$ and $\mathbf{e}_a(\mathbf{x})$ is given by

$$(3.1) \quad F_A^a(\mathbf{X}, t) = \frac{\partial\phi^a}{\partial X^A}(\mathbf{X}, t),$$

where a mapping $\mathbf{x} = \phi(\mathbf{X}, t)$ represents a motion of a body \mathcal{B} .

We consider the local multiplicative decomposition

$$(3.2) \quad \mathbf{F} = \mathbf{F}^e \cdot \mathbf{F}^p,$$

where $(\mathbf{F}^e)^{-1}$ is the deformation gradient that releases elastically the stress on the neighbourhood $\phi(\mathcal{N}(\mathbf{X}))$ in the current configuration.

Let us define the total and elastic Finger deformation tensors

$$(3.3) \quad \mathbf{b} = \mathbf{F} \cdot \mathbf{F}^T, \quad \mathbf{b}^e = \mathbf{F}^e \cdot \mathbf{F}^{eT},$$

respectively, and the Eulerian strain tensors as follows

$$(3.4) \quad \mathbf{e} = \frac{1}{2}(\mathbf{g} - \mathbf{b}^{-1}), \quad \mathbf{e}^e = \frac{1}{2}(\mathbf{g} - \mathbf{b}^{e-1}),$$

where \mathbf{g} denotes the metric tensor in the current configuration.

By definition¹⁾

$$(3.5) \quad \mathbf{e}^p = \mathbf{e} - \mathbf{e}^e = \frac{1}{2}(\mathbf{b}^{e-1} - \mathbf{b}^{-1})$$

we introduce the plastic Eulerian strain tensor.

¹⁾For precise definition of the finite elasto-plastic deformation see PERZYNA [41].

To define objective rates for vectors and tensors we use the Lie derivative²⁾. Let us define the Lie derivative of a spatial tensor field \mathbf{t} with respect to the velocity field \mathbf{v} as

$$(3.6) \quad \mathbf{L}_{\mathbf{v}}\mathbf{t} = \phi_* \frac{\partial}{\partial t} (\phi^* \mathbf{t}),$$

where ϕ^* and ϕ_* denote the pull-back and push-forward operations, respectively.

The rate of deformation tensor is defined as follows

$$(3.7) \quad \mathbf{d}^b = \mathbf{L}_{\mathbf{v}}\mathbf{e}^b = \frac{1}{2} \mathbf{L}_{\mathbf{v}}\mathbf{g} = \frac{1}{2} (g_{ac} v^c |_{|b} + g_{cb} v^c |_{|a}) \mathbf{e}^a \otimes \mathbf{e}^b,$$

where the symbol $|_{|b}$ denotes the index lowering operator and \otimes the tensor product,

$$(3.8) \quad v^a |_{|b} = \frac{\partial v^a}{\partial x^b} + \gamma_{bc}^a v^c,$$

and γ_{bc}^a denotes the Christoffel symbol for the general coordinate systems $\{x^a\}$. The components of the spin $\boldsymbol{\omega}$ $\boldsymbol{\omega}$ are given by

$$(3.9) \quad \omega_{ab} = \frac{1}{2} (g_{ac} v^c |_{|b} - g_{cb} v^c |_{|a}) = \frac{1}{2} \left(\frac{\partial v_a}{\partial x^b} - \frac{\partial v_b}{\partial x^a} \right).$$

Similarly

$$(3.10) \quad \mathbf{d}^{e^b} = \mathbf{L}_{\mathbf{v}}\mathbf{e}^{e^b}, \quad \mathbf{d}^{p^b} = \mathbf{L}_{\mathbf{v}}\mathbf{e}^{p^b},$$

and

$$(3.11) \quad \mathbf{d} = \mathbf{d}^e + \mathbf{d}^p.$$

Let $\boldsymbol{\tau}$ denote the Kirchhoff stress tensor related to the Cauchy stress tensor $\boldsymbol{\sigma}$ by

$$(3.12) \quad \boldsymbol{\tau} = J\boldsymbol{\sigma} = \frac{\rho_{\text{Ref}}}{\rho} \boldsymbol{\sigma},$$

where the Jacobian J is the determinant of the linear transformation $\mathbf{F}(\mathbf{X}, t) = (\partial/\partial X)\phi(\mathbf{X}, t)$, $\rho_{\text{Ref}}(\mathbf{X})$ and $\rho(\mathbf{x}, t)$ denote the mass density in the reference and current configuration, respectively.

The Lie derivative of the Kirchhoff stress tensor $\boldsymbol{\tau} \in \mathbf{T}^2(\mathcal{S})$ (elements of $\mathbf{T}^2(\mathcal{S})$ are called tensors on \mathcal{S} , contravariant of order 2) gives

$$(3.13) \quad \begin{aligned} \mathbf{L}_{\mathbf{v}}\boldsymbol{\tau} = \phi_* \frac{\partial}{\partial t} (\phi^* \boldsymbol{\tau}) &= \left\{ \mathbf{F} \cdot \frac{\partial}{\partial t} [\mathbf{F}^{-1} \cdot (\boldsymbol{\tau} \circ \phi) \cdot \mathbf{F}^{-1T}] \cdot \mathbf{F}^T \right\} \circ \phi^{-1} \\ &= \dot{\boldsymbol{\tau}} - (\mathbf{d} + \boldsymbol{\omega}) \cdot \boldsymbol{\tau} - \boldsymbol{\tau} \cdot (\mathbf{d} + \boldsymbol{\omega})^T, \end{aligned}$$

²⁾The algebraic and dynamic interpretations of the Lie derivative have been presented by ABRAHAM *et al.* [1], cf. also MARSDEN and HUGHES [29].

where \circ denotes the composition of mappings. In the coordinate system (3.13) reads

$$(3.14) \quad (\mathbf{L}_{\mathbf{v}}\boldsymbol{\tau})^{ab} = F_A^a \frac{\partial}{\partial t} \left(F_c^{-1A} \tau^{cd} F_d^{-1B} \right) F_B^b \\ = \frac{\partial \tau^{ab}}{\partial t} + \frac{\partial \tau^{ab}}{\partial x^c} v^c - \tau^{cb} \frac{\partial v^a}{\partial x^c} - \tau^{ac} \frac{\partial v^b}{\partial x^c}.$$

Equation (3.14) defines the Oldroyd rate of the Kirchhoff stress tensor $\boldsymbol{\tau}$ (cf. OLDROYD [33]).

3.2. Constitutive postulates

Let us assume that: (i) conservation of mass, (ii) balance of momentum, (iii) balance of moment of momentum, (iv) balance of energy, (v) entropy production inequality hold.

We introduce the four fundamental postulates:

- (i) Existence of the free energy function. It is assumed that the free energy function is given by

$$(3.15) \quad \psi = \hat{\psi}(\mathbf{e}, \mathbf{F}, \vartheta; \boldsymbol{\mu}),$$

where \mathbf{e} denotes the Eulerian strain tensor, \mathbf{F} is deformation gradient, ϑ temperature and $\boldsymbol{\mu}$ denotes a set of the internal state variables.

To extend the domain of the description of the material properties and particularly to take into consideration different dissipation effects we have to introduce the internal state variables represented by the vector $\boldsymbol{\mu}$.

- (ii) Axiom of objectivity (spatial covariance). The constitutive structure should be invariant with respect to any diffeomorphism (any motion) $\boldsymbol{\xi} : \mathcal{S} \rightarrow \mathcal{S}$ (cf. MARSDEN and HUGHES [29]). Assuming that $\boldsymbol{\xi} : \mathcal{S} \rightarrow \mathcal{S}$ is a regular, orientation preserving map transforming \mathbf{x} into \mathbf{x}' and $T\boldsymbol{\xi}$ is an isometry from $T_{\mathbf{x}}\mathcal{S}$ to $T_{\mathbf{x}'}\mathcal{S}$, we obtain the axiom of material frame indifference (cf. TRUESDELL and NOLL [54]).
- (iii) The axiom of the entropy production. For any regular motion of a body \mathcal{B} the constitutive functions are assumed to satisfy the reduced dissipation inequality

$$(3.16) \quad \frac{1}{\rho_{\text{Ref}}} \boldsymbol{\tau} : \mathbf{d} - (\eta \dot{\vartheta} + \dot{\psi}) - \frac{1}{\rho \vartheta} \mathbf{q} \cdot \text{grad} \vartheta \geq 0,$$

where ρ_{Ref} and ρ denote the mass density in the reference and actual configuration, respectively, $\boldsymbol{\tau}$ is the Kirchhoff stress tensor, \mathbf{d} the rate of deformation, η is the specific (per unit mass) entropy, and \mathbf{q} denotes the heat

flow vector field. MARSDEN and HUGHES [29] proved that the reduced dissipation inequality (3.16) is equivalent to the entropy production inequality first introduced by COLEMAN and NOLL [5] in the form of the Clausius–Duhem inequality. In fact the Clausius–Duhem inequality gives a statement of the second law of thermodynamics within the framework of mechanics of continuous media, cf. DUSZEK and PERZYNA [14], and PERZYNA [42].

- (iv) The evolution equation for the internal state variable vector $\boldsymbol{\mu}$ is assumed in the form as follows

$$(3.17) \quad L_v \boldsymbol{\mu} = \hat{\mathbf{m}}(\mathbf{e}, \mathbf{F}, \vartheta, \boldsymbol{\mu}),$$

where the evolution function $\hat{\mathbf{m}}$ has to be determined based on careful physical interpretation of a set of the internal state variables and analysis of available experimental observations.

The determination of the evolution function $\hat{\mathbf{m}}$ (in practice a finite set of the evolution functions) appears to be the main problem of the modern constitutive modelling.

The main objective is to develop the rate type constitutive structure for an elastic-viscoplastic material in which the effects of the plastic non-normality, micro-damaged mechanism and thermomechanical coupling are taken into consideration. To do this it is sufficient to assume a finite set of the internal state variables. For our practical purposes it is sufficient to assume that the internal state vector $\boldsymbol{\mu}$ has the form

$$(3.18) \quad \boldsymbol{\mu} = (\epsilon^p, \xi),$$

where ϵ^p is the equivalent viscoplastic deformation, i.e.

$$(3.19) \quad \epsilon^p = \int_0^t \left(\frac{2}{3} \mathbf{d}^p : \mathbf{d}^p \right)^{1/2} dt,$$

and ξ is volume fraction porosity and takes account for micro-damaged effects.

Let us introduce the plastic potential function $f = f(J_1, J_2, \vartheta, \boldsymbol{\mu})$, where J_1, J_2 denote the first two invariants of the Kirchhoff stress tensor $\boldsymbol{\tau}$.

Let us postulate the evolution equations as follows

$$(3.20) \quad \mathbf{d}^p = \Lambda \mathbf{P}, \quad \dot{\xi} = \Xi,$$

where for elasto-viscoplastic model of a material we assume (cf. PERZYNA [34–36, 41])

$$(3.21) \quad \Lambda = \frac{1}{T_m} \left\langle \Phi \left(\frac{f}{\kappa} - 1 \right) \right\rangle,$$

T_m denotes the relaxation time for mechanical disturbances, the isotropic work-hardening-softening function κ is

$$(3.22) \quad \kappa = \widehat{\kappa}(\epsilon^p, \vartheta, \xi),$$

Φ is the empirical overstress function, the bracket $\langle \cdot \rangle$ defines the ramp function,

$$(3.23) \quad \mathbf{P} = \frac{\partial f}{\partial \boldsymbol{\tau}} \bigg|_{\xi=\text{const}} \left(\left\| \frac{\partial f}{\partial \boldsymbol{\tau}} \right\| \right)^{-1},$$

Ξ denotes the evolution function which has to be determined.

3.3. Intrinsic micro-damage mechanisms

To take into consideration experimentally observed time dependent effects it is advantageous to use the proposition of the description of the intrinsic micro-damage process presented by PERZYNA [38, 39] and DUSZEK–PERZYNA and PERZYNA [15].

Let us assume that the intrinsic micro-damage process consists of the nucleation and growth mechanisms³⁾.

Physical considerations (cf. CURRAN *et al.* [7] and PERZYNA [38, 39]) have shown that the nucleation of microvoids in dynamic loading processes which are characterized by very short time duration is governed by the thermally-activated mechanism. Based on this heuristic suggestion and taking into account the influence of the stress triaxiality on the nucleation mechanism we postulate for rate dependent plastic flow⁴⁾

$$(3.24) \quad \left(\dot{\xi} \right)_{\text{nucl}} = \frac{1}{T_m} h^*(\xi, \vartheta) \left[\exp \frac{m^*(\vartheta) | I_n - \tau_n(\xi, \vartheta, \epsilon^p) |}{k\vartheta} - 1 \right],$$

where k denotes the Boltzmann constant, $h^*(\xi, \vartheta)$ represents a void nucleation material function which is introduced to take account of the effect of microvoid interaction, $m^*(\vartheta)$ is a temperature dependent coefficient, $\tau_n(\xi, \vartheta, \epsilon^p)$ is the porosity, temperature and equivalent plastic strain dependent threshold stress for microvoid nucleation,

$$(3.25) \quad I_n = a_1 J_1 + a_2 \sqrt{J_2'} + a_3 (J_3')^{1/3}$$

³⁾Experimental observation results (cf. SHOCKEY *et al.* [49]) have shown that coalescence mechanism can be treated as nucleation and growth process on a smaller scale. This conjecture simplifies very much the description of the intrinsic micro-damage process by taking account only of the nucleation and growth mechanisms.

⁴⁾An analysis of the experimental observations for cycle fatigue damage mechanics at high temperature of metals performed by SIDEY and COFFIN [50] suggests that the intrinsic micro-damage process does very much depend on the strain rate effects, the wave shape effects as well as on the stress triaxiality.

defines the stress intensity invariant for nucleation, a_i ($i = 1, 2, 3$) are the material constants, J_1 denotes the first invariant of the Kirchhoff stress tensor $\boldsymbol{\tau}$, J'_2 and J'_3 are the second and third invariants of the stress deviator $\boldsymbol{\tau}'$.

For the growth mechanism we postulate (cf. JOHNSON [26]; PERZYNA [38, 39]; PERZYNA and DRABIK [45] and DORNOWSKI and PERZYNA [10–12])

$$(3.26) \quad \left(\dot{\xi} \right)_{\text{grow}} = \frac{1}{T_m} \frac{g^*(\xi, \vartheta)}{\kappa_0} [I_g - \tau_{eq}(\xi, \vartheta, \epsilon^p)],$$

where $T_m \kappa_0$ denotes the dynamic viscosity of a material, $g^*(\xi, \vartheta)$ represents a void growth material function and takes account for void interaction, $\tau_{eq}(\xi, \vartheta, \epsilon^p)$ is the porosity, temperature and equivalent plastic strain dependent void growth threshold stress,

$$(3.27) \quad I_g = b_1 J_1 + b_2 \sqrt{J'_2} + b_3 (J'_3)^{1/3},$$

defines the stress intensity invariant for growth and b_i ($i = 1, 2, 3$) are the material constants.

Finally the evolution equation for the porosity ξ has the form

$$(3.28) \quad \dot{\xi} = \frac{h^*(\xi, \vartheta)}{T_m} \left[\exp \frac{m^*(\vartheta) |I_n - \tau_n(\xi, \vartheta, \epsilon^p)|}{k\vartheta} - 1 \right] + \frac{g^*(\xi, \vartheta)}{T_m \kappa_0} [I_g - \tau_{eq}(\xi, \vartheta, \epsilon^p)].$$

To have consistent theory of elasto-viscoplasticity we can replace the exponential function in the nucleation term and the linear function in the growth term by the empirical overstress Φ , then the evolution equation for the porosity ξ takes the form as follows (cf. PERZYNA [43])

$$(3.29) \quad \dot{\xi} = \frac{1}{T_m} h^*(\xi, \vartheta) \left\langle \Phi \left[\frac{I_n}{\tau_n(\xi, \vartheta, \epsilon^p)} - 1 \right] \right\rangle + \frac{1}{T_m} g^*(\xi, \vartheta) \left\langle \Phi \left[\frac{I_g}{\tau_{eq}(\xi, \vartheta, \epsilon^p)} - 1 \right] \right\rangle.$$

This determines the evolution function Ξ .

3.4. Thermodynamic restrictions and rate type constitutive equations

Suppose the axiom of the entropy production holds. Then the constitutive assumption (3.15) and the evolution equations (3.20) lead to the results as follows

$$(3.30) \quad \begin{aligned} \boldsymbol{\tau} &= \rho_{\text{Ref}} \frac{\partial \widehat{\psi}}{\partial \mathbf{e}}, & \eta &= -\frac{\partial \widehat{\psi}}{\partial \vartheta}, \\ -\frac{\partial \widehat{\psi}}{\partial \boldsymbol{\mu}} \cdot \mathbf{L}_{\mathbf{v}} \boldsymbol{\mu} - \frac{1}{\rho \vartheta} \mathbf{q} \cdot \text{grad } \vartheta &\geq 0. \end{aligned}$$

The rate of internal dissipation is determined by

$$(3.31) \quad \widehat{\vartheta i} = -\frac{\partial \widehat{\psi}}{\partial \boldsymbol{\mu}} \cdot \mathbf{L}_{\mathbf{v}} \boldsymbol{\mu} = -\left(\frac{\partial \widehat{\psi}}{\partial \epsilon^p} \sqrt{\frac{2}{3}} \right) \Lambda - \frac{\partial \widehat{\psi}}{\partial \xi} \Xi.$$

Operating on the stress relation (3.30)₁ with the Lie derivative and keeping the internal state vector constant, we obtain (cf. DUSZEK–PERZYNA and PERZYNA [15])

$$(3.32) \quad \mathbf{L}_{\mathbf{v}} \boldsymbol{\tau} = \mathcal{L}^e : \mathbf{d} - \mathcal{L}^{th} \dot{\vartheta} - [(\mathcal{L}^e + \mathbf{g} \boldsymbol{\tau} + \boldsymbol{\tau} \mathbf{g}) : \mathbf{P}] \frac{1}{T_m} \left\langle \Phi \left(\frac{f}{\kappa} - 1 \right) \right\rangle,$$

where

$$(3.33) \quad \mathcal{L}^e = \rho_{\text{Ref}} \frac{\partial^2 \widehat{\psi}}{\partial \mathbf{e}^2}, \quad \mathcal{L}^{th} = -\rho_{\text{Ref}} \frac{\partial^2 \widehat{\psi}}{\partial \mathbf{e} \partial \vartheta}.$$

Substituting $\dot{\psi}$ into the energy balance equation and taking into account the results (3.30)₃ and (3.31) gives

$$(3.34) \quad \rho \vartheta \dot{\eta} = -\text{div} \mathbf{q} + \rho \widehat{\vartheta i}.$$

Operating on the entropy relation (3.30)₂ with the Lie derivative and substituting the result into (3.34) we obtain

$$(3.35) \quad \rho c_p \dot{\vartheta} = -\text{div} \mathbf{q} + \vartheta \frac{\rho}{\rho_{\text{Ref}}} \frac{\partial \boldsymbol{\tau}}{\partial \vartheta} : \mathbf{d} + \rho \chi^* \boldsymbol{\tau} : \mathbf{d}^p + \rho \chi^{**} \dot{\xi},$$

where the specific heat

$$(3.36) \quad c_p = -\vartheta \frac{\partial^2 \widehat{\psi}}{\partial \vartheta^2}$$

and the irreversibility coefficients χ^* and χ^{**} are determined by

$$(3.37) \quad \begin{aligned} \chi^* &= -\left(\frac{\partial \widehat{\psi}}{\partial \epsilon^p} - \vartheta \frac{\partial^2 \widehat{\psi}}{\partial \vartheta \partial \epsilon^p} \right) \sqrt{\frac{2}{3}} \frac{1}{\boldsymbol{\tau} : \mathbf{P}}, \\ \chi^{**} &= -\left(\frac{\partial \widehat{\psi}}{\partial \xi} - \vartheta \frac{\partial^2 \widehat{\psi}}{\partial \vartheta \partial \xi} \right). \end{aligned}$$

So, a set of the constitutive equations of the rate type has the form as follows

$$\begin{aligned}
 \mathbf{L}_v \boldsymbol{\tau} &= \mathcal{L}^e : \mathbf{d} - \mathcal{L}^{th} \dot{\vartheta} - [(\mathcal{L}^e + \mathbf{g} \boldsymbol{\tau} + \boldsymbol{\tau} \mathbf{g}) : \mathbf{P}] \frac{1}{T_m} \left\langle \Phi \left(\frac{f}{\kappa} - 1 \right) \right\rangle, \\
 \rho c_p \dot{\vartheta} &= -\operatorname{div} \mathbf{q} + \vartheta \frac{\rho}{\rho_{\text{Ref}}} \frac{\partial \boldsymbol{\tau}}{\partial \vartheta} : \mathbf{d} + \rho \chi^* \frac{1}{T_m} \left\langle \Phi \left(\frac{f}{\kappa} - 1 \right) \right\rangle \boldsymbol{\tau} : \mathbf{P} + \rho \chi^{**} \dot{\xi}, \\
 \dot{\xi} &= \frac{1}{T_m} h^*(\xi, \vartheta) \left\langle \Phi \left[\frac{I_n}{\tau_n(\xi, \vartheta, \epsilon^p)} - 1 \right] \right\rangle \\
 &\quad + \frac{1}{T_m} g^*(\xi, \vartheta) \left\langle \Phi \left[\frac{I_g}{\tau_{eq}(\xi, \vartheta, \epsilon^p)} - 1 \right] \right\rangle.
 \end{aligned}
 \tag{3.38}$$

All the material functions and the material constants should be identified based on available experimental data.

3.5. Fracture criterion based on the evolution of micro-damage

We base the fracture criterion on the evolution of the porosity internal state variable ξ . The volume fraction porosity ξ takes account for microdamage effects.

Let us assume that for $\xi = \xi^F$ catastrophe takes place (cf. PERZYNA [37]), that is

$$\kappa = \widehat{\kappa}(\epsilon^p, \vartheta, \xi)|_{\xi=\xi^F} = 0.
 \tag{3.39}$$

It means that for $\xi = \xi^F$ the material loses its carrying capacity. The condition (3.39) describes the main feature observed experimentally that the load tends to zero at the fracture point.

It is noteworthy that the isotropic hardening–softening material function $\widehat{\kappa}$ proposed in Eq. (3.22) should satisfy the fracture criterion (3.39).

3.6. Length-scale sensitivity of the constitutive model

The constitutive equations for a thermo-elastic-viscoplastic model introduce implicitly a length-scale parameter into the dynamic initial-boundary value problem, i.e.

$$l = \alpha c T_m,
 \tag{3.40}$$

where T_m is the relaxation time for mechanical disturbances, and is directly related to the viscosity of the material, c denotes the velocity of the propagation of the elastic waves in the problem under consideration, and the proportionality factor α depends on the particular initial-boundary value problem and may also be conditioned on the microscopic properties of the material.

The relaxation time T_m can be viewed either as a microstructural parameter to be determined from experimental observations or as a mathematical regularization parameter.

4. DISCUSSION OF THE EVOLUTION PROBLEM

4.1. Initial-boundary value problem (evolution problem)

Find $\boldsymbol{\varphi}$ as function of t and \mathbf{x} satisfying

$$(4.1) \quad \begin{cases} \text{(i)} & \dot{\boldsymbol{\varphi}} = \mathcal{A}(t, \boldsymbol{\varphi})\boldsymbol{\varphi} + \mathbf{f}(t, \boldsymbol{\varphi}); \\ \text{(ii)} & \boldsymbol{\varphi}(0) = \boldsymbol{\varphi}^0(\mathbf{x}); \\ \text{(iii)} & \text{The boundary conditions;} \end{cases}$$

where the unknown $\boldsymbol{\varphi}$ takes values in a Banach space, $\mathcal{A}(t, \boldsymbol{\varphi})$ is a spatial linear differential operator (in general unbounded) depending on t and $\boldsymbol{\varphi}$, \mathbf{f} is a nonlinear function, and the dot denotes the material derivative.

The evolution problem (4.1) describes an adiabatic inelastic flow process provided

$$(4.2) \quad \begin{aligned} \boldsymbol{\varphi} &= \begin{bmatrix} \mathbf{v} \\ \rho \\ \boldsymbol{\tau} \\ \xi \\ \vartheta \end{bmatrix}, \\ \mathbf{f} &= \begin{bmatrix} 0 \\ 0 \\ -\frac{\left\langle \Phi\left(\frac{f}{\kappa} - 1\right) \right\rangle}{T_m} \left[\left(\mathcal{L}^e + \frac{\chi^* \boldsymbol{\tau}}{\rho_{\text{Ref}}} \mathcal{L}^{th} + \mathbf{g}\boldsymbol{\tau} + \boldsymbol{\tau}\mathbf{g} \right) : \mathbf{P} \right] - \frac{\chi^{**}\Xi}{\rho_{\text{Ref}}} \mathcal{L}^{th} \\ \frac{1}{T_m} \left\langle \Phi\left(\frac{f}{\kappa} - 1\right) \right\rangle \frac{\Xi}{\rho_{\text{Ref}}} \mathcal{L}^{th} \boldsymbol{\tau} : \mathbf{P} + \frac{\chi^{**}}{\rho_{\text{Ref}}} \Xi \end{bmatrix}, \\ \mathcal{A} &= \begin{bmatrix} 0 & 0 & \frac{\boldsymbol{\tau}}{\rho_{\text{Ref}}\rho} \text{grad} & \frac{1}{\rho_{\text{Ref}}} \text{div} & 0 \\ 0 & -\rho \text{div} & 0 & 0 & 0 \\ 0 & \mathbb{E} : \text{sym} \frac{\partial}{\partial \mathbf{x}} + 2 \text{sym} \left(\boldsymbol{\tau} : \frac{\partial}{\partial \mathbf{x}} \right) & 0 & 0 & 0 \\ 0 & 0 & 0 & 0 & 0 \\ 0 & \frac{\vartheta}{c_p \rho_{\text{Ref}}} \frac{\partial \boldsymbol{\tau}}{\partial \vartheta} : \text{sym} \frac{\partial}{\partial \mathbf{x}} & 0 & 0 & 0 \end{bmatrix}. \end{aligned}$$

where

$$(4.3) \quad \mathbb{E} = \mathcal{L}^e - \frac{\vartheta}{c_p \rho_{\text{Ref}}} \mathcal{L}^{th} \frac{\partial \tau}{\partial \vartheta}$$

denotes the thermo-elastodynamic matrix for adiabatic process.

It is noteworthy that the spatial operator \mathcal{A} has the same form as in thermo-elastodynamics while all dissipative effects generated by viscoplastic flow phenomena and by microdamage mechanisms influence the adiabatic impact loading process through the nonlinear function \mathbf{f} .

A strict solution of (4.1) with $\mathbf{f}(t, \boldsymbol{\varphi}) \equiv 0$ (i.e. the homogeneous evolution problem) is defined as a function $\boldsymbol{\varphi}(t) \in \mathbf{E}$ (a Banach space) such that⁵⁾

$$(4.4) \quad \begin{aligned} & \boldsymbol{\varphi}(t) \in \mathcal{D}(\mathcal{A}), & \text{for all } t \in [0, t_f], \\ & \lim_{\Delta t \rightarrow 0} \left\| \frac{\boldsymbol{\varphi}(t + \Delta t) - \boldsymbol{\varphi}(t)}{\Delta t} - \mathcal{A}\boldsymbol{\varphi}(t) \right\|_{\mathbf{E}} = 0 & \text{for all } t \in [0, t_f]. \end{aligned}$$

The boundary conditions are taken care of by restricting the domain $\mathcal{D}(\mathcal{A})$ to elements of \mathbf{E} that satisfy those conditions; they are assumed to be linear and homogeneous, so that the set \mathbf{S} of all $\boldsymbol{\varphi}$ that satisfy them is a linear manifold; $\mathcal{D}(\mathcal{A})$ is assumed to be contained in \mathbf{S} .

The choice of the Banach space \mathbf{E} , as well as the domain of \mathcal{A} , is an essential part of the formulation of the evolution problem.

4.2. Well-posedness of the evolution problem

The homogeneous evolution problem (i.e. for $\mathbf{f} \equiv 0$) is called well posed (in the sense of Hadamard) if it has the following properties:

- (i) The strict solutions are uniquely determined by their initial elements;
- (ii) The set Y of all initial elements of strict solutions is dense in the Banach space \mathbf{E} ;
- (iii) For any finite interval $[0, t_0]$, $t_0 \in [0, t_f]$ there is a constant $K = K(t_0)$ such that every strict solution satisfies the inequality

$$(4.5) \quad \|\boldsymbol{\varphi}(t)\| \leq K \|\boldsymbol{\varphi}^0\| \quad \text{for } 0 \leq t \leq t_0.$$

The inhomogeneous evolution problem (4.1) will be called well posed if it has a unique solution for all reasonable choices of $\boldsymbol{\varphi}^0$ and $\mathbf{f}(t, \boldsymbol{\varphi})$ and if the solution depends continuously, in some sense, on those choices.

⁵⁾We shall follow here some fundamental results which have been discussed in RICHTMYER and MORTON [47], STRANG and FIX [52], RICHTMYER [46] and DAUTRAY and LIONS [8].

It is evident that any solution is unique, because of the uniqueness of the solutions of the homogeneous evolution problem. Namely, the difference of two solutions, for given $\boldsymbol{\varphi}^0$ and given $\mathbf{f}(\cdot)$, is a solution of the homogeneous problem with zero as initial element, hence must be zero for all t .

It is possible to show (cf. RICHTMYER [46]) that strict solutions exist for sets of $\boldsymbol{\varphi}^0$ and $\mathbf{f}(\cdot)$ that are dense in E and E_1 (a new Banach space), respectively.

Let $\{\mathbb{F}_t^*; t \geq 0\}$ be a semi-group generated by the operator $\mathcal{A} + \mathbf{f}(\cdot)$ (as it has been defined in Section 4.1) and $\{\mathbb{F}_t; t \geq 0\}$ be a semi-group generated by the operator \mathcal{A} .

Then we can write the generalized solution of the nonhomogenous evolution problem (4.1) in alternative forms

$$\begin{aligned} \boldsymbol{\varphi}(t, \mathbf{x}) &= \mathbb{F}^*(t) \boldsymbol{\varphi}^0(\mathbf{x}) \\ (4.6) \qquad &= \mathbb{F}(t) \boldsymbol{\varphi}^0(\mathbf{x}) + \int_0^t \mathbb{F}(t-s) \mathbf{f}(s, \boldsymbol{\varphi}(s)) ds. \end{aligned}$$

The generalized solution of the nonhomogenous evolution problem (4.1) in the form (4.6)₂ is the integral equation.

The successive approximations for (4.6)₂ are defined to be the functions $\boldsymbol{\varphi}_0, \boldsymbol{\varphi}_1, \dots$, given by the formulas

$$\begin{aligned} \boldsymbol{\varphi}_0(t) &= \boldsymbol{\varphi}^0, \\ &\dots\dots\dots \\ (4.7) \qquad \boldsymbol{\varphi}_{k+1}(t) &= \mathbb{F}(t) \boldsymbol{\varphi}^0 + \int_0^t \mathbb{F}(t-s) \mathbf{f}(s, \boldsymbol{\varphi}_k(s)) ds, \\ k &= 0, 1, 2, \dots; \quad t \in [0, t_f]. \end{aligned}$$

It is possible to show that these functions actually exist on $t \in [0, t_f]$ if the continuous function \mathbf{f} is Lipschitz continuous with respect to the second argument uniformly with respect to $t \in [0, t_f]$, cf. PERZYNA [40]. Then (4.6)₂ has unique solution (cf. also IONESCU and SOFONEA [25]).

4.3. Discretization in space and time

We must approximate (4.1) twice. First, when E is infinite dimensional, we must replace \mathcal{A} by an operator \mathcal{A}_h which operates in a finite dimensional space $V_h \subset E$, where, in general, $h > 0$ represents a discretisation step in space, such that $\dim(V_h) \rightarrow \infty$ as $h \rightarrow 0$. Second, we must discretise in time, that is to say choose a sequence of moments t_n (for example $t_n = n\Delta t$, where Δt is time step) at which we shall calculate the approximate solution.

Let us introduce the following semi-discretised (discrete in space) problem.

$$(4.8) \quad \begin{cases} \text{Find } \boldsymbol{\varphi}_h \in \mathcal{C}^0([0, t_0]; V_h) \text{ (}\mathcal{C}^0 \text{ denotes the space of functions} \\ \text{continuous on } ([0, t_0], V_h)) \text{ satisfying} \\ \frac{d\boldsymbol{\varphi}_h(t)}{dt} = \mathcal{A}_h \boldsymbol{\varphi}_h(t) + \mathbf{f}_h(t), \\ \boldsymbol{\varphi}_h(0) = \boldsymbol{\varphi}_{0,h}. \end{cases}$$

The operator \mathcal{A}_h for the finite element method can be obtained by a variational formulation approach. The discrete equations are obtained by the Galerkin method at particular points in the domain.

Finally, we shall define a method allowing us to calculate $\boldsymbol{\varphi}_h^n \in V_h$, an approximation to $\boldsymbol{\varphi}_h(t_n)$ starting from $\boldsymbol{\varphi}_h^{n-1}$ (we limit ourselves to a two-level scheme). Then we can write

$$(4.9) \quad \boldsymbol{\varphi}_h^{n+1} = C_h(\Delta t) \boldsymbol{\varphi}_h^n + \Delta t \mathbf{f}_h^n, \quad \boldsymbol{\varphi}_h^0 = \boldsymbol{\varphi}_{0,h},$$

where we introduce the operator $C_h(\Delta t) \in \mathcal{L}(V_h)$ (\mathcal{L} is the set of continuous linear mapping of V_h with values in V_h) and where \mathbf{f}_h^n approximates $\mathbf{f}_h(t_n)$.

We shall always assume that the evolution problem (4.1) is well posed and there exists a projection R_h of E into V_h such that

$$(4.10) \quad \lim_{h \rightarrow 0} |R_h \boldsymbol{\varphi} - \boldsymbol{\varphi}|_E = 0, \quad \forall \boldsymbol{\varphi} \in E.$$

4.4. Convergence, consistency and stability

The first fundamental question is that of the convergence, when h and Δt tend to zero, of the sequence $\{\boldsymbol{\varphi}_h^n\}$, the solution (4.9), towards the function $\boldsymbol{\varphi}(t)$, the solution of (4.1). Let us restrict our consideration, for the moment, to the case where $\mathbf{f}(t) \equiv 0$.

DEFINITION 1: *The scheme defined by (4.9) will be called convergent if the condition*

$$(4.11) \quad \boldsymbol{\varphi}_{0,h} \rightarrow \boldsymbol{\varphi}^0 \quad \text{as } h \rightarrow 0$$

implies that

$$(4.12) \quad \boldsymbol{\varphi}_h^n \rightarrow \boldsymbol{\varphi}(t) \quad \text{as } \Delta t \rightarrow 0, \quad n \rightarrow \infty \quad \text{with } n\Delta t \rightarrow t$$

for all $t \in]0, t_0[$, $t_0 \in [0, t_f]$, where $\boldsymbol{\varphi}_h^n$ is defined by (4.9) and $\boldsymbol{\varphi}(t)$ is the solution of (4.1). All this holds for arbitrary $\boldsymbol{\varphi}^0$.

The study of the convergence of an approximation scheme involves two fundamental properties of the scheme, consistency and stability.

DEFINITION 2: *The scheme defined by (4.9) is called stable, if there exists a constant $K \geq 1$ independent of h and Δt such that*

$$(4.13) \quad \|(C_h(\Delta t))^n R_h\|_{\mathcal{L}(\mathbf{E})} \leq K \quad \forall n, \Delta t \text{ satisfying } n\Delta t \leq t_0.$$

In the Definition 1 and 2 there occur two parameters h and Δt . It may be that the scheme is not stable (or not convergent) unless Δt and h satisfy supplementary hypotheses of the type $\Delta t/h^\alpha \leq \text{constant}$, $\alpha < 0$, in which case we call the scheme **conditionally stable**. If the scheme is stable for arbitrary h and Δt we say that it is **unconditionally stable**.

These schemes reflect so called explicit and implicit types of the integration procedure in a particular numerical implementation.

DEFINITION 3: *The scheme defined by (4.9) will be called consistent with equation (4.1) if there exists a subspace $Y \subset \mathbf{E}$ dense in \mathbf{E} , such that for every $\boldsymbol{\varphi}(t)$ which is a solution of (4.1) with $\boldsymbol{\varphi}^0 \subset Y$ (and $\mathbf{f} \equiv 0$) we have*

$$(4.14) \quad \lim_{h \rightarrow 0, \Delta t \rightarrow 0} \left| \frac{C_h(\Delta t) R_h \boldsymbol{\varphi}(t) - \boldsymbol{\varphi}(t)}{\Delta t} - \mathcal{A} \boldsymbol{\varphi}(t) \right|_{\mathbf{E}} = 0.$$

We see that the two essential preoccupations in the study of approximation schemes for the solution of evolution equations are on the one hand the determination of the consistency of the scheme, more precisely the order of precision and on the other hand its stability.

Determining the order of precision is, in general, easy, we shall therefore study the stability of the scheme in more detail.

4.5. The Lax-Richtmyer equivalence theorem

We can now state the Lax-Richtmyer equivalence theorem (cf. RICHTMYER and MORTON [47], STRANG and FIX [52], DAUTRAY and LIONS [8] and GUSTAFSSON, KREISS and OLIGER [23]).

THEOREM 1: *Suppose that the evolution problem (4.1) is well-posed for $t \in [0, t_0]$ and that it is approximated by the scheme (4.9), which we assume consistent. Then the scheme is convergent if and only if it is stable.*

The proof of the Lax-Richtmyer equivalence theorem for the case when the partial differential operator \mathcal{A} in (4.2) is independent of $\boldsymbol{\varphi}$ can be found in DAUTRAY and LIONS [8].

REMARK. Let us consider the evolution problem (4.1) with

$$(4.15) \quad \mathbf{f}(t, \boldsymbol{\varphi}) \neq 0$$

and $\boldsymbol{\varphi}^0 = 0$, and also the corresponding approximation (4.9). We have

$$(4.16) \quad \boldsymbol{\varphi}_h^{n+1} = \Delta t \sum_{j=1}^n [C_h(\Delta t)]^{n-j} \mathbf{f}_h^j.$$

If \mathcal{A} is the infinitesimal generator of a semigroup $\{\mathbb{F}(t)\}$ we can write

$$(4.17) \quad \boldsymbol{\varphi}(t) = \int_0^t \mathbb{F}(t-s) \mathbf{f}(s) ds.$$

Under suitable hypotheses on the convergence of \mathbf{f}_h^j to $\mathbf{f}(j\Delta t)$ we can show that expression (4.16) converges to (4.17) if the scheme is stable and consistent.

4.6. Dispersive analysis

The most important feature is that the propagation of deformation waves in an elastic-viscoplastic medium has dispersive nature.

The dispersion of a waveform is caused by certain physical and/or geometrical characteristics of the medium in which the wave is generated. Consequently, instead of dispersive waves, it is perhaps more precise to speak of a **dispersive medium** or, where geometrical features alone cause the dispersion, a **dispersive geometry**, cf. THAU [53].

To make our analysis easier let us consider the linear case of the evolution equation with the interpretation of the functions $\boldsymbol{\varphi}$ and \mathbf{f} as well as the spatial differential operator \mathcal{A} given by (4.1) and (4.2) i.e.

$$(4.18) \quad \dot{\boldsymbol{\varphi}} = \mathcal{A}_0(t, \mathbf{x}) \boldsymbol{\varphi} + f_0(t, \mathbf{x}) \boldsymbol{\varphi}.$$

The theory of dispersive wave propagation can be introduced by a particular wave solution of (4.18), namely, by the simple harmonic wavetrains (cf. WHITHAM [55, 56] and THAU [53])

$$(4.19) \quad \boldsymbol{\varphi} = A \exp[i(\mathbf{k} \cdot \mathbf{x} - \omega t)],$$

where \mathbf{k} is the wave number, ω is the frequency, and A denotes the amplitude.

Since a set of the equations (4.18) is linear, A factor out and can be arbitrary. To satisfy a set of the equations (4.18), \mathbf{k} and ω have to be related by an equation

$$(4.20) \quad G(\omega, \mathbf{k}, \mathbf{x}, t) = 0,$$

which is called the dispersion relation.

Let us assume that the dispersion relation may be solved in the form of real roots

$$(4.21) \quad \omega = W(\mathbf{k}, \mathbf{x}, t).$$

There will be a number of such solutions, in general, with different functions $W(\mathbf{k}, \mathbf{x}, t)$. We refer to these as different modes.

The phase velocity \mathbf{c} is given as a function of wavenumber

$$(4.22) \quad \mathbf{c}(\mathbf{k}, \mathbf{x}, t) = \frac{\omega}{k} \hat{\mathbf{k}} = k^{-1} W(\mathbf{k}, \mathbf{x}, t) \hat{\mathbf{k}},$$

where $\hat{\mathbf{k}}$ is the unit vector in the \mathbf{k} direction. For any particular mode $\omega = W(\mathbf{k}, \mathbf{x}, t)$, the phase velocity \mathbf{c} is a function of \mathbf{k} .

Another velocity associated with the harmonic wavetrains (4.19) in dispersive media is the group velocity \mathbf{C} defines as

$$(4.23) \quad \mathbf{C}(\mathbf{k}, \mathbf{x}, t) = \frac{\partial W(\mathbf{k}, \mathbf{x}, t)}{\partial \mathbf{k}},$$

which also depends on the wavenumber \mathbf{k} .

The derivative of \mathbf{C} with respect to \mathbf{k} is the symmetric dispersive tensor

$$(4.24) \quad W_{\mathbf{k}\mathbf{k}} = \frac{\partial^2 W}{\partial \mathbf{k}^2}.$$

To have dispersive wave we have to introduce two assertions:

$$(4.25) \quad \begin{aligned} (i) \quad & W(\mathbf{k}, \mathbf{x}, t) \text{ is real;} \\ (ii) \quad & \det \left| \frac{\partial^2 W}{\partial k_i \partial k_j} \right| \neq 0. \end{aligned}$$

The group velocity \mathbf{C} is having a great effect and the condition (4.25)₂ ensures that it is not a constant.

The quantity

$$(4.26) \quad \Theta = \mathbf{k} \cdot \mathbf{x} - \omega t$$

in the solution (4.19) is the phase. The group velocity is actually the most important velocity associated with dispersive waves, as it not only is the velocity of a given group of oscillations or “wavelets” in a wavetrain but also coincides with the velocity with which the energy in that group propagates. Moreover, in a dispersive medium any initial disturbance is eventually broken up into a system of such groups, cf. THAU [53].

Since the medium under consideration has also dissipation property (cf. Eq. (4.1) in which the last term on the right hand side is responsible for dissipation effect) hence mathematically, losses due to dissipation are manifested by the dispersion relation yielding complex or pure imaginary values of W corresponding to real values of \mathbf{k} . The amplitude of a harmonic wavetrain then decays exponentially with time.

If the dissipation becomes appreciable, as is in the elastic-viscoplastic medium, then the general theory of waves in dispersive media would require modification.

The previous consideration does not apply to general nonlinear case (cf. Eq. (4.1)). To obtain some results we can use the variational method, the perturbation theory or the numerical method, cf. SLUYS [51].

Dispersion is a relation between the frequency and wave number, cf. WHITHAM [55]. The ratio of the frequency and wave number is the phase speed whereas the derivative of the frequency with respect to the wave number is the group speed. For nondispersive problem, both speeds are equal and on the other hand for dispersive one the group velocity depends on the frequency and in general is different from the phase speed. As a matter of fact, the dispersion of a waveform is caused by both material (physical law) and geometrical (boundaries) characteristics of the medium (specimen) in which the wave is generated.

4.7. Application of finite difference method

Let us consider the evolution problem in the form of (4.1). Let us introduce in the Euclidean space E^3 a regular difference net of nodes (i, j, k) with convective coordinates $\chi_i^1 = i\Delta\chi^1$, $\chi_j^2 = j\Delta\chi^2$ and $\chi_k^3 = k\Delta\chi^3$, $i, j, k \in N$, where N is a set of natural numbers, cf. DORNOWSKI [10] and DORNOWSKI and PERZYNA [11]. Of course, some of the nodes belong to the edge of the body and are used to approximate the boundary conditions. Time is approximated by a discrete sequence of moments $t_n = n\Delta t$, where Δt is time step, $n \in N$.

For all functions $\boldsymbol{\varphi} = \widehat{\boldsymbol{\varphi}}(\mathbf{x}, t)$ of the analysed problem we postulate the following approximation in the domain $\Delta E = \Delta\chi^1 \times \Delta\chi^2 \times \Delta\chi^3$ of a convective difference mesh (cf. Fig. 9):

$$(4.27) \quad \boldsymbol{\varphi}(\mathbf{x}, t) \cong \boldsymbol{\varphi}_h(\mathbf{x}, t) = \mathbf{a}_1(t) + \mathbf{a}_2(t)\chi^1 + \mathbf{a}_3(t)\chi^2 + \mathbf{a}_4(t)\chi^3 \\ + \mathbf{a}_5(t)\chi^1\chi^2 + \mathbf{a}_6(t)\chi^1\chi^3 + \mathbf{a}_7(t)\chi^2\chi^3 + \mathbf{a}_8(t)\chi^1\chi^2\chi^3,$$

$$\mathbf{x} \in \Delta\mathcal{S}.$$

The functions $\mathbf{a}_1(t), \dots, \mathbf{a}_8(t)$ depend only on time, are determined by the value of the function $\boldsymbol{\varphi}_w(t) = [\boldsymbol{\varphi}_1(t), \dots, \boldsymbol{\varphi}_8(t)]^T$ in the node points of difference

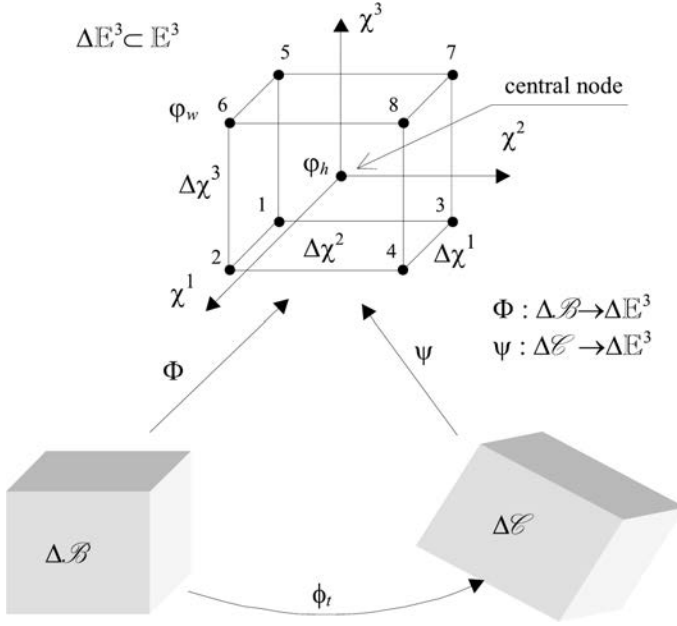


FIG. 9. Convective finite difference mesh of nodes.

mesh, (cf. Fig. 9). Hence the approximation functions (4.27) can be written in the form

$$(4.28) \quad \boldsymbol{\varphi}_h(\mathbf{x}, t) = \mathbf{N}(\mathbf{x}) \boldsymbol{\varphi}_w(t), \quad \mathbf{x} \in \Delta\mathcal{S},$$

where

$$(4.29) \quad \begin{aligned} N_1(\mathbf{x}) &= q(-\Delta\chi^1 + 2\chi^1)(-\Delta\chi^2 + 2\chi^2)(\Delta\chi^3 - 2\chi^3), \\ N_2(\mathbf{x}) &= q(\Delta\chi^1 + 2\chi^1)(-\Delta\chi^2 + 2\chi^2)(-\Delta\chi^3 + 2\chi^3), \\ N_3(\mathbf{x}) &= q(-\Delta\chi^1 + 2\chi^1)(\Delta\chi^2 + 2\chi^2)(-\Delta\chi^3 + 2\chi^3), \\ N_4(\mathbf{x}) &= q(\Delta\chi^1 + 2\chi^1)(\Delta\chi^2 + 2\chi^2)(\Delta\chi^3 - 2\chi^3), \\ N_5(\mathbf{x}) &= q(-\Delta\chi^1 + 2\chi^1)(-\Delta\chi^2 + 2\chi^2)(\Delta\chi^3 + 2\chi^3), \\ N_6(\mathbf{x}) &= q(\Delta\chi^1 + 2\chi^1)(\Delta\chi^2 - 2\chi^2)(\Delta\chi^3 + 2\chi^3), \\ N_7(\mathbf{x}) &= q(\Delta\chi^1 - 2\chi^1)(\Delta\chi^2 + 2\chi^2)(\Delta\chi^3 + 2\chi^3), \\ N_8(\mathbf{x}) &= q(\Delta\chi^1 + 2\chi^1)(\Delta\chi^2 + 2\chi^2)(\Delta\chi^3 + 2\chi^3), \\ q &= \frac{1}{8\Delta\chi^1\Delta\chi^2\Delta\chi^3} \end{aligned}$$

Equations (4.28) allow to determine values of the function $\boldsymbol{\varphi}_h(\mathbf{x}, t)$ in any point of the difference mesh, $\mathbf{x} \in \Delta\mathcal{S}$. For the central point $\mathbf{x} = \mathbf{x}_0$, $N_1 = \dots = N_8 = \frac{1}{8}$ and $\boldsymbol{\varphi}_h(t) = [\boldsymbol{\varphi}_1(t) + \dots + \boldsymbol{\varphi}_8(t)]\frac{1}{8}$.

By using (4.28) we can determine the matrix of the difference operators which approximate the first partial derivatives of the function $\boldsymbol{\varphi}(\mathbf{x}, t)$ for $\mathbf{x} \in \Delta\mathcal{S}$,

$$(4.30) \quad \frac{\partial}{\partial \mathbf{x}} \boldsymbol{\varphi}(\mathbf{x}, t) \cong \frac{\partial}{\partial \mathbf{x}} \boldsymbol{\varphi}_h(\mathbf{x}, t) = \frac{\partial}{\partial \mathbf{x}} \mathbf{N}(\mathbf{x}) \boldsymbol{\varphi}_w(t) = \mathbf{R}(\mathbf{x}) \boldsymbol{\varphi}_w(t).$$

The matrix of the difference operator $\mathbf{R}(\mathbf{x})$ for the central point takes the form

$$(4.31) \quad \mathbf{R}(\mathbf{x} = \mathbf{x}_0) = \left. \frac{\partial}{\partial \mathbf{x}} \mathbf{N}(\mathbf{x}) \right|_{\mathbf{x}=\mathbf{x}_0} = \begin{bmatrix} \frac{-1}{\Delta\chi^1} & \frac{1}{\Delta\chi^1} & \frac{-1}{\Delta\chi^1} & \frac{1}{\Delta\chi^1} & \frac{-1}{\Delta\chi^1} & \frac{1}{\Delta\chi^1} & \frac{-1}{\Delta\chi^1} & \frac{1}{\Delta\chi^1} \\ \frac{-1}{\Delta\chi^2} & \frac{-1}{\Delta\chi^2} & \frac{1}{\Delta\chi^2} & \frac{1}{\Delta\chi^2} & \frac{-1}{\Delta\chi^2} & \frac{-1}{\Delta\chi^2} & \frac{1}{\Delta\chi^2} & \frac{1}{\Delta\chi^2} \\ \frac{-1}{\Delta\chi^3} & \frac{-1}{\Delta\chi^3} & \frac{-1}{\Delta\chi^3} & \frac{-1}{\Delta\chi^3} & \frac{1}{\Delta\chi^3} & \frac{1}{\Delta\chi^3} & \frac{1}{\Delta\chi^3} & \frac{1}{\Delta\chi^3} \end{bmatrix}.$$

In similar way we can find the difference form of the spatial difference operator $\mathcal{A}(t, \boldsymbol{\varphi})$ of the considered evolution problem (4.1)

$$(4.32) \quad \mathcal{A}(t, \boldsymbol{\varphi}) \boldsymbol{\varphi} \cong \mathcal{A}(t, \boldsymbol{\varphi}_h) \mathbf{N}(\mathbf{x}) \boldsymbol{\varphi}_w(t) = \mathcal{A}_h(t, \boldsymbol{\varphi}_h) \boldsymbol{\varphi}_w(t),$$

hence

$$(4.33) \quad \mathcal{A}_h(t, \boldsymbol{\varphi}_h) = \mathcal{A}(t, \boldsymbol{\varphi}_h) \mathbf{N}(\mathbf{x}) \quad \text{for} \quad \mathbf{x} \in \Delta\mathcal{S}.$$

For the central node, $\mathbf{x} = \mathbf{x}_0$ the difference operator (4.33) depends only on time.

As a result of the proposed approximation of the evolution problem (4.1) with respect to the spatial variables we obtain a set of differential equations with respect to time and difference equations with respect to spatial variables

$$(4.34) \quad \frac{d\boldsymbol{\varphi}_h(t)}{dt} = \mathcal{A}_h \boldsymbol{\varphi}_w(t) + \mathbf{f}_h(t).$$

For the approximation of (4.34) with respect to time we use the evident scheme of the first order in the form

$$(4.35) \quad \frac{d\boldsymbol{\varphi}_h(t)}{dt} \cong \frac{\boldsymbol{\varphi}_h^{n+1} - \boldsymbol{\varphi}_h^n}{\Delta t} = \mathcal{A}_h \boldsymbol{\varphi}_w^n + \mathbf{f}_h^n.$$

The solution of (4.35) is reduced to the realization of the recurrence relation

$$(4.36) \quad \boldsymbol{\varphi}_h^{n+1} = \mathbf{C}_h(\Delta t) \boldsymbol{\varphi}_w^n + \Delta t \mathbf{f}_h^n.$$

The difference operator

$$(4.37) \quad \mathbf{C}_h(\Delta t) = \Delta t \mathcal{A}_h + \mathbf{N}$$

couple dependent variables and various points of difference mesh.

For the finite difference approximation it can be proved that the introduced scheme (4.36) is consistent with equation (4.1).

4.8. Stability criterion

In explicit finite difference scheme for a set of the partial differential equations (4.1)₁ of the hiperbolic type the condition of stability is assumed as the criterion of Courant–Friedrichs–Lewy, cf. COURANT *et al.* [6]

$$(4.38) \quad \Delta t_{n,n+1} \leq \min \left(\frac{\Delta L_{p,q,r}^n}{|c_{p,q,r}^n|} \right),$$

$$p = 1, 2, 3, \dots, P; \quad q = 1, 2, 3, \dots, Q; \quad r = 1, 2, 3, \dots, R,$$

where $\Delta t_{n,n+1}$ denotes time step, $c_{p,q,r}^n$ denotes the velocity of the propagation of the disturbances in the vicinity of the central node (p, q, r) , $\Delta L_{p,q,r}^n$ is the minimum distance between the mesh nodes which are in the vicinity of the node (cf. Fig. 9).

The Courant–Friedrichs–Lewy condition requires that the numerical domain of dependence of a finite-difference scheme include the domain of dependence of the associated partial differential equations, cf. DURRAN [16].

We can now use the Lax–Richtmyer equivalence theorem (cf. Theorem 1 in Subsec. 4.5).

5. IDENTIFICATION PROCEDURE

5.1. Assumption of the material functions for an adiabatic process

To do the proper identification procedure we first make assumption of the material functions (cf. DORNOWSKI and PERZYNA [11]).

The plastic potential function f is assumed in the form (cf. PERZYNA [37] and SHIMA and OYANE [48])

$$(5.1) \quad f = \left\{ J_2' + [n_1(\vartheta) + n_2(\vartheta)\xi] J_1^2 \right\}^{1/2}$$

where

$$(5.2) \quad \begin{aligned} n_1(\vartheta) &= 0, \\ n_2(\vartheta) &= n = \text{const.} \end{aligned}$$

The isotropic work-hardening-softening function κ is postulated as (cf. PERZYNA [38] and NEMES and EFTIS [32])

$$(5.3) \quad \begin{aligned} \kappa &= \widehat{\kappa}(\epsilon^p, \vartheta, \xi) \\ &= \{\kappa_s(\vartheta) - [\kappa_s(\vartheta) - \kappa_0(\vartheta)] \exp[-\delta(\vartheta)\epsilon^p]\} \left[1 - \left(\frac{\xi}{\xi_F} \right)^{\beta(\vartheta)} \right], \end{aligned}$$

where

$$(5.4) \quad \begin{aligned} \kappa_s(\vartheta) &= \kappa_s^*(1 - \bar{\iota}\bar{\vartheta}), & \kappa_0(\vartheta) &= \kappa_0^*(1 - \bar{\iota}\bar{\vartheta}), \\ \delta(\vartheta) &= \delta^*(1 - \bar{\iota}\bar{\vartheta}), & \beta(\vartheta) &= \beta^*(1 - \bar{\iota}\bar{\vartheta}), & \bar{\vartheta} &= \frac{\vartheta - \vartheta_0}{\vartheta_0}. \end{aligned}$$

The overstress function $\Phi\left(\frac{f}{\kappa} - 1\right)$ is assumed in the form

$$(5.5) \quad \Phi\left(\frac{f}{\kappa} - 1\right) = \left(\frac{f}{\kappa} - 1\right)^m.$$

The evolution equation for the porosity ξ is postulated as

$$(5.6) \quad \dot{\xi} = \dot{\xi}_{\text{grow}} = \frac{g^*(\xi, \vartheta)}{T_m \kappa_0(\vartheta)} [I_g - \tau_{eq}(\xi, \vartheta, \epsilon^p)]$$

where (cf. DORNOWSKI [9])

$$(5.7) \quad \begin{aligned} g^*(\xi, \vartheta) &= c_1(\vartheta) \frac{\xi}{1 - \xi}, \\ I_g &= b_1 J_1 + b_2 \sqrt{J_2}, \\ \tau_{eq}(\xi, \vartheta, \epsilon^p) &= c_2(\vartheta)(1 - \xi) \ln \frac{1}{\xi} \{2\kappa_s(\vartheta) - [\kappa_s(\vartheta) - \kappa_0(\vartheta)] F(\xi_0, \xi, \vartheta)\}, \\ c_1(\vartheta) &= \text{const}, & c_2(\vartheta) &= \text{const}, \end{aligned}$$

$$F(\xi_0, \xi, \vartheta) = \left(\frac{\xi_0}{1 - \xi_0} \frac{1 - \xi}{\xi} \right)^{\frac{2}{3}\delta} + \left(\frac{1 - \xi}{1 - \xi_0} \right)^{\frac{2}{3}\delta}.$$

As in the infinitesimal theory of elasticity we assume linear properties of the material, i.e.

$$(5.8) \quad \mathcal{L}^e = 2\mu\mathbf{I} + \lambda(\mathbf{g} \otimes \mathbf{g}),$$

where μ and λ denote the Lamé constants, and the thermal expansion matrix is postulated as

$$(5.9) \quad \mathcal{L}^{th} = (2\mu + 3\lambda)\theta\mathbf{g},$$

where θ is the thermal expansion constant ($\theta = 12 \cdot 10^{-6} \text{ K}^{-1}$).

5.2. Identification of the material constants

To determine the material constants assumed in Subsec. 5.1 we take advantage of the experimental observations presented by CHAKRABARTI and SPRETNAK [2]. They investigated the localized fracture mode for tensile steel sheet specimens simulating both plane stress and plane strain processes. The material used in their study was AISI 4340 steel. The principal variable in this flat specimen test was the width-to-thickness ratio. Variation in specimen geometry produces significant changes in stress state, directions of shear bands, and ductility. They found that fracture propagated consistently along the shear band localized region.

Let us now consider the adiabatic dynamic process for a thin steel plate under condition of plane stress state. In fact we idealize the initial-boundary value problem investigated by CHAKRABARTI and SPRETNAK [2] by assuming the velocity driven adiabatic process for a thin steel plate. Dimensions of the plate and the variation in time of the kinematic constraints are presented in Fig. 10. The problem has been solved by using the finite difference method. A thin sheet is modelled via $N \times M$ elements, cf. Fig. 10.

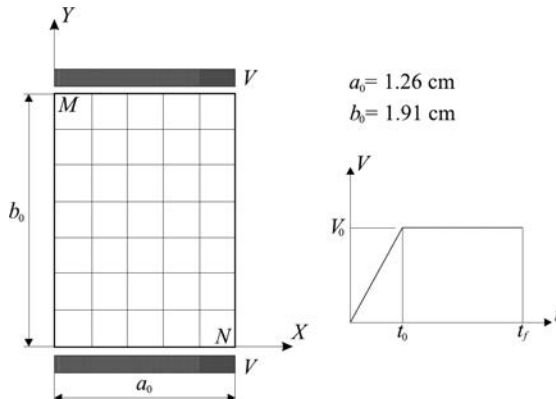


FIG. 10. Dimension of the plate and the variation in time of the kinematic constraints (after CHAKRABARTI and SPRETNAK [2]).

In numerical calculations it is assumed:

$$V_0 = 1.5 \text{ m/s},$$

$$t_0 = 50 \text{ } \mu\text{s},$$

$$t_f = 800 \text{ } \mu\text{s}.$$

The material of a plate is AISI 4340 steel.

Based on the best curve fitting of the experimental results obtained by CHAKRABARTI and SPRETNAK [2] for the stress-strain relation (cf. Fig. 11) the identification of the material constants has been done, cf. Table 1.

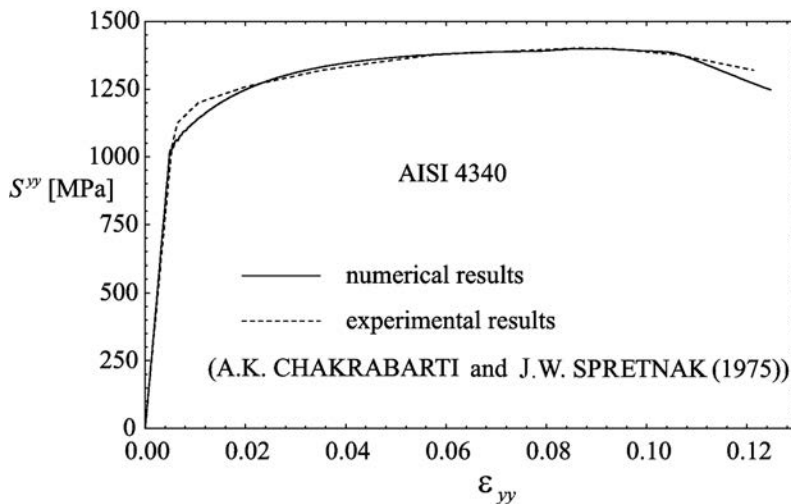


FIG. 11. Component S^{YY} of the second Piola-Kirchhoff stress tensor as a function of the logarithmic strain ϵ_{YY} .

Table 1. An AISI 4340 steel (plate).

$\kappa_s^* = 1155 \text{ MPa}$	$\vartheta_0 = 293 \text{ K}$	$c_1 = 0.1$	$\xi_0 = 6 \cdot 10^{-4}$	$\nu = 0.3$
$\kappa_0^* = 808 \text{ MPa}$	$\iota = 0.1$	$c_2 = 0.067$	$\xi_F = 0.25$	$E = 208 \text{ GPa}$
$\delta^* = 14$	$T_m = 1 \text{ } \mu\text{s}$	$b_1 = 0.58$	$n = 0.25$	$\rho_{\text{Ref}} = 7850 \text{ kg/m}^3$
$\beta^* = 9$	$m = 1$	$b_2 = 1.73$	$\chi = 0.9$	$c_p = 455 \text{ J/kg K}$

5.3. Investigation of stability and convergence

Using the same initial-boundary value problem we can investigate the convergence of the numerical method based on the finite difference discretization. In this analysis we assume that the micro-damage evolution is investigated. For a thin steel plate five different meshes have been assumed. In Fig. 12 distributions of the equivalent plastic deformation along the middle cross-section

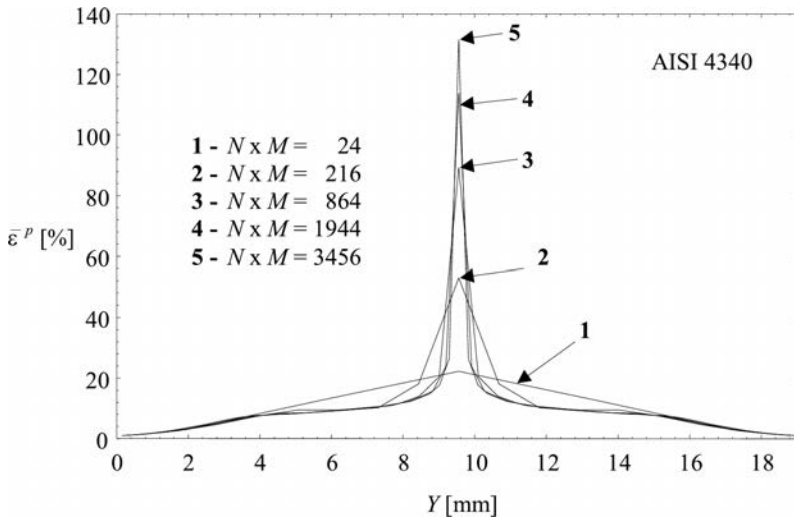


FIG. 12. Distributions of the equivalent plastic deformation along the middle cross-section ($X = a_0/2$) for various meshes.

($X = a_0/2$) for various meshes are presented. Similar results for temperature are showed in Fig. 13. All curves are plotted in the initial configuration of the specimen and for finite time of the process, $t_f = 800 \mu s$. The deformed meshes with various densities of nodes are presented in Fig. 14. Both analysed values shown in Fig. 12 and 13 have strong increase in the middle region of the plate. This suggests that in that region of the specimen the localization of plastic de-

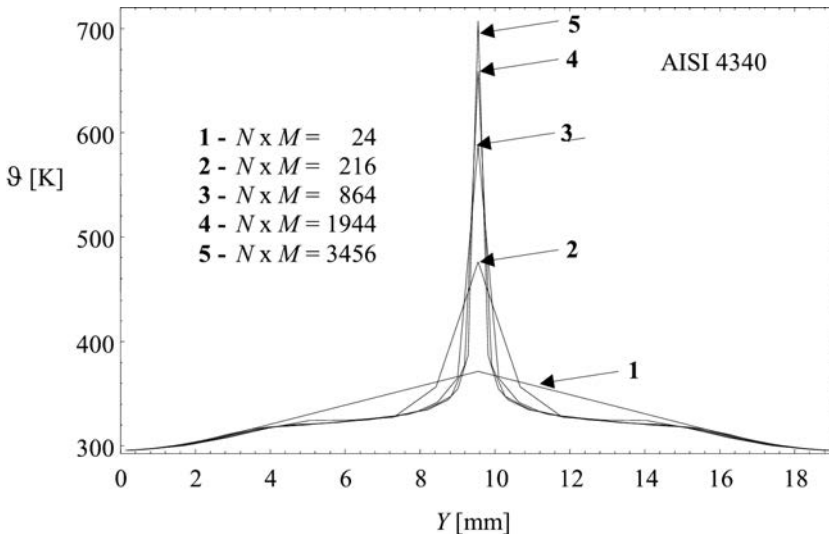


FIG. 13. Distributions of the temperature along the middle cross-section ($X = a_0/2$) for various meshes.

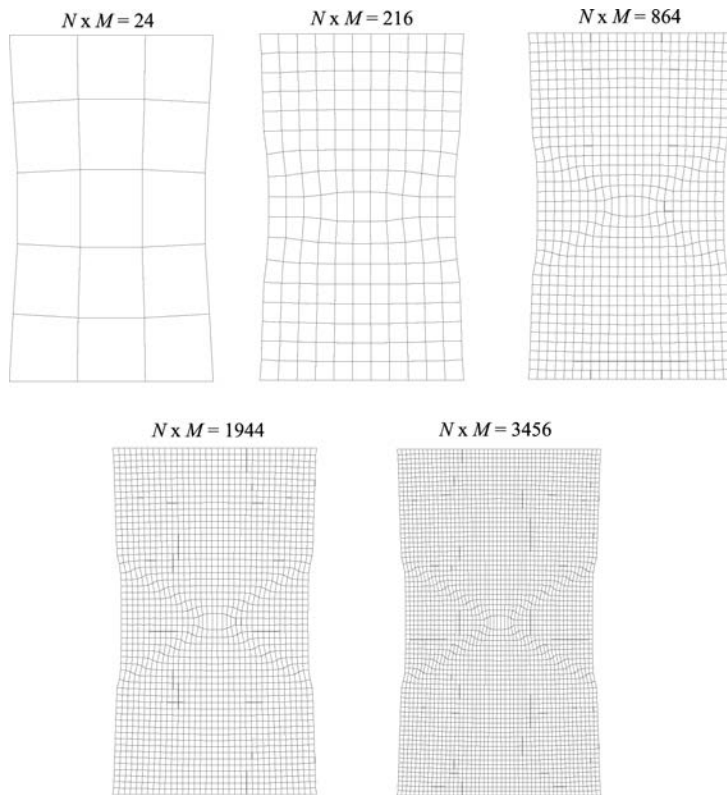


FIG. 14. Deformed meshes with various densities of nodes.

formation takes place. Based on the results for distributions of the equivalent plastic deformation plotted in Fig. 12 we can observe that the finite width of the localized region needs appropriate density for the finite difference mesh (in considered case higher than 864 nodes).

The numerical procedure for the explicit finite difference scheme (4.36) has been accomplished with various time step Δt . The value of the time step has been determined by using the stability criterion (4.38). In Fig. 15 the evolution of the time step Δt in the deformation process for the mesh $N \times M = 3456$ has been shown. For the considered deformation process the time step Δt is decreasing function of time.

The stability of the numerical procedure with constant time step can be keeping in entire interval $[0, t_f]$ provided we assume $\Delta t = 0.025 \mu s$. Then as a result for the considered deformation process we have 32 000 time steps. While the analogical process with various time step Δt is accomplished for 26 603 time steps. This decreases very much time of computation. Very intense change of time step Δt observed from $t = 0.6$ ms in Fig. 15 is caused by the formation of the shear band localization.

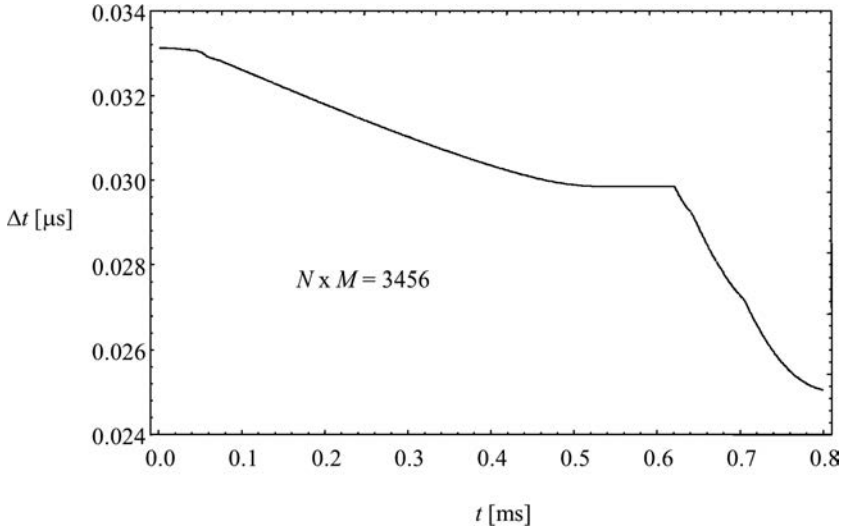


FIG. 15. Evolution of the time step Δt for a mesh with 3456 nodes.

The results obtained show that the satisfaction of the stability criterion (4.38) leads to the convergence of the numerical procedure. We can conclude that the assumed finite difference scheme (4.36) approximates the well posed initial-boundary value problem (4.1). These results can be treated as the numerical proof of the Lax–Richtmyer equivalence theorem formulated in Subsec. 4.8.

5.4. Investigation of localization and fracture phenomena

Let us consider again the adiabatic dynamic process for a thin steel plate under condition of plane stress state which idealized the experimental observations of the localized fracture mode for tensile steel sheet specimens performed by CHAKRABARTI and SPRETNAK [2], cf. Subsec. 5.2.

In Fig. 16 distributions of the equivalent plastic deformation in a thin plate for chosen instants of the deformation process are presented.

The development of macrocracks in a thin plate has been shown in Figs. 17 and 18 and the deformed configuration for final fracture of a plate is presented in Fig. 19.

The results presented permit to draw some conclusions concerning the adiabatic dynamic deformation process for a thin steel plate considered. We observe that two cross shear bands are developed in the center of the specimen. With continued loading process, one of the instability bands becomes more predominant and most of the plastic deformation is confirmed to this particular adiabatic shear band. Fracture occurs along the boundary of this active instability band. The symmetry breaking in the deformation process observed is only due

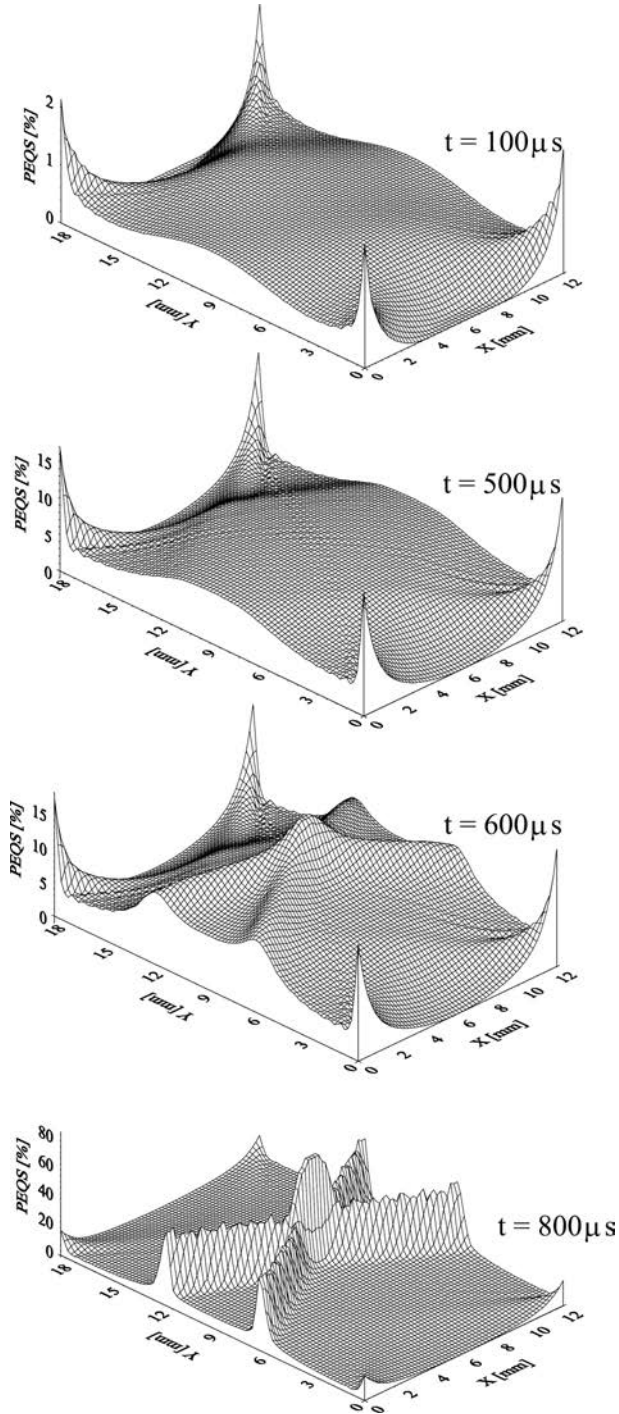


FIG. 16. Distributions of the equivalent plastic strain in a thin plate for chosen instants of the deformation process.

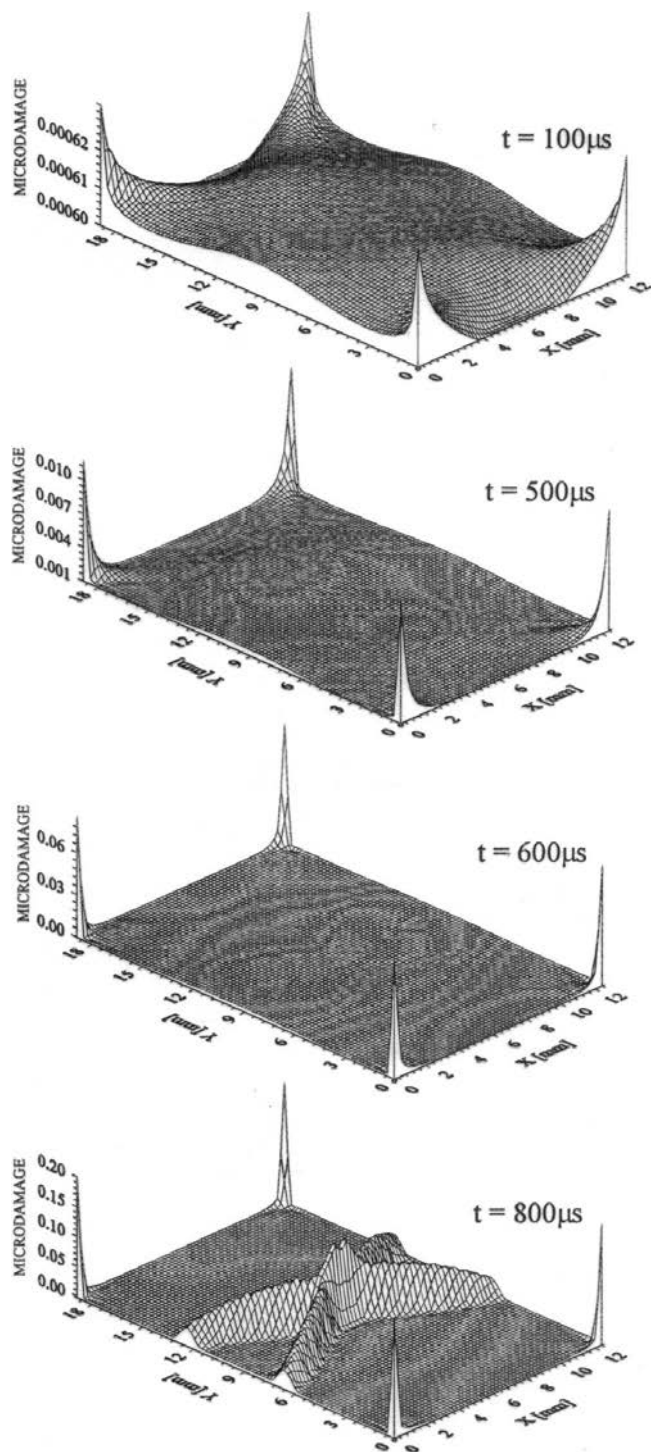


FIG. 17. Distribution of the microdamage for chosen instants of the deformation process.

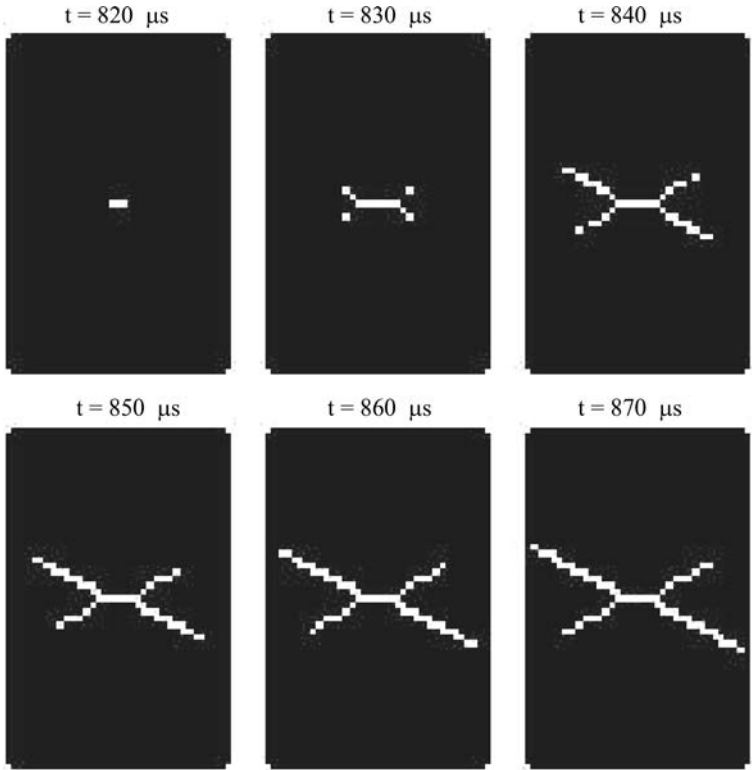


FIG. 18. Development of macrocracks in a thin plate.

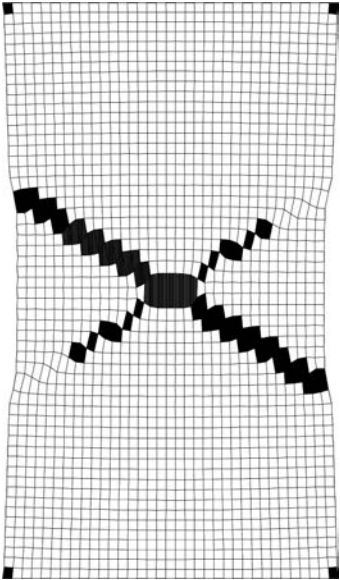


FIG. 19. Deformed configuration for final fracture of the plate.

to very small imperfections generated by numerical procedure. The obtained results are in accord with the experimental observations of CHAKRABARTI and SPRETNAK [2], cf. Fig. 20.

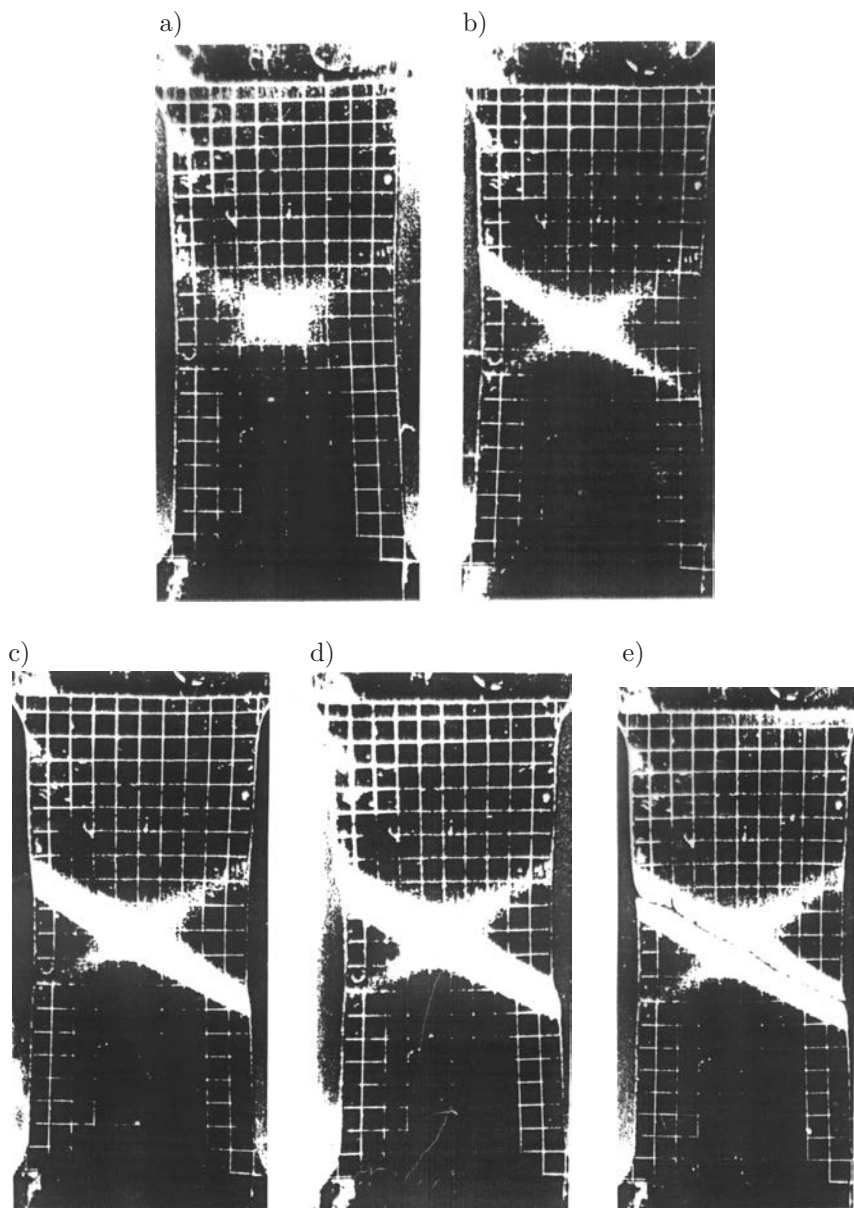


FIG. 20. Initiation and gradual development of instability bands in 0.099 cm thick specimen. One of the instability bands is getting predominant and much of the plastic deformation gets confined in this active band, cf. b)–d); failure takes place by shearing through the instability boundary of active instability band, cf. e) (after CHAKRABARTI and SPRETNAK [2]).

6. NUMERICAL EXAMPLE

6.1. Numerical solution of the initial boundary-value problem

We analyse the impact loaded plate with a pre-notched crack (Fig. 21). The material of the plate is assumed as a AISI 4340 steel and is modeled as elasto-viscoplastic with isotropic hardening-softening effects. We assume that the material softening is caused by intrinsic microdamage mechanism and thermomechanical coupling effect. The height of the specimen is equal to 200 mm, width is 100 mm and length of the initial crack (notch) is equal to 50 mm and is situated unsymmetrically, i.e., 110 mm from the bottom. The plane stress state is considered. As it is shown in Fig. 21, this specimen is loaded asymmetrically to the notch axis. The initial boundary value problem is different than those considered previously by DORNOWSKI and PERZYNA [13] and LI *et al.* [27].

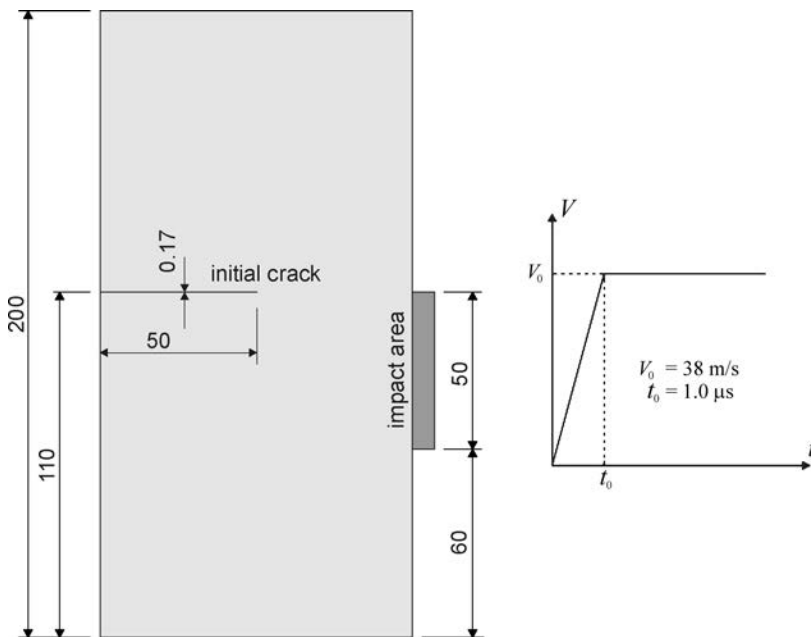


FIG. 21. The impact loaded plate with a prenotched crack.

To obtain the solution of the initial-boundary value problem formulated the finite difference method for regularized elasto-viscoplastic model is used⁶⁾. The

⁶⁾Numerical modelling of localized fracture phenomena in inelastic solids in dynamic loading processes by means of finite element method has been presented by ŁODYGOWSKI and PERZYNA [28].

loading condition is modeled by the velocity of nodes lying on the edge section with length equals to 50 mm, according to the relation

$$(6.1) \quad V(t) = V_0 t/t_0 \quad \text{for } t \leq t_0 \quad \text{and} \quad V(t) = V_0 \quad \text{for } t > t_0.$$

The rise time t_0 is fixed at 1.0 μs and the speed impact $V_0 = 38 \text{ m/s}$. Initial conditions of the problem are homogeneous. In the discussion of the numerical results attention is focused mostly on the phenomenon of crack propagation.

The finite difference method with the explicit time integration scheme (conditionally stable) is used. The stress state in a nodal environment is determined by the iterative procedure of solving the dynamical yield condition with respect to the norm of the plastic deformation rate tensor. The elaborated algorithm satisfies the material objectivity principle with respect to diffeomorphism (any motion). We assume a nonuniform mesh of nodes which contain 180 000 nodes. The smallest mesh has the dimensions $\Delta\chi^1 = \Delta\chi^2 = 40 \mu\text{m}$, the time increment $\Delta t = 0.00356 \mu\text{s}$.

Figure 22 shows the Mises stress contour in the failure region following the impact. It can be clearly observed that the crack follow the path of the greatest Mises stress (the white band). The crack path changes its direction and has irregular (ragged) edges.

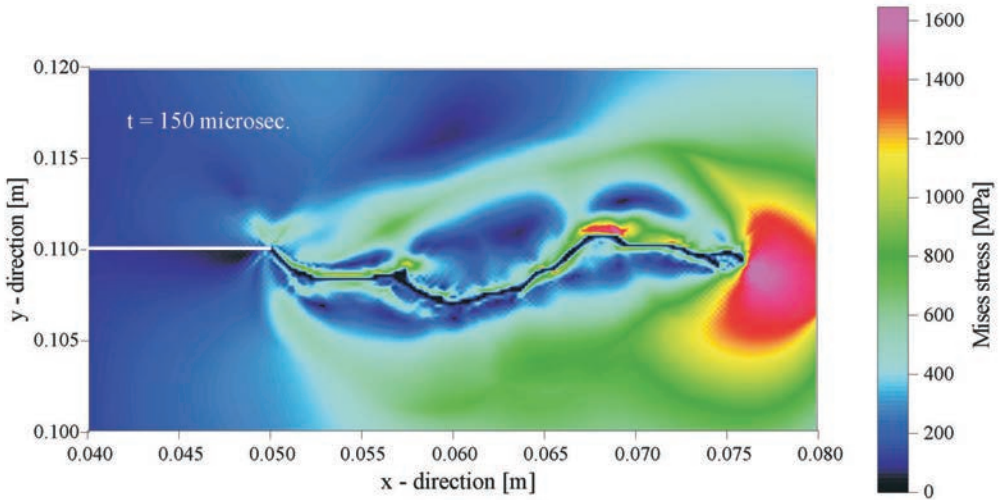


FIG. 22. Misses stress contours in the failure region.

In Fig. 23 the equivalent plastic strain distribution is displayed. It shows that there is a strain concentration region right in the front of the pre-notch tip. Along with the shear band progress the equivalent plastic strain intensity decreases. It confirms that the shear band transforms into an opening crack.

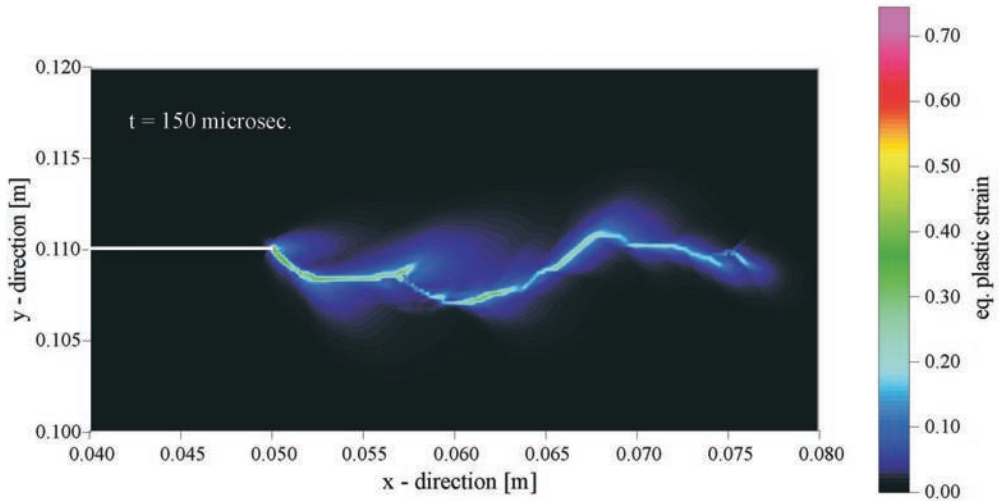


FIG. 23. Evolution of the equivalent plastic deformation in the fracture region.

The evolution of temperature is shown in Fig. 24. Zones of increased temperature correspond to the plastic zones. The maximum value of temperature is $\vartheta_{\max} = 750$ K. The effect of such a strong heating of the material results from its mechanical properties, i.e. the high strength steel, $R_m = 2000$ MPa. From Fig. 24 one may see that the computed temperature distribution is very heterogeneous. The similar effect has been noticed in experimental observations by GUDURU, ROSAKIS and RAVICHANDRAN [21].

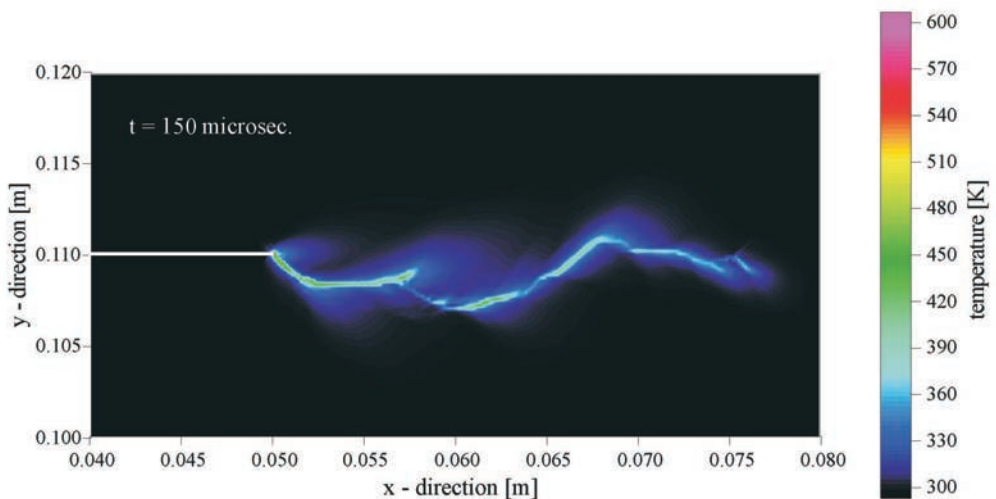


FIG. 24. Evolution of temperature in the fracture region.

In Fig. 25 the evolution of microdamage is presented. It can be clearly observed that the crack path (a black line) is very irregular and it widens steadily.

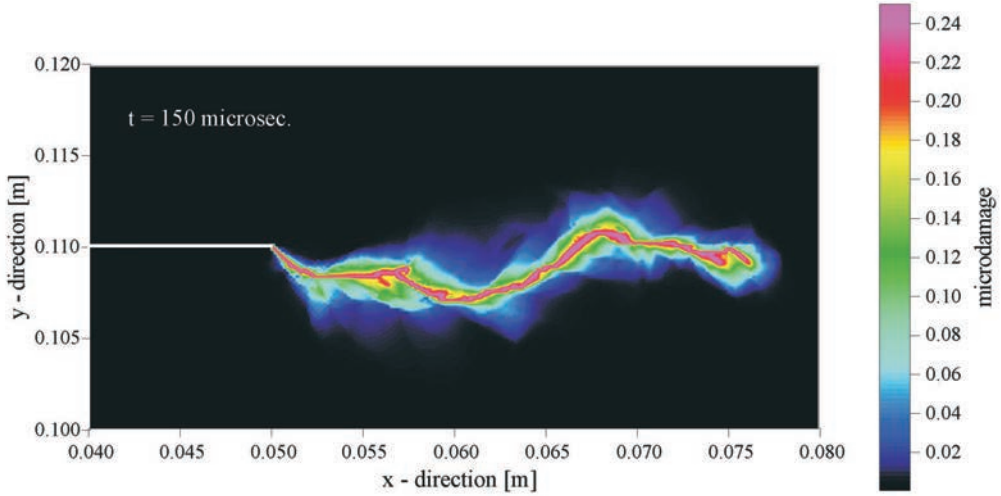


FIG. 25. Evolution of the microdamage and the crack path in the fracture region.

6.2. Discussion of the numerical results

From Fig. 22 we can observed that the macrocrack follows the path of the maximum value of the Mises stress $\tau_M = \left(\frac{2}{3} \boldsymbol{\tau}' : \boldsymbol{\tau}' \right)^{1/2}$. The macrocrack path changes its direction and has irregular edges. It results from the dispersive stress wave interaction and reflection of the considered impact adiabatic process as well as from the fact that the shear band transforms into an opening macrocrack, cf. GLEMA, ŁODYGOWSKI and PERZYNA [17–19]. The dissipation effect due to viscoplastic flow phenomena is observed in Fig. 23 as decay of the equivalent viscoplastic deformation intensity along with the shear band progress.

From Fig. 24 one may see that the computed temperature distribution along a propagating shear band is very heterogeneous and nonuniform. A similar effect has been noticed in experimental observations by GUDURU, ROSAKIS and RAVICHANDRAN [21]. They consistently observed, in all experiments where a propagating shear band was imaged, that the temperature distribution along the shear band is highly non-uniform, with discrete regions of high temperature, that look like “hot spots”. These hot spots are also seen to translate along the length of the shear band. Figure 26 shows one such image where the hot spots can be identified easily. This observation raises question about the spatial and temporal nature of shear deformation inside a shear band. We suggest that the

reason of this phenomenon is caused by interaction and reflection of dispersive stress waves during observed impact adiabatic process.

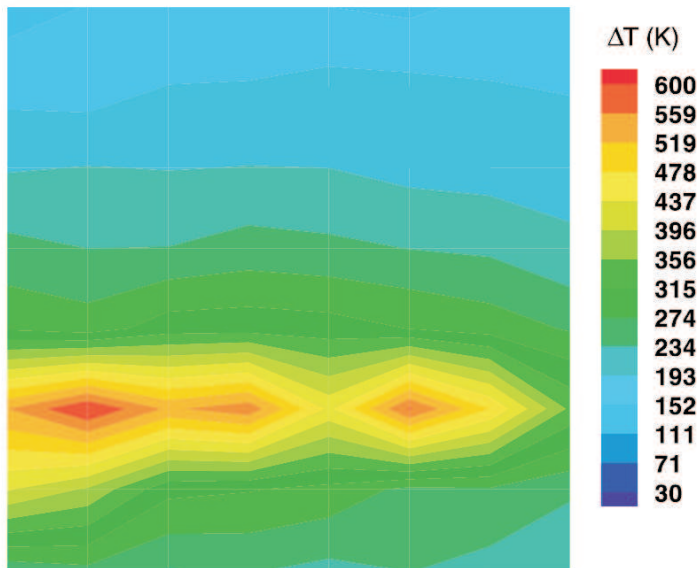


FIG. 26. A thermal image of a shear band showing non-uniform temperature distribution along the length of the band. After GUDURU, ROSAKIS and RAVICHANDRAN [21].

In our recent paper GLEMA, ŁODYGOWSKI and PERZYNA [20] investigated this problem numerically by using the finite element method and ABAQUS system. We used regularized thermo-elasto-viscoplastic constitutive model with one scalar internal state variable, namely equivalent inelastic deformation. We considered the initial boundary value problem, cf. Fig. 27, which is idealization of the process observed experimentally by GUDURU, ROSAKIS and RAVICHANDRAN [21], by assuming the velocity boundary condition and different material of the specimen (HY-100 steel). To identify the material functions and constants we used the experimental observation results obtained by CHO, CHI and DUFFY [4], cf. also CHI *et al.* [3]. The contour plots of equivalent inelastic deformation and temperature obtained for time instants 40, 50, 60 μs are visualized in Fig. 28 for unsymmetric impact. To show better that we obtained non-uniform temperature distribution along the shear band we present the magnification of the result for the field of temperature at 60 μs in Fig. 29. The function of shear band length and propagation velocity of its front were also calculated, cf. Fig. 30. The advances of shear band length in experimental observations and in numerical computations have similar find values and the functions presenting its evolution are comparable. The comparison of the shear band propagation velocity reaches the same conclusion.

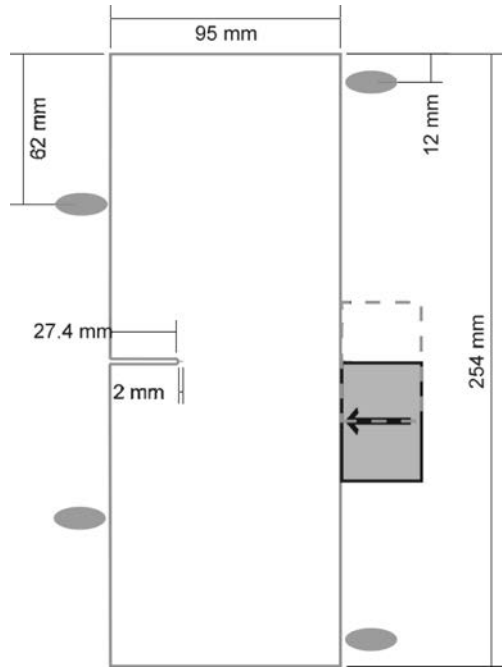


FIG. 27. Specimen geometry.

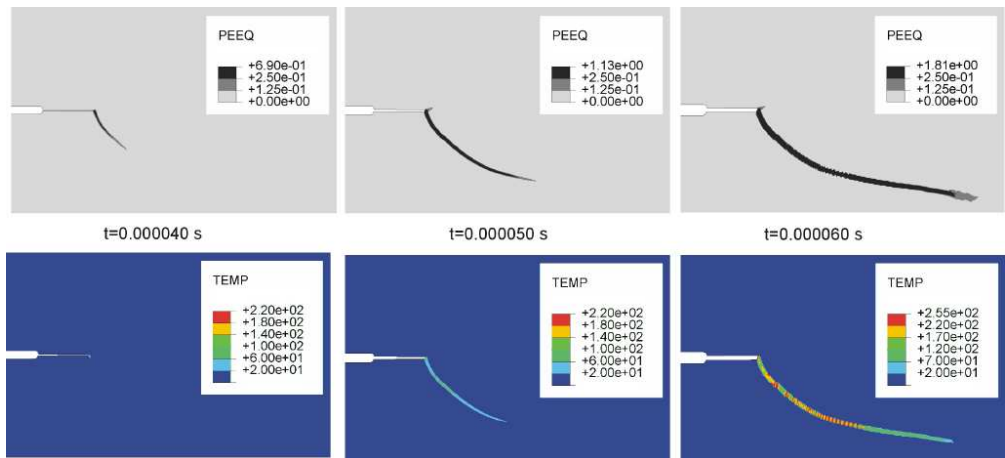


FIG. 28. Evolution of plastic equivalent deformation and temperature along the shear band for unsymmetric impact (for 40, 50, 60 μ s).

Rather the qualitative agreement is verified, than strict comparison of values. The common sudden velocity drop, observed in experiment and simulations, is specially worth to point it out.

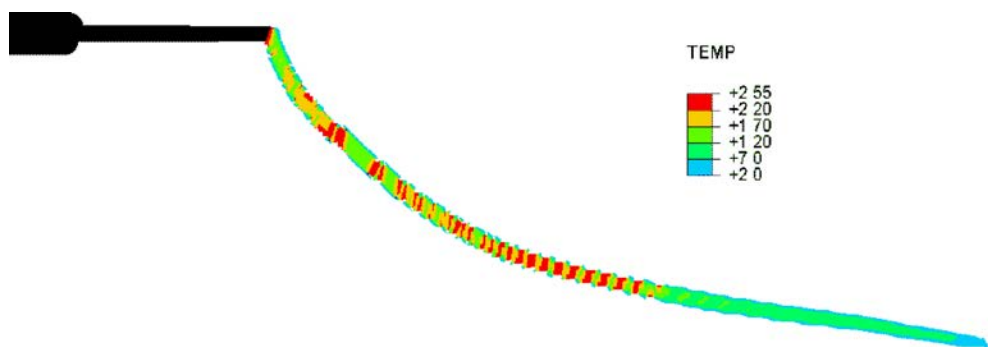


FIG. 29. Magnification of the results for the field of temperature at 60 μ s for unsymmetric impact.

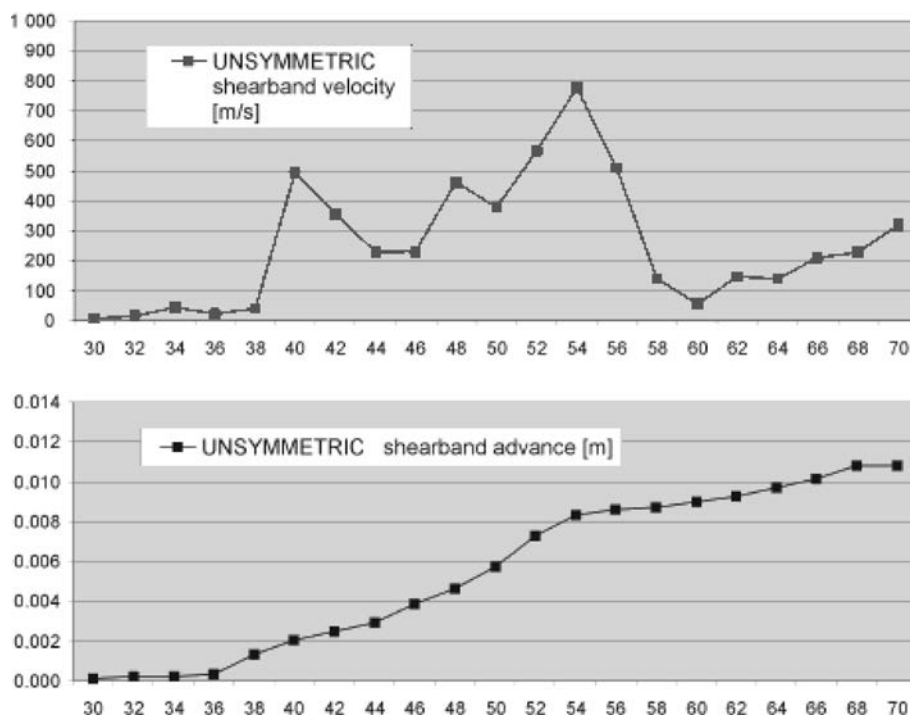


FIG. 30. Propagation velocity of shear band front and shear band length as functions of time, for unsymmetric impacts.

The remark concerning the temperature distribution goes in the same direction. There is valuable to expose that numerical results show the particular character of experimental ones, with occurrence of discrete regions of high temperature, that are described as “hot spots”, cf. Fig. 29. Appearance of several local extremes take place after the mentioned above drop of propagation ve-

locity of the shear band tip. The evolution of described variables suggests the step-wise nature of shear band propagation phenomena caused by the reflection and interaction of dispersive stress waves during impact adiabatic process.

From the results presented in Figs. 22–25 one can easily observe that the localized fracture is preceded by the propagation of the shear band⁷⁾. This is also visible in Fig. 25, where the propagated localized region of critical microdamage (it means the fracture front for $\xi = \xi^F$) is preceded by the shear band along which the microdamage is smaller than $\xi = \xi^F$. The evolution of the microdamage and the macrocrack path in the fracture region shown in Fig. 25 indicates that the macrocrack path is very irregular and it widens steadily. It seems that in some places of the macrocrack we can expect the branching effect as it has been observed by GUDURU, ROSAKIS and RAVICHANDRAN [21], cf. Fig. 8.

Of course, we have to take into account that during experimental observations they investigated real material (C300 steel), which can have some impurities, which help to generate the shear band bifurcation, while we assumed fully homogeneous material of the plate for our numerical simulation.

We can conclude that the shear band branching can be generated by reflection and interaction of dispersive stress waves during adiabatic impact process and by some real existing impurities of the investigated material.

7. EPILOGUE

The elaborated numerical algorithm satisfies the material objectivity principle with respect to diffeomorphism (any motion). The discretization parameters are assumed in such a way that the problem of mesomechanics is solved properly. A thin shear band region of finite width which undergoes significant deformation and temperature rise has been determined. Its evolution until occurrence of final fracture has been simulated. Shear band advance, as a function of time and the evolution of the Mises stress, equivalent plastic deformation, temperature and the macrocrack path in the fracture region have been determined. Qualitative comparison of numerical results with experimental observation data has been presented. Based on this comparison we can conclude that our numerical results are in accord with the experimental observations performed by GUDURU, ROSAKIS and RAVICHANDRAN [21]. Particularly, in our numerical simulation the temperature evolution along the shear band region is very nonuniform and the obtained macrocrack path is very irregular and is showing a tendency to branching phenomenon similarly as have been suggested by experimental observations. The numerical results obtained have been proven the usefulness of

⁷⁾For a thorough discussion of numerical investigation of propagation of shear bands in inelastic solids please consult GLEMA, ŁODYGOWSKI and PERZYNA [20].

the thermo-elasto-viscoplastic theory in the numerical investigation of dynamic shear band propagation and localized fracture phenomena.

ACKNOWLEDGMENT

The paper was prepared within the framework of the Research Projects N N501 036435 and N N519 419435 of the Ministry of Higher Education and Science of Poland.

REFERENCES

1. R. ABRAHAM, J. E. MARSDEN, T. RATIU, *Manifolds, Tensor Analysis and Applications*, Springer, Berlin, 1988.
2. A. K. CHAKRABARTI, J. W. SPRETNAC, *Instability of plastic flow in the direction of pure shear*, Metallurgical Transactions, **6A**, 733–747, 1975.
3. Y. C. CHI, S. H. LEE, K. CHO, J. DUFFY, *The effects of tempering and test temperatures on the dynamic fracture initiation behaviour of an AISI 4340 VAR steel*, Brown University Technical Report, August 1988.
4. K. CHO, Y. C. CHI, J. DUFFY, *Microscopic observations of adiabatic shear bands in three different steels*, Brown University Report No DAAL03-88-K-0015/3, September 1988.
5. B. D. COLEMAN, W. NOLL, *The thermodynamics of elastic materials with heat conduction and viscosity*, Arch. Rational Mech. Anal., **13**, 167–178, 1963.
6. R. COURANT, K. O. FRIEDRICHS, H. LEWY, *Über die Partiellen Differenzgleichungen der Mathematischen Physik*, Math. Ann., **100**, 32–74, 1928.
7. D. R. CURRAN, L. SEAMAN, D. A. SHOCKEY, *Dynamic failure of solids*, Physics Reports, **147**, 253–388, 1987.
8. R. DAUTRAY, J. L. LIONS, *Mathematical Analysis and Numerical Methods for Science and Technology*, Vol. 6. Evolution Problems II, Springer, Berlin 1993.
9. W. DORNOWSKI, *Influence of finite deformation on the growth mechanism of microvoids contained in structural metals*, Arch. Mech., **51**, 71–86, 1999.
10. W. DORNOWSKI, P. PERZYNA, *Constitutive modelling of inelastic solids for plastic flow processes under cyclic dynamic loadings*, In: Transaction of the ASME, J. Eng. Materials and Technology, **121**, 210–220, 1999.
11. W. DORNOWSKI, P. PERZYNA, *Localization phenomena in thermo-viscoplastic flow processes under cyclic dynamic loadings*, CAMES, **7**, 117–160, 2000.
12. W. DORNOWSKI, P. PERZYNA, *Localized fracture phenomena in thermo-viscoplastic flow processes under cyclic dynamic loadings*, Acta Mechanica, **155**, 233–255, 2002.
13. W. DORNOWSKI, P. PERZYNA, *Numerical investigation of localized fracture phenomena in inelastic solids*, Foundations of Civil and Environmental Engineering, **7**, 79–116, 2006.
14. M. K. DUSZEK, P. PERZYNA, *The localization of plastic deformation in thermoplastic solids*, Int. J. Solids Structures, **27**, 1419–1443, 1991.

15. M. K. DUSZEK-PERZYNA, P. PERZYNA, *Analysis of the influence of different effects on criteria for adiabatic shear band localization in inelastic solids* [in:] Proceedings Material Instabilities: Theory and Applications, ASME Congress, Chicago, 9–11 November 1994, R. C. BATRA and H. M. ZBIB [Eds.], AMD-Vol. 183/MD-Vol.50, ASME, New York, pp. 59–85, 1994.
16. D. R. DURRAN, *Numerical Methods for Wave Equations in Geophysical Fluid Dynamics*, Springer, New York, 1999.
17. A. GLEMA, T. ŁODYGOWSKI, P. PERZYNA, *Interaction of deformation waves and localization phenomenon in inelastic solids*, Comput. Methods Appl. Mech. Engng., **183**, 123–140, 2000.
18. A. GLEMA, T. ŁODYGOWSKI, P. PERZYNA, *The role of dispersion for the description of strain localization in materials under impact loading*, [in:] European Conference on Computational Mechanics, June 26–29, 2001, Cracow, Poland.
19. A. GLEMA, T. ŁODYGOWSKI, P. PERZYNA, *Localization of plastic deformations as a result of wave interaction*, CAMES, **10**, 81–91, 2003.
20. A. GLEMA, T. ŁODYGOWSKI, P. PERZYNA, *Numerical investigation of dynamic shear bands in inelastic solids as a problem of mesomechanics*, Comput. Mech., **41**, 219–229, 2008.
21. P. R. GUDURU, A. J. ROSAKIS, G. RAVICHANDRAN, *Dynamic shear bands: an investigation using high speed optical and infrared diagnostic*, Mechanics of Materials, **33**, 371–402, 2001.
22. P. R. GUDURU, A. T. ZEHNDER, A. J. ROSAKIS, G. RAVICHANDRAN, *Dynamic full field measurements of crack tip temperatures*, Engineering Fracture Mechanics, **68**, 1535–1556, 2001.
23. B. GUSTAFSSON, H. O. KREISS, J. OLIGER, *Time Dependent Problems and Difference Methods*, John Wiley, New York, 1995.
24. J. W. HUTCHINSON, *Plasticity at the micron scale*, Int. J. Solids and Structures, **37**, 225–238, 2000.
25. I. R. IONESCU, M. SOFONEA, *Functional and Numerical Methods in Viscoplasticity*, Oxford 1993.
26. J. N. JOHNSON, *Dynamic fracture and spallation in ductile solids*, J. Appl. Phys., **52**, 2812–2825, 1981.
27. S. LI, W.-K. LIU, D. QIAN, P. R. GUDURU, A. J. ROSAKIS, *Dynamic shear band propagation and micro-structure of adiabatic shear band*, Comput. Methods Appl. Mech. Engng., **191**, 73–92, 2001.
28. T. ŁODYGOWSKI, P. PERZYNA, *Numerical modelling of localized fracture of inelastic solids in dynamic loading processes*, Int. J. Num. Meth. Engng., **40**, 4137–4158, 1997.
29. J. E. MARSDEN, T. J. R. HUGHES, *Mathematical Foundations of Elasticity*, Prentice-Hall, Englewood Cliffs, New York, 1983.
30. H. C. MEYERS, *Dynamic Behaviour of Materials*, John Wiley, New York 1994.
31. A. NEEDLEMAN, *Computational mechanics at the mesoscale*, Acta Materialia, **48**, 105–124, 2000.

32. J. A. NEMES, J. EFTIS, *Constitutive modelling of the dynamic fracture of smooth tensile bars*, Int. J. Plasticity, **9**, 243–270, 1993.
33. J. OLDROYD, *On the formulation of rheological equations of state*, Proc. Roy. Soc. (London), **A 200**, 523–541, 1950.
34. P. PERZYNA, *The constitutive equations for rate sensitive plastic materials*, Quart. Appl. Math., **20**, 321–332, 1963.
35. P. PERZYNA, *Fundamental problems in viscoplasticity*, Advances in Applied Mechanics, **9**, 243–377, 1966.
36. P. PERZYNA, *Thermodynamic theory of viscoplasticity*, Advances in Applied Mechanics, **11**, 313–354, 1971.
37. P. PERZYNA, *Constitutive modelling of dissipative solids for postcritical behaviour and fracture*, ASME J. Eng. Materials and Technology, **106**, 410–419, 1984.
38. P. PERZYNA, *Internal state variable description of dynamic fracture of ductile solids*, Int. J. Solids Structures, **22**, 797–818, 1986a.
39. P. PERZYNA, *Constitutive modelling for brittle dynamic fracture in dissipative solids*, Arch. Mechanics, **38**, 725–738, 1986b.
40. P. PERZYNA, *Instability phenomena and adiabatic shear band localization in thermoplastic flow processes*, Acta Mechanica, **106**, 173–205, 1994.
41. P. PERZYNA, *Interactions of elastic-viscoplastic waves and localization phenomena in solids*, [in:] Proceedings IUTAM Symposium on Nonlinear Waves in Solids, August 15–20, 1993, Victoria, Canada, J. L. WEGNER and F. R. NORWOOD [Eds.], ASME 1995, pp. 114–121, 1995.
42. P. PERZYNA, *Thermo-elasto-viscoplasticity and damage*, [in:] Handbook of Materials Behaviour Models, J. LEMAITRE [Ed.], Academic Press, New York, pp. 821–834, 2001.
43. P. PERZYNA, *The thermodynamical theory of elasto-viscoplasticity*, Engineering Transactions, **53**, 235–316, 2005.
44. P. PERZYNA, *Application of the thermodynamical theory of elasto-viscoplasticity in modern manufacturing processes*, [in:] Damage Mechanics and Micromechanics of Localized Fracture Phenomena in Inelastic Solids, CISM Courses and Lectures, G. Z. VOYIADJIS [Ed.], Vol. **525**, Springer, Wien New York, pp. 225–376, 2011.
45. P. PERZYNA, A. DRABIK, *Description of micro-damage process by porosity parameter for nonlinear viscoplasticity*, Arch. Mech., **41**, 895–908, 1989.
46. R. D. RICHTMYER, *Principles of Advance Mathematical Physics*, Vol. I, Springer, New York 1978.
47. R. D. RICHTMYER, K. W. MORTON, *Difference Methods for Initial-Value Problems*, John Wiley, New York 1967.
48. S. SHIMA, M. OYANE, *Plasticity for porous solids*, Int. J. Mech. Sci., **18**, 285–291, 1976.
49. D. A. SHOCKEY, L. SEAMAN, D. R. CURRAN, *The microstatistical fracture mechanics approach to dynamic fracture problem*, Int. J. Fracture, **27**, 145–157, 1985.
50. D. SIDEY, L. F. COFFIN, *Low-cycle fatigue damage mechemism at high temperature*, [in:] Fatigue Mechanism, Proc. ASTM STP 675 Symposium, Kansas City, Mo., May 1978, J. T. FONG [Ed.], Baltimore, pp. 528–568, 1979.

51. L. J. SLUYS, *Wave propagation, localization and dispersion in softening solids*, Doctoral thesis, Delft University Press, Delft, 1992.
52. G. STRANG, G. J. FIX, *An Analysis of the Finite Element Method*, Prentice-Hall, Englewood Cliffs 1973.
53. S. A. THAU, *Linear dispersive waves*, [in:] Nonlinear Waves, S. LEIBOVICH and A. R. SEEBASS [Eds.], Cornell University Press, Ithaca, 1974, pp. 44-81.
54. C. TRUESDELL, W. NOLL, *The nonlinear field theories*, Handbuch der Physik, Band III/3, pp. 1-579, Springer, Berlin, 1965.
55. G. B. WHITHAM, *Linear and Nonlinear Waves*, John Wiley, New York, 1974a.
56. G. B. WHITHAM, *Dispersive waves and variational principles*, [in:] Nonlinear Waves, S. LEIBOVICH and A. R. SEEBASS [Eds.], Cornell University Press, Ithaca, 1974b, pp. 139-169.
57. M. ZHOU, A. J. ROSAKIS, G. RAVICHANDRAN, *Dynamic propagating shear band in impact-loaded prenotched plates. I. Experimental investigations of temperature signatures and propagation speed*, J. Mech. Phys. Solids, **44**, 981-1006, 1996.
58. M. ZHOU, G. RAVICHANDRAN, A. J. ROSAKIS, *Dynamic propagating shear band in impact-loaded prenotched plates. II. Numerical simulations*, J. Mech. Phys. Solids, **44**, 1007-1032, 1996.

Received July 18, 2011.

SUBSCRIPTIONS

Address of the Editorial Office: Engineering Transactions

Institute of Fundamental Technological Research

Pawińskiego 5B, PL 02-106 Warsaw, Poland

Tel.: (48-22) 826 12 81 ext. 206, Fax: (48-22) 826 98 15, E-mail: engtrans@ippt.gov.pl

Subscription orders for all journals edited by IPPT (Institute of Fundamental Technological Research) may be sent directly to the Publisher:

Institute of Fundamental Technological Research

e-mail: subscribe@ippt.gov.pl

Please transfer the subscription fee to our bank account:

Payee: IPPT PAN,

Bank: Pekao S.A. IV O/Warszawa,

Account number 05124010531111000004426875.

All journals edited by IPPT are available also through:

- Foreign Trade Enterprise ARS POLONA ul. Obrońców 25,
03-933 Warszawa, Poland, Tel. (48-22) 509 86 38, 509 86 37
e-mail: arspolona@arspolona.com.pl
- RUCH S.A. ul. Jana Kazimierza 31/33,
01-248 Warszawa, Poland,
Tel. (48-22) 532 88 16, Fax (48-22) 532 87 31
e-mail: prenumerata@okdp.ruch.com.pl
- International Publishing Service Sp. z o.o. ul. Piękna 31/37
00-677 Warszawa, Poland, Tel. (48-22) 628 60 89, Fax: (48-22) 621 72 55
e-mail: piekna.bookstore@abe.pl

Warunki prenumeraty

Prenumeratę na wszystkie czasopisma wydawane przez IPPT PAN przyjmuje Dział Wydawnictw IPPT. Bieżące numery można nabywać, a także zaprenumerować roczne wydanie Engineering Transactions, bezpośrednio w IPPT PAN, ul. Pawińskiego 5B, 02-106 Warszawa

Tel.: (48-22) 826 60 22; Fax: (48-22) 826 98 15

e-mail: subscribe@ippt.gov.pl

Wpłaty na prenumeratę przyjmują także regionalne Działy Sprzedaży Prasy RUCH S.A.

Infolinia: 804 200 600. Zamówienia można przysyłać pocztą elektroniczną ze strony

www.prenumerata.ruch.com.pl